Microstructural Characterization of Al-Fe Intermetallics in Aluminum Alloy 7xxx during Controlled Solidification

BY: KISHOR KUMAR NAGARAJ, B.Eng.

A Thesis Submitted to the School of Graduate Studies in Partial Fulfillment of the Requirements for the Degree

Master of Applied Science in Mechanical Engineering

Title: Microstructural Characterization of Al-Fe Intermetallics in Aluminum Alloy 7xxx during Controlled Solidification

Author: Kishor Kumar Nagaraj

M.A.Sc. Thesis Number of Pages: 150

Supervisors: Dr.Joseph McDermid, Dr.Joey Kish

Location: Department of Mechanical Engineering, McMaster University, Hamilton, Ontario, Canada - L8S 4L7

Abstract

Aluminum 7xxx series alloys have been a major focus for lightweight automotive structural components to achieve the targeted weight reductions by auto industries and, in turn, to increase the vehicle fuel efficiency. AA 7xxx series wrought alloy components have been widely used by the aerospace and automotive industries for many decades due to their low density and high strength. However, although near net shape casting of these alloys has many benefits versus wrought alloys; this processing route has been a challenge for the researchers and the auto industry because of limitations due to castability issues such as like hot tearing and die soldering. One possible mitigation strategy involves the addition of iron (Fe) as one of the major alloying element and then subsequently optimizing the alloy chemistry and solidification parameters in terms of die soldering.

The objective of this thesis is to determine the microstructural evolution of any Al-Fe intermetallic phases with respect to cooling rate during solidification for a range of AA 7xxx series alloy compositions. Fe was added at three different levels in a total of nine alloy composition developed from a Taguchi experimental matrix based on the interaction of three composition levels for four alloying elements. The alloys were cast using a custom built casting rig while the cooling rates were measured along the length of a directionally solidifying sample.

The thermocouple measurements were analyzed to determine the velocity of the solid/liquid interface, overall cooling rate and thermal arrest points for later correlation to variations in the microstructural development of any Al-Fe intermetallic phase particles present in the experimental alloys. Metallographic samples were taken at locations with

known cooling rates to determine the resultant microstructure. Scanning electron microscopy (SEM) and energy dispersive X-Ray spectroscopy (EDS) were performed to obtain elemental analyses of the Al-Fe intermetallic phases for present in the samples. The Fe maps obtained by EDS were processed and analyzed using Image-J software to determine the size distribution and area fraction of the Al-Fe intermetallic phases as a function of alloy composition and solidification rates. Also, a regression analysis was used to develop a statistical model to predict the variation of intermetallic particle size and area fraction of the Al-Fe intermetallic phases as a function of alloy composition and cooling rate.

Based on the experimental investigation and analysis of the nine Al 7xxx-Fe alloys the results can be summarized as follows: (1) Cooling rate has a strong influence on the chemistry and morphology of the Fe intermetallic particles: It was determined that the dominant intermetallic species changes from the equilibrium Al_3Fe to the metastable Al_6Fe alloys for cooling rates in excess of approximately10 °C/s. (2) Alloy cooling rate does significantly affect the area fraction of the Fe intermetallic particles. It was determined that the morphology of the Al-Fe particles transitions from a relatively low aspect ratio particles to a high aspect, needle-like particles for cooling rates less than approximately 10 °C/s. (3) Alloying elements such as Zn, Cu, and Mg does not influence the Fe intermetallic chemistry and the area fraction of the intermetallics.

Acknowledgements

Firstly I would like to thank my supervisor Dr. Joe McDermid, for his invaluable inputs and guidance. I am grateful for his patience and encouragement that carried me on through difficult times. This thesis would not have been possible without his direction and support.

I would also like to thank my co-supervisor Dr. Joey Kish, for all the insights and suggestions, especially his careful reading of this document and a number of fruitful discussions that undoubtedly improved the final result.

I would also like to express sincere gratitude to my previous supervisor Dr.Sumanth Shankar, for accepting me as his student. I am grateful to have had the privilege of attending the prestigious McMaster University.

This thesis also benefited greatly from the generous help and advice offered by LMCRC lab members, Thanks to Dr.Jeyakumar Manikraj, Dr.Xiachun Zeng, Dr. Kifah Takrouri for all the support and guidance. Special thanks to Dr. Beth McNally and Chris Butcher for providing SEM training.

I am grateful to have been part of the Automotive Partnership Canada (APC).I thank APC for funding my graduate research. Special thanks to staff of Department of Mechanical Engineering for taking care of all the administrative hurdles I have come across.

My deepest gratitude goes to my parents and sister for their unflagging love and support throughout my life.

Last but not least, I want to thank my wife Rekha and my beloved daughter Nirvi for your unconditional love and care.

Table of Contents

List of Figures

List of Tables

List of Abbreviations

AFS	**A**merican **F**oundry **S**ociety
EDS	**E**nergy **D**ispersive **S**pectroscopy
HPDC	**H**igh **P**ressure **D**ie **C**asting
SEM	**S**canning **E**lectron **M**icroscopy
UTS	**U**ltimate **T**ensile **S**trength
YS	**Y**ield **S**trength
TC	**T**hermocouple
CR	**C**ooling **R**ate

Introduction

Automobile manufacturers are striving to develop better solutions to help reduce global warming resulting from vehicular emissions and to comply with government mandated emission standards. The U.S. auto industry has targeted a doubling of current [2015] fuel efficiency of new passenger vehicle by 2035. It also intends to achieve a 20% reduction in vehicular weight over that period [1].

Major U.S research agencies suggested combination of three options to reduce fuel consumption and vehicle weight reduction: material substitution, vehicular redesign and vehicle downsizing (1). The use of aluminum (Al) in automotive applications is rapidly expanding as, it offers significant potential for weight reduction over steel, thereby increasing fuel efficiency while meeting the stringent safety regulations imposed by government agencies. It is estimated that by substituting Al in place of steel a, 20% reduction in weight is estimated to be achieved by 2035, as shown in Figure 1.1.

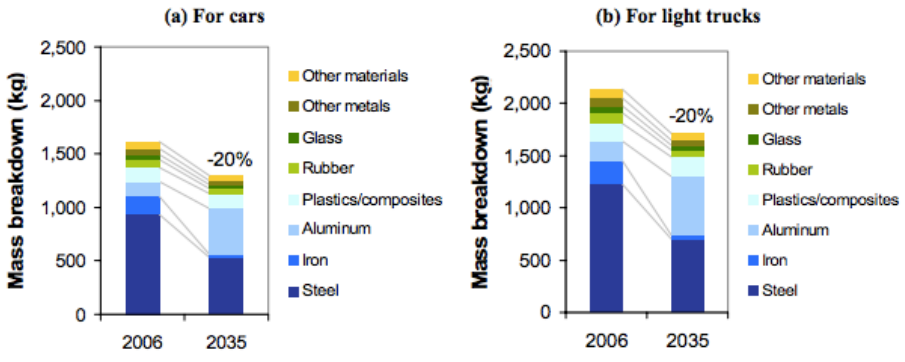

Figure 1.1 Material composition of average new gasoline vehicle after material substitution [1]

Based on this assessment, with the combination of material substitution, vehicular redesign and downsizing, a maximum weight reduction of 35% can be achieved by 2035. With some inherent limitations to decreasing vehicle weight further, estimates show that the minimum average mass of a new car would be reduced to 1050 kg from 1620 kg for existing standard passenger vehicles and to1390 kg from 2140 kg by 2035 for light duty trucks.

Being a cost sensitive industry, auto manufacturers are very cautious about selecting alternative materials like Al alloys. Although aluminum components have great potential to penetrate in the market, their limitations including processing techniques and required material properties are a large challenges to be addressed.

Cast Al alloy products are less expensive alternatives for advanced high strength steel (AHSS) structural components, but the mechanical properties offered by conventional Al alloys do not meet the design requirements. A typical casting alloy has a yield strength of 250 MPa and an elongation (ductility) of 8% after heat treatment, but the mechanical properties required for cast structural components fall close to 350 MPa yield strength and more than 10% elongation. Achieving these required properties in cast aluminum alloys is only possible with advances in near net shape casting technology and the selection of an optimum alloy composition that produces the mechanical properties required for the intended application.

AA 7xxx series Al alloys offer high strength and are widely used as commercial wrought alloys, but they are not suitable for structural applications that require high strength with ductility for crashworthiness within the automotive industry. The higher processing cost of wrought Al alloy components compare to AHSS makes them a non- economical

choice for substitution. Also, the reduced formability of these alloys makes it difficult to achieve optimum shape and wall thickness and, hence, restricts the achievable weight reduction.

Casting processes can achieve high integrity components compared to wrought processes, specifically for casting high performance, high integrity, complex thin-wall shapes and geometries. Conventional Al alloy casting with higher silicon contents provides higher fluidity and good castability because of their relatively high volumes of the Al-Si eutectic phase. However, these alloys do not achieve the high mechanical properties exhibited by the conventional wrought alloys such as AA 2014, AA 6082 and AA 7075. Shape casting of these wrought alloy compositions has been a challenge for materials engineers because of castability issues such as hot tearing and die soldering [2].

The wrought AA 7xxx alloys have a wide solidification temperature range and large solidification shrinkage which can lead to hot tearing during solidification. Also, high temperature chemical and metallurgical reactions between the molten Al alloy and the steel die material can leads to die soldering when the Fe in the die material dissolves in-to the molten Al alloy and vice versa.

For example Shankar and Apelian [3] studied the mechanisms by which Al alloys stick to steel die materials during die soldering .The process was found to be a diffusion controlled phenomenon in which the Fe and the Al atoms inter-diffuse, forming a thick intermetallic layer at the die/casting interface, as shown in Figure 1.2. They also found that die soldering was due to rapid reaction kinetics between the solid and liquid.

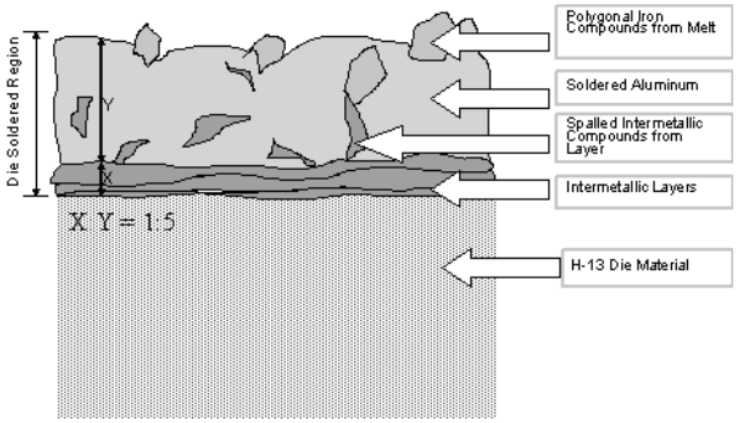

Figure 1.2 Schematic cross-section of a die showing the intermediate layers and soldered aluminum [3]

It is evident from the literature that the addition of Fe as an alloy modifier can mitigate die soldering tendencies by limiting the Al alloy-steel die reaction kinetics and also reduce the hot tearing tendency by increasing the high temperature strength of the casting. However, castability issues when shape casting of AA 7xxx alloys using high levels of Fe alloying have not been investigated.

For example, no previous work was found to determine the relationship between the effect of key process parameters such as the effect of cooling rate, alloy composition and microstructure for the Al-Zn-Mg-Cu-(Fe) system. Thus the primary objective of this thesis is to determine the resulting microstructure of Al-Fe intermetallics as a function of alloy composition at varying cooling rates for AA 7xxx series cast alloy samples. Nine alloys within Al-Zn-Mg-Cu-Fe alloy systems were designed for investigation using a Taguchi L9 factorial analysis method which enables determination of the most significant process factors determining the fraction, morphology and chemistry of the Al-Fe

intermetallics.

This thesis consists of five chapters, where the second chapter consists of an in-depth literature review concerning castability issues and the role of Fe in aluminum alloys within the specific context of die soldering. Chapter three depicts the experimental procedure and design of experiments using a factorial design and the results and interpretations obtained during the study are presented as chapter 4. Finally, the fifth chapter presents the conclusions and outcome of the study.

2. Literature Review

Die soldering and hot tearing are two important castability issues in the near net shape casting of aluminum 7xxx series alloys for automotive chassis and structural applications, where the addition of Fe as an alloying element to 7xxx series alloys is believed to circumvent the problem of die soldering and tendency for hot tearing and, thereby, allow for the processing of a sound casting. It is generally believed that Fe is the most common impurity element that influences poor mechanical properties and casting defects in aluminum alloys [4]. However, it should be noted that Fe does not always exert a negative effect on mechanical properties. For example, Fe is deliberately added as an alloying element to enhance the strength and to minimize the problem of die soldering in the case of high pressure die casting (HPDC) [5, 6]. At present, shape cast 7xxx series alloys have not been successfully used in automotive applications because of severe hot tearing tendencies during solidification, where addition of Fe to these alloys leads to a narrowing of solidification range by the formation of binary and ternary eutectic phases [7].

This literature review will summarize the current state of knowledge concerning the solidification and microstructural evolution of 7xxx series alloys during casting, specifically the effect of iron as an alloying element and its influence on die soldering, microstructural evolution and mechanical properties.

2.1 Die soldering in aluminum alloy casting

Die soldering or die sticking occurs in aluminum alloys when the molten aluminum alloy sticks to the surface of the steel die and remains there after the ejection of the part from the die. It is a very unfavorable phenomenon specific to HPDC because of the increased

equipment downtime, production of faulty castings and, high tooling and die replacement costs [8].

Die soldering usually happens at a temperature higher than the critical temperature of the aluminum alloys, i.e. the critical temperature is the die-surface temperature above which the Al-Fe eutectic phase can form. For example, in the case of Al-Fe binary alloy system, the eutectic temperature is 655 °C. Contact between molten aluminum and the die steel at a temperature higher than a critical temperature results in diffusion taking place between iron and aluminum, resulting in the formation of Fe-Al intermetallic phases and a liquid aluminum-rich FCC phase which subsequently forms an intermediate layer on the die material upon cooling [9].

Shankar and Apelian [3] studied the phenomenon of die soldering between a ferrous die material and an aluminum melt (Al-Si alloy) and determined that die soldering is a diffusion driven reaction in which iron from the tool steel diffuses into the molten aluminum. A series of intermetallic phases formed because of this inter-diffusion phenomenon on to which the aluminum alloy solders to the die material.

Shankar and Apelian [10] investigated the effect of aluminum alloy composition on die soldering with a H-13 tool steel die materials and proposed a six stage interaction mechanism between the molten aluminum alloy and the die material. Figure 2.1 illustrates a detailed summary of their die soldering mechanism between the molten aluminum alloy and steel. Initially, pitting of die surface takes place because of repeated encounters between the molten metal and die surface, resulting in the formation of a primary solid solution of iron and aluminum, as shown in Figure 2.1(a). The subsequently images in Figure 2.1 shows the formation Fe-Al intermetallics (such as FeAl, $FeAl_2$,

Fe_2Al_5 and $FeAl_3$).where Figure 2.1 (b and d) also shows the growth of ternary composition (Al-Si-Fe) "pyramid" which expands laterally and finally merges in molten aluminum causing a soldering phenomenon. A ratio of 1:5 was reported between the Fe-Al intermetallic layer thickness and the soldered aluminum.

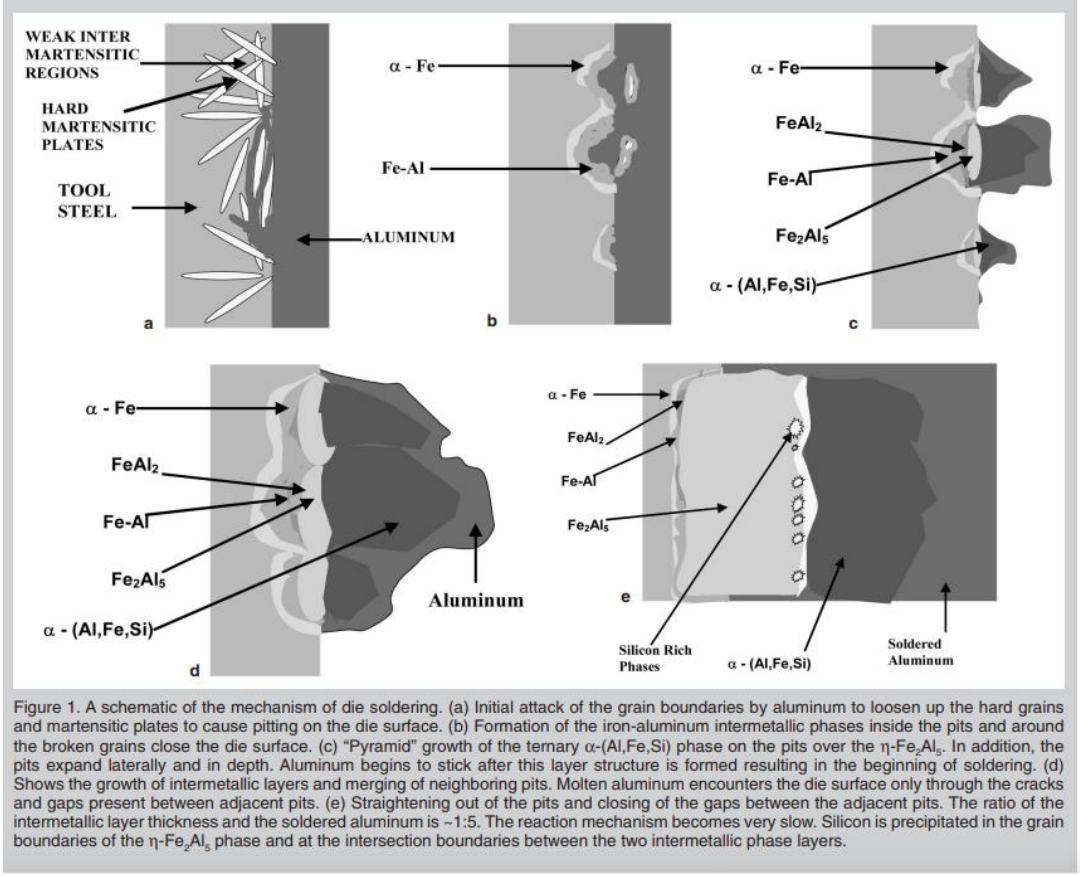

Figure 1. A schematic of the mechanism of die soldering. (a) Initial attack of the grain boundaries by aluminum to loosen up the hard grains and martensitic plates to cause pitting on the die surface. (b) Formation of the iron-aluminum intermetallic phases inside the pits and around the broken grains close the die surface. (c) "Pyramid" growth of the ternary α-(Al,Fe,Si) phase on the pits over the η-Fe_2Al_5. In addition, the pits expand laterally and in depth. Aluminum begins to stick after this layer structure is formed resulting in the beginning of soldering. (d) Shows the growth of intermetallic layers and merging of neighboring pits. Molten aluminum encounters the die surface only through the cracks and gaps present between adjacent pits. (e) Straightening out of the pits and closing of the gaps between the adjacent pits. The ratio of the intermetallic layer thickness and the soldered aluminum is ~1:5. The reaction mechanism becomes very slow. Silicon is precipitated in the grain boundaries of the η-Fe_2Al_5 phase and at the intersection boundaries between the two intermetallic phase layers.

Figure 2.1 Schematic illustration of die soldering mechanism proposed by Shankar and Apelian [10]

Below are the most critical process parameters that affect die soldering [8, 11]:

- temperature of the molten metal and die.
- alloy composition and intermetallic layers.
- die lubrication and coating.
- die design and operating parameters.

In the below text, additional emphasis is given to comprehensively understanding the role of alloy composition and intermetallic layers on die soldering, specifically using iron as one of the major alloying elements in order to reduce the die soldering tendencies.

2.2 Al-Fe binary phase diagram

Iron is always present in commercial aluminum alloys as an impurity element and which is usually considered as detrimental in several ways. Fe is a natural impurity that occurs during aluminum processing from bauxite ores and is very difficult to remove [12]. It is highly soluble in liquid aluminum and exhibits a limited solubility in the solid, where the Fe solubility decreases exponentially as the alloy approaches its solidus temperature, causing the iron to precipitate and form intermetallic compounds with aluminum (e.g. $Al+FeAl_3$) and other alloying elements such as Si, Mg, Ni, Mn, etc., that may be present in the alloy.

Figure 2.2 [12], shows that in the binary Al-Fe system, the maximum liquid solubility of iron is ~1.8 wt % at 655° C (eutectic temperature) which can reach 5 wt% if the melt is held at 800° C.

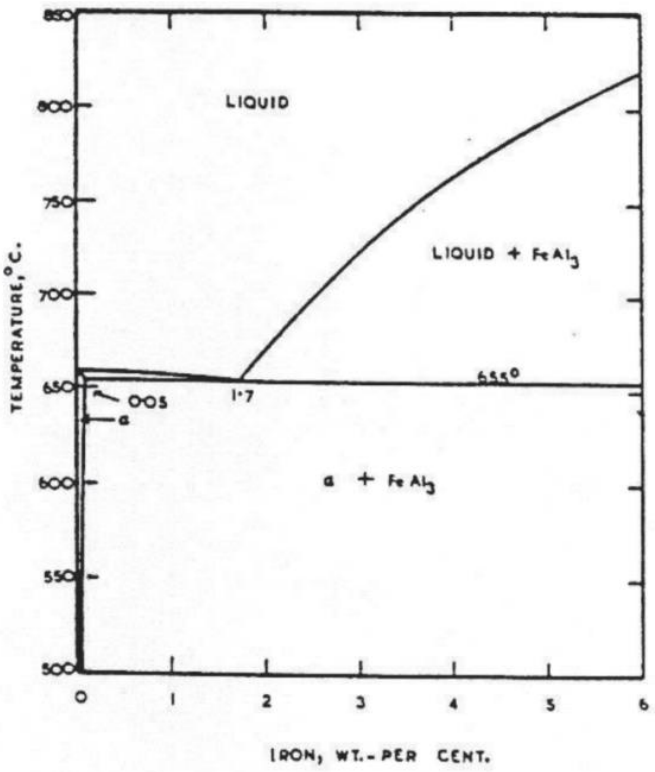

Figure 2.2 Binary Al-Fe equilibrium phase diagram [12]

Table 2.1 [4] shows the solid solubility of iron in Al-Fe binary system during equilibrium solidification; the solubility limits may change as a function of cooling rate during non equilibrium solidification.

Table 2.1 Equilibrium solid solubility of iron in aluminum [4**]**

T (°C)	655	625	600	500	450
Fe (wt%)	0.052	0.043	0.034	0.021	0.005

Taylor [5] reported that aluminum metal typically contains 0.02 to 0.15 wt% iron as an impurity depending upon the initial ore quality and beneficiation processing technologies.

Apart from this baseline value any further activities involving melt processing potentially increase the amount of iron in the melt via two basic mechanisms:

- aluminum melts kept at high temperatures between 700° C to 800° are capable of dissolving up to 5wt% iron from unprotected tool steel die surfaces and furnace equipment
- alloying additions, such as low purity Si and Zn hardners, can also increase the iron level in the melt

2.3 Intermetallics in Al-Fe system

Li et al.[13] identified five intermetallic phases in the aluminum rich corner of the Al-Fe equilibrium phase diagram, namely FeAl, which has a simple BCC structure, and Al rich $FeAl_2$, Fe_2Al_5, and Fe_4Al_{13} with complex triclinic, orthorhombic and monoclinic lattices, respectively. Fe_5Al_8 is a complex phase which has been recently determined to form at high temperatures and will decompose on rapid cooling through a eutectoid reaction.

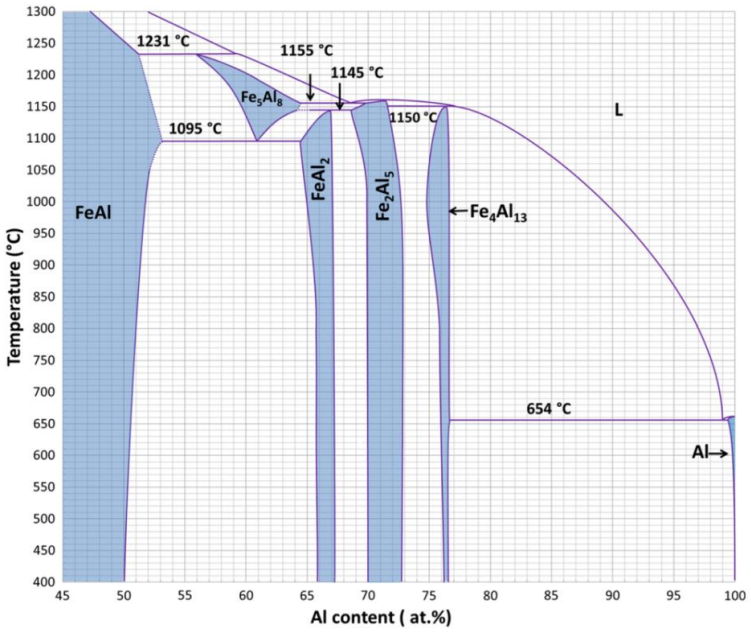

(**A**)

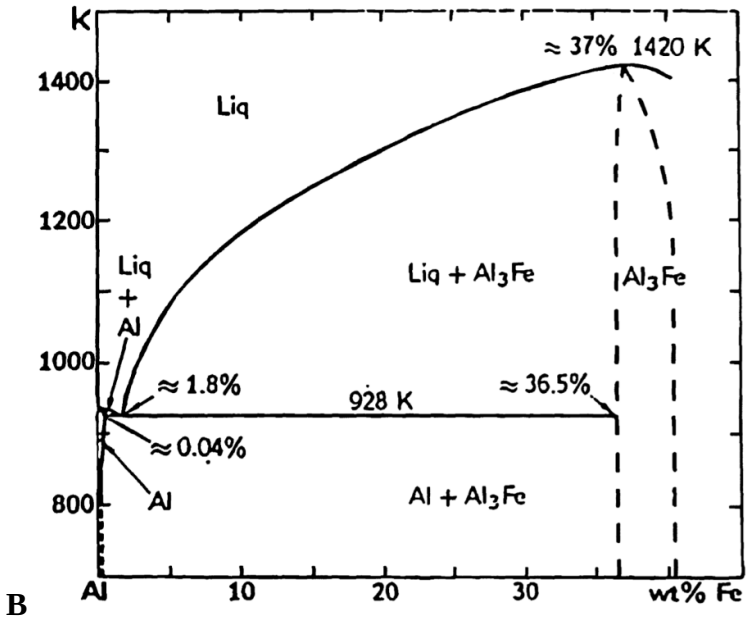

(B)

Figure 2.3 Al–rich end of Al-Fe revised phase diagram (A)
(B) Al-rich Al-Fe equilibrium phase diagram [13, 14]

A revised Al-Fe phase diagram proposed by Li et al. (Figure 2.3 A, [13]) shows that in the aluminum rich corner of the phase diagram, a eutectic reaction occurs at 654 °C, where Al_3Fe (Fe_4Al_{13}) has a very narrow homogeneity range of about 0.5 at.% to 1 at% between 400 °C to 800 °C respectively, the Fe_2Al_5 phase extends from 70.0 to 72.6 at.% Al, and $FeAl_2$ from 65.8 to 67.1 at.% Al.

Allen et al. [14] also conducted extensive research on the evolution of binary and ternary intermetallic phases in AA 1xxx series in both the equilibrium and metastable conditions, Figure 2.3 (B) shows the Al rich part of Al-Fe equilibrium binary phase diagram in which the first phase that forms during solidification of Al-Fe binary alloys in equilibrium condition in given by an eutectic reaction as follows,

Liquid $(\alpha) \longrightarrow$ Al +Al_3Fe (this phase is also denoted as θ phase) Eqn 2.1

The eutectic was reported by Liang and Jones [15] as being 655 °C at 1.8 wt% Fe. This value closely conforms with the eutectic temperature reported by Li et al. [13] as 654 °C but, without any reference to the Fe content in the alloy. Al_3Fe is the equilibrium secondary phase exists over a range of compositions as shown in the Figure 2.3(B).

Commercial alloys are rarely in equilibrium and it is common to find metastable intermetallics depending upon the solidification conditions and alloy composition i.e., it is not possible to determine the intermetallic chemistries or their occurrence from conventional Al-Fe equilibrium phase diagrams under typical non- equilibrium practical casting practices. It has been reported that a eutectic microstructure can be attained by rapidly cooling Al-Fe alloys provided the Fe content is well in excess of 1.8 wt%, which is above the equilibrium eutectic composition [14]. It is further reported in the literature that the Al_3Fe equilibrium phase requires large undercooling to nucleate and grow [14]. Consequently, some of the Al-Fe non equilibrium metastable phases which needs smaller undercooling to nucleate will also form and co-exist in the alloy microstructure under certain solidification conditions.[14]

The common metastable intermetallics are Al_6Fe, Al_mFe, Al_xFe_2, Al_9Fe_2 these phases may coexist with a similar morphology as of the equilibrium phases. Therefore, identification of these phases based on shape alone may be misleading.[14]

Hollingsworth et al [16] identified the displacement of eutectic Al_3Fe by $FeAl_6$ in a continuous cast aluminum alloy with 2 wt% Fe, with a 652 °C eutectic temperature and crystal structure of C-face centered orthorhombic. Kosuge et al. [17] reported that at higher cooling rates (> 10K in a wedge shaped mould for a Al- 0.6 wt% Fe alloy) a metastable Al_mFe eutectic phase appeared rather than Fe_3Al and Al_6Fe which usually

formed at lower cooling rates. This phase has also been observed in the more rapidly cooled zones of DC cast billets.

Allen et al. [14] have determined the eutectic temperature for this phase as 649 °C with 0.3 wt % Fe in the Al-Fe-Si alloy system. The authors also noticed that the eutectic temperature for the Al_3Fe phase for the same alloy was 651 °C, which is higher than the formation temperature of 649.5 °C reported for the Al_mFe phase. The eutectic temperature for this phase in the Al-Fe binary system is not well determined in the literature.

Figure 2.4 shows the composition ranges of the most commonly found metastable intermetallics in ternary Al-Fe-Si alloys. From Figure 2.4 it can be observed that the binary Al_3Fe equilibrium intermetallic and the meta-stable Al_mFe intermetallic has a range of Fe composition from 36 to 38.5 wt% and 31.5 to 34 wt% respectively.

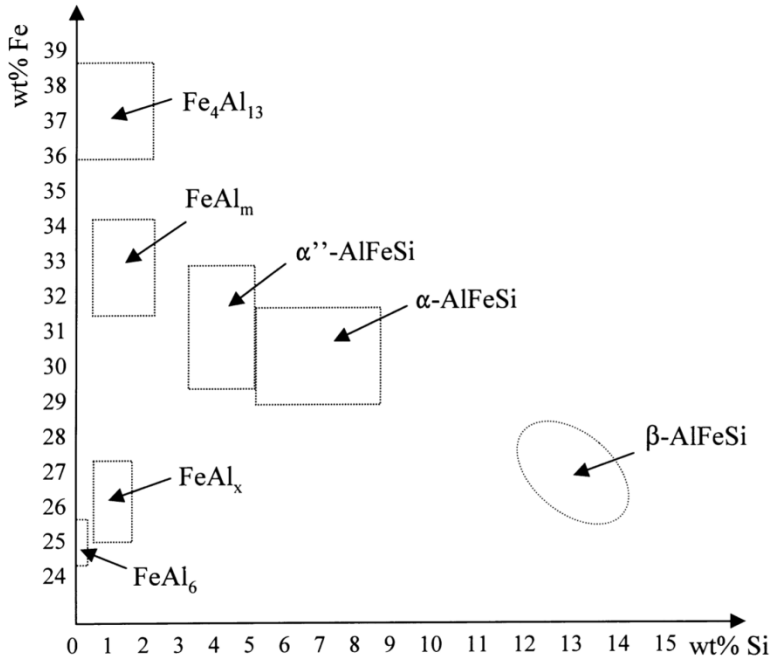

Figure 2.4 Compositions of the common binary and ternary compounds found in Al-Fe-Si alloys by Allen et al. [14].

The transition from phase A to phase B will be depend upon the growth kinetics of the two phases. Two important process parameters which influences the competitive growth of two phases include the critical cooling rate $(dT/dt)_{crit}$ and the critical growth velocity (U_{crit}) these two parameters are related by equation (Eqn 2.2) where, G ($_{grad}T$) is the temperature gradient at the solid liquid interface :

$$\frac{dT}{dt\ crit} = \mathbf{grad T} \ . \mathbf{U_{criti}} \qquad \text{Eqn 2.2}$$

Backerud [18] studied the Al-Fe alloys with 0.5- 4 wt% Fe to determine the variation of eutectic growth temperatures with cooling rate for the Al_3fe and Al_6Fe phases. The author observed that, with increasing cooling rate, the eutectic temperatures for both the phases decreased with different intermetallic fractions in the melt, No specific growth velocity or cooling rates at which the Al_3Fe to Al_6Fe transition occurred was reported. However, the work indicated that both cooling rate and solidification velocity were fundamental factors driving the phase transition.

Adam and Hogan [19] investigated Al-Fe binary alloys with 2 - 4 wt% Fe during unidirectional solidification experiments to understand the variation in eutectic phase and the morphology of that phase with varying growth velocity (U) and temperature gradient ($_{grad}G$) at the solidification front. Figure 2.5 shows the variation in eutectic microstructure with changing U and $_{grad}G$ for different casting conditions. The authors reported that, at high G/U ratios the resultant microstructure was Al_3Fe with a lamellar morphology. As G/U decreased, the eutectic became increasingly branched and the spacing between the

Al_3Fe particles decreased. Further decreases in G/U resulted in transition to a rod-like Al_6Fe based eutectic microstructure from a faceted Al_3Fe morphology.

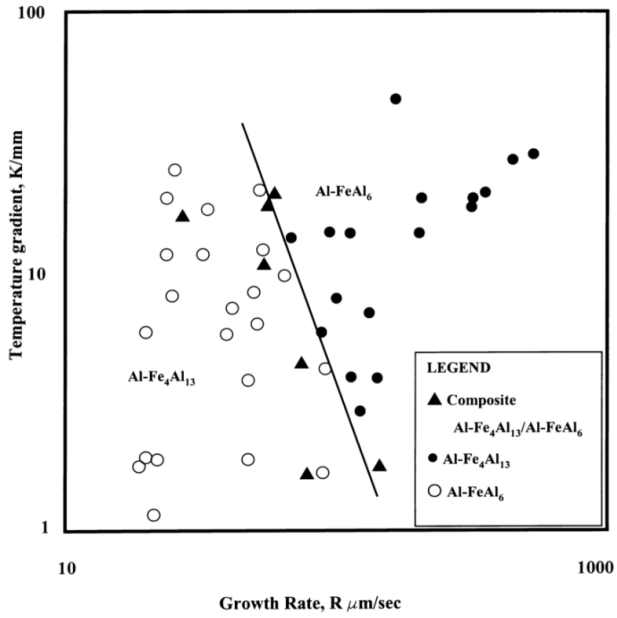

Figure 2.5 Growth rate and temperature gradient conditions imposed on uni-directionally solidified Al - 2 wt% Fe alloys and the resultant eutectic reactions [20]

The value of U_{crit} reported by Adam and Hogan [20] was 100 µm/sec. With such a high solidification velocity the required undercooling for the formation of Al_3Fe particles is greater than that of Al_6Fe and can be kinetically displaced by Al_3Fe provided the nucleation conditions permit it. However, it is difficult to determine a unique cooling rate for the transition. As indicated in Equation 2.1 the value of critical cooling rate ($\frac{dT}{dt\ crit}$) always depends on the temperature gradient ($\mathbf{grad T}$).

Hughes and Jones[20] observed the displacement of Al_3Fe by Al_6Fe in a unidirectionally solidified Al-Fe alloy with 2.2 to 6.1 wt% Fe at a growth velocity of 0.10 mm/s. They

also reported an increased tendency for Al_6Fe rods to cross-link with decreasing U. The critical velocity was observed to be an independent of Fe alloying content.

Young and Clyne, [21] conducted unidirectional solidification experiments to determine the cooling rate at which the displacement occurs between metastable Al-Fe phases in a hypoeutectic Al-Fe alloy. Figure 2.6 shows the observed displacement from Al_3Fe by Al_xFe at 0.7 K/s . Al_3Fe was detected at cooling rates up to 0.9 K /s , Al_xFe in the range 0.5to 6 K/s, Al_6Fe at cooling rates >3 K/s and Al_mFe at cooling rate >10 K/s. The authors claimed that Al_mFe existed as an intermediate phase during the displacement from Al_3Fe to Al_6Fe, and was mistaken as $FeAl_6$ because of its similar morphology. The claim made by Young and Clyne is highly debatable because of the additional literature which does not support this result. Hence, there does not appear to be a unique critical cooling rate for any of these transitions. However, there is a general agreement in the literature that under more extreme solidification conditions Al_6Fe becomes kinetically displaced by Al_mFe [14].

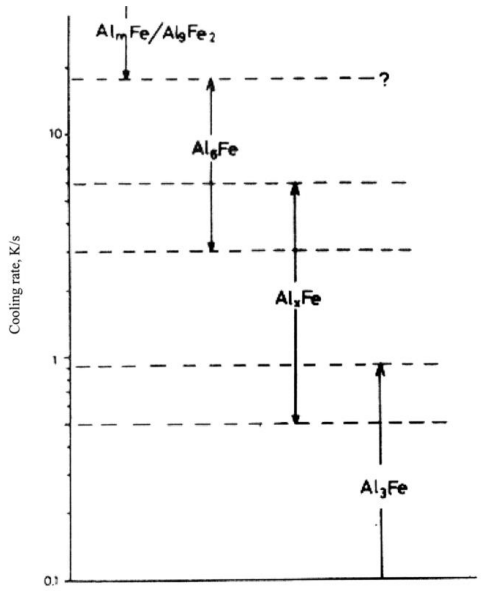

Figure 2.6 Effect of cooling rate on formation of Al-Fe eutectics in hypoeutectic Al-Fe alloys. After Young and Clyne [21]

The focus of this section of the literature review was to understand the formation of different Al-Fe intermetallics and the nature of microstructure during non equilibrium solidification conditions. Based on the equilibrium diagram of Al-Fe and Al-Fe-Si, it is reported that Al_3Fe is a most common intermetallic that precipitates during solidification and forms in the interdentritic spaces, The eutectic temperature was reported around 655 ±2 °C [12,13,14,15] . However, during non equilibrium solidification conditions (higher cooling rates) a number of metastable intermetallics such as Al_6Fe, Al_XFe, Al_mFe have been reported. Also, in the alloys having high Fe levels, the displacement of Al_3Fe by Al_6Fe was commonly observed by many researchers at high cooling rates and different solidification conditions [14,16,18,19,20,21]. The transition from Al_3Fe by Al_6Fe occurred depending upon the growth rate and temperature gradient conditions during solidification. The resultant changes in the morphologies were also observed during this transition.

The results obtained from the proposed research work are very consistent with the general agreement noted in the above literature. The Al-Fe intermetallics formed during the unidirectional solidification experiment at different cooling rates shows a transition trend from Al_3Fe by Al_6Fe at relatively higher cooling rates and also the morphology changes occur during this transition from high to low aspect ratio Al-Fe intermetallics.

2.4 Al-Fe intermetallic morphology

Mbuya et al. [22] reported that, in aluminum alloys, Fe-Al intermetallics forms with various morphologies that includes small needles, large platelets, Chinese script, hexagonal, star like, polyhedral and with irregular shapes.[22].The evolutions of intermetallics, morphologies, size, distribution etc., are greatly influenced by the solidification parameters and the alloy composition. It is a complex phenomenon to understand specifically for multi-component alloy systems with varying solidification parameters. As stated earlier, a high level of Fe can be added to die casting alloys to eliminate or alleviate die soldering. Generally, Mn or Cr are also added to die casting alloys to alter the morphology of the mechanically detrimental needle shaped Fe bearing intermetallics to less detrimental ones. The resultant complex intermetallic compounds (Al-Fe-Mn-Cr) with large crystals have been categorized as sludge [8].

Makhlouf and Apelian [8] investigated the casting characteristics such as die soldering tendency, melt fluidity, alloy machinability and sludge formation trends for the various die casting aluminum alloys shown in Table 2.2. It was reported that the Fe:Mn:Cr ratio in the alloy contributed to sludge formation with the cooling rate playing an important role in the resulting morphologies and distribution of the particles. An increase in Fe content intensified the sludge formation and its formation temperature. The authors also noticed a decrease in the size, amount, and volume fraction of Al-Fe intermetallics with higher cooling rates.

Table 2.2 Alloy composition used for casting characteristics studies [8]

Alloy No.	Composition* (%)										
	Si	Cu	Fe	Mn	Mg	Ni	Cr	Zn	Ti	Sr	Others Total
1	13.0	5.0	1.6	0.25	0.50	0.25	0.05	3.0	0.20	<0.02	0.50
2	7.0	1.25	0.7	0.50	0.05	0.05	0	3.0	0.20	0.02	0.50
3	13.0	5.0	1.2	0.50	0.25	0.25	0.05	3.0	0.20	<0.02	0.50
4	7.0	1.25	0.7	0	0.05	0.25	0.15	0.50	0	<0.02	0.50
5	7.0	1.25	0.7	0.25	0.05	0.05	0	3.0	<0.2	<0.02	0.50
A380.0	7.5-9.5	3.0-4.0	1.3	0.50	0.10	0.5	-	3.0	-	-	0.50

Shebhasthari et al. [23] also investigated sludge forming trends for aluminum based alloys (Al-12.7Si) with various alloy composition, holding temperatures and cooling rates. They noted the same trend as mentioned by Makhlouf and Apelian [8] and provided an exponential equation that correlated the sludge forming temperature and the alloy Fe content per equation 2.2

$$\textbf{Temperature (C)} = 645.7 + 34.2\,(\%\text{Fe})^{2} \qquad \text{Eqn 2.3}$$

It should be noted that the formation of sludge increased the die-soldering tendency of the alloy and affected the melt fluidity. The complex sludge crystals were composed mainly of Fe and Mn-rich compounds and their formation causes a depletion of Fe and Mn in the melt, which increased the chemical potential gradient between the alloy melt and steel die [8]. Equation 2.2 assists in reducing the tendency for die soldering by optimizing the alloy chemistry and the holding temperature.

2.5 Effect of Al-Fe intermetallic on mechanical properties

In general, Fe is considered as an unwanted impurity and is detrimental in aluminum alloys for several reasons, although, the presence of Fe has proved to be beneficial in improving some casting issues like die soldering and hot tearing in die casting [24].

Al-Fe intermetallics tend to negatively affect alloy mechanical properties depending upon their size, morphology and the distribution of the primary intermetallics [5]. The increase in Fe content beyond a critical level in terms of alloy composition can increases the porosity in the alloy and result in a defective casting [5]. It also reduces the machinability and fluidity of the alloy [8].

Wang et al. [6] carried out a detailed investigation of Al-Si high pressure die casting alloys for the 16 alloy compositions shown in Table 2.2 based on a L_{16} orthogonal array of alloy design of experiments. The Fe level in these experiments was kept as low as possible and ranged from 0.7 to 1.6wt%. The authors performed an ANOVA analysis to understand the effect of different elements on the major mechanical properties. Table 2.3 shows the average room temperature tensile properties for alloys 1-16, where the authors reported a slight increase in the modulus of elasticity of 7.77 GPa, the ultimate tensile strength was slightly decreased by 1.1 MPa, and the average yield strength was increased slightly by 8.6 MPa with an increase in alloy Fe content from 0.6 to 1.7 wt%. There was a drastic decrease in the average percent elongation of 1.64 % (from 3.24 to 1.60 %) with the increase in alloy Fe. The pooled ANOVA analysis results showed that the contribution of Fe content towards the decrease in tensile strength was negligible compare to other elements. It is generally believed that the tensile and yield strength

were adversely affected by iron rich intermetallic particles but, still there seems to be a lack of general agreement about the degree of influence on mechanical properties.

Table 2.3 Alloy composition based on a L_{16} orthogonal array of alloy design of experiments [6]

Alloy No.	Composition (%)									
	Si	Mg	Fe	Cu	Ni	Cr	Mn	Ti	Zn	Sr
1	7.15	0.03	0.68	1.24	0.01	0.01	0.01	0.01	0.44	0.000
2	6.99	0.01	0.56	1.15	0.01	0.01	0.47	0.24	2.87	0.018
3	6.98	0.04	1.49	4.99	0.44	0.13	0.01	0.01	0.47	0.018
4	6.94	0.04	1.48	4.74	0.47	0.15	0.45	0.16	2.69	0.000
5	7.05	0.44	0.67	1.18	0.53	0.14	0.01	0.01	2.76	0.000
6	6.98	0.44	0.57	1.13	0.48	0.13	0.45	0.18	0.38	0.018
7	6.92	0.50	1.63	4.94	0.03	0.01	0.02	0.01	2.73	0.022
8	6.79	0.46	1.49	4.77	0.01	0.01	0.45	0.20	0.42	0.000
9	12.71	0.05	0.63	4.96	0.06	0.14	0.01	0.20	0.50	0.017
10	12.69	0.03	0.73	5.09	0.07	0.11	0.37	0.01	2.73	0.000
11	12.86	0.04	1.59	1.21	0.45	0.01	0.01	0.18	0.49	0.000
12	12.95	0.05	1.55	1.29	0.46	0.01	0.43	0.01	2.91	0.023
13	13.03	0.46	0.58	4.70	0.44	0.01	0.01	0.17	2.61	0.021
14	12.94	0.48	0.74	4.77	0.50	0.01	0.57	0.01	0.55	0.000
15	12.78	0.47	1.51	1.27	0.06	0.14	0.01	0.18	2.94	0.000
16	12.86	0.41	1.63	1.21	0.06	0.14	0.44	0.01	0.46	0.024

Table 2.4 Summary of average room temperature tensile properties for alloy 1-16 [6] Documented in Table 2.3

Alloy No.	Tensile Strength			Yield Strength			Elongation			Modulus of Elasticity		
	Average	St. dev.*	CV**	Average	St. dev.	CV	Average	St. dev.	CV	Average	St. dev.	CV
	(ksi)	(ksi)	(%)	(ksi)	(ksi)	(%)	(%)	(%)	(%)	(ksi)	(ksi)	(%)
1	39.6	0.9	2.3	16.6	0.4	2.4	5.85	0.97	16.6	10,536	1,024	9.7
2	42.4	0.8	1.9	20.0	0.4	2.0	7.43	1.18	15.9	10,915	753	6.9
3	45.4	1.0	2.2	24.8	0.3	1.2	2.08	0.23	11.1	11,262	753	6.7
4	47.0	0.9	1.9	25.5	0.4	1.6	2.81	0.29	10.3	11,079	746	6.7
5	44.4	0.7	1.6	24.9	0.3	1.2	3.76	0.52	13.8	10,671	427	4.0
6	46.2	1.5	3.2	24.9	0.5	2.0	3.78	0.75	19.8	11,008	748	6.8
7	49.1	0.6	1.2	32.2	0.6	1.9	1.42	0.08	5.6	11,435	687	6.0
8	48.9	0.9	1.8	30.0	0.3	1.0	1.93	0.19	9.8	11,111	385	3.5
9	46.8	1.8	3.8	27.5	0.4	1.5	1.69	0.29	17.2	11,583	685	5.9
10	44.3	2.4	5.4	28.2	0.4	1.4	1.40	0.37	26.4	11,420	539	4.7
11	35.1	2.0	5.7	23.8	0.5	2.1	0.75	0.13	17.3	11,621	595	5.1
12	40.4	2.2	5.4	23.3	0.4	1.7	1.42	0.32	22.5	11,418	826	7.2
[illegible]	47.2	1.6	3.4	31.0	0.5	1.6	1.39	0.24	17.3	11,552	391	3.4
14	41.9	4.0	9.5	32.9	0.7	2.1	0.67	0.32	47.8	11,644	389	3.3
15	42.6	2.1	4.9	29.2	0.4	1.4	0.97	0.17	17.5	11,639	562	4.8
16	43.0	2.5	5.8	26.9	0.4	1.5	1.41	0.39	27.7	11,620	700	6.0

*St. dev. - Standard deviation **CV - Coefficient of Variation (= St. dev./Mean 100%)

Some researchers have reported a slight increase in the tensile and yield strength with an addition of iron Fe while the majority of the researchers reported a decrease in tensile and yield strength of the alloy with increase in Fe levels [5, 6, 8, 6, 25, 26]. However, extensive literature is available to support the argument that the fracture toughness, ductility, fatigue resistance and impact resistance will be affected negatively with an increase in alloy Fe levels.

Murali et al. [26] have studied the effect of Fe in Al-7Si-xMg-yFe alloy on the observed mechanical properties and fracture toughness for Fe contents from 0.2 to 0.8 wt%. Figure 2.7 shows the mechanical properties of alloys with various Fe content having 0.65 and 0.32 wt% Mg respectively. They have reported a significant drop of yield strength, UTS.

The elongation was drastically reduced from 4 to 2 % in both the alloys with an increase in alloy Fe content. They have also shown that the higher value of alloy Fe contents above the critical value of 0.3 wt% resulted in a significant reduction of fracture toughness and impact resistance.

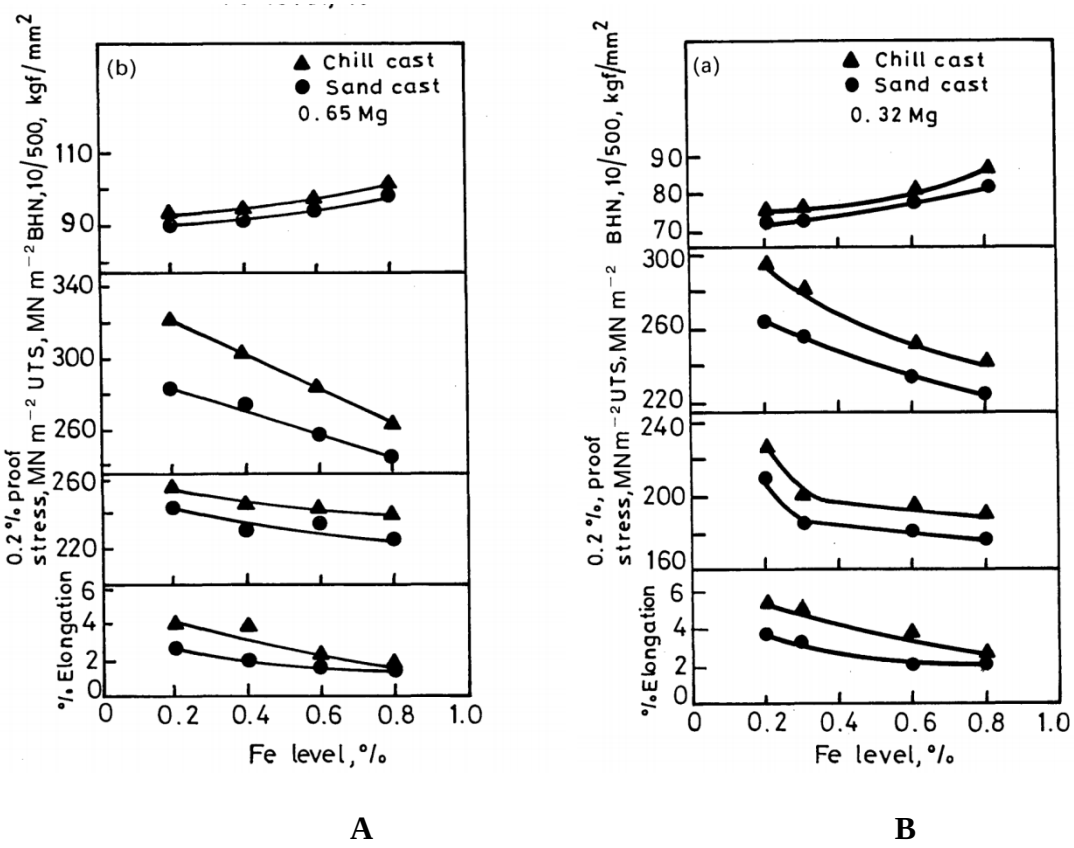

A **B**

Figure 2.7 Effect of Fe content on mechanical properties (A) 0.65 %Mg (B) 0.32% Mg [26]

Ji et al. [27] studied the effect of Fe on the microstructure and mechanical properties of Al-Mg-Si and Al-Mg-Si-Mn die cast alloys by maintaining the constant process parameters for both the experiments shown in Table 2.3. The Fe was added in the range of 0.2 to 1.8 and 2.4 wt% respectively. Figure 2.8 [A] shows the effect of Fe (wt%) on the average particle size distribution of both the alloys and shows, there was no

significant variation observed in the average size of the particles within the experimental range

Figure 2.8 [B] shows that the solid fraction of the intermetallics was increased with the increase in iron content, as would be expected from the global mass balance.

Table 2.5 Composition of die cast Al-Mg-Si alloy used for experiments [27]

Alloy	Si	Fe	Mn	Mg	Ti	Zn	Others	Al
A	2.2 ± 0.08	varied*	0.541 ± 0.05	6.2 ± 0.08	0.17 ± 0.04	0.012 ± 0.004	< 0.03	Bal.
B	1.9 ± 0.07	varied[a]	0.023 ± 0.04	5.6 ± 0.09	0.15 ± 0.04	0.013 ± 0.004	< 0.03	Bal.

* Actual Fe contents were measured to be 0.214, 0.389, 0.623, 0.841, 1.243, 1.490, 1.861, and 2.482, respectively.
[a] Actual Fe contents were measured to be 0.086, 0.414, 0.634, 0.911, 1.188, 1.420, 1.542, and 1.821, 2.453, respectively.

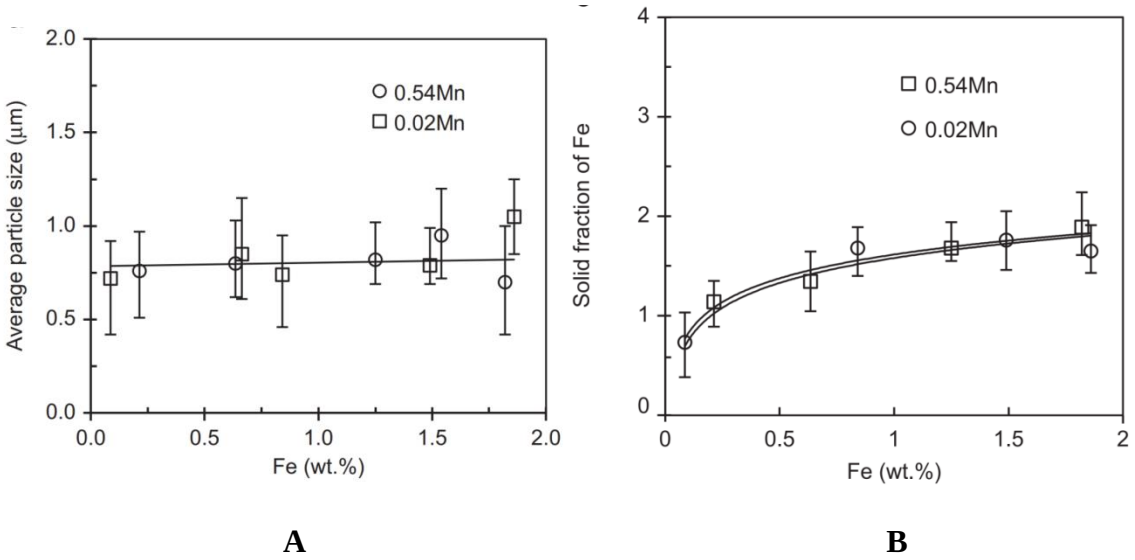

A **B**

Figure 2.8 [A, B] Effect of Fe content on the (A) average size and (B) solid fraction of the Fe intermetallic particles [27].

The authors also reported a slight enhancement in the yield strength and a drastic decrease in the elongation with the increase in the alloy iron content as shown in Figure 2.9 [A and C], respectively. The UTS did not show significant change from the lower to

higher levels of Fe but, a minimal reduction can be observed beyond 0.6 wt% Fe, as shown in Figure 2.9 [B].

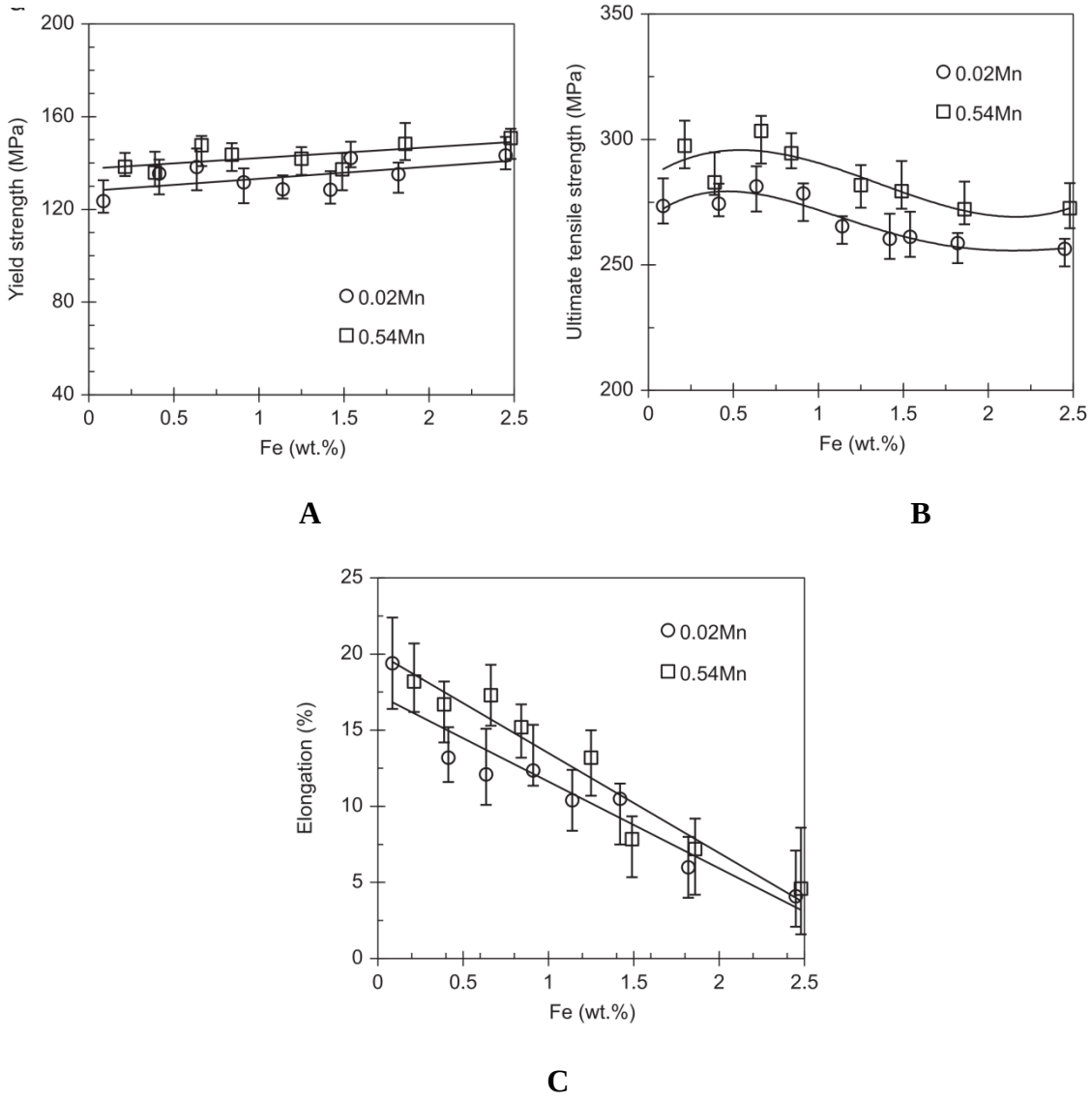

Figure 2.9 [A, B, C] Effect of Fe content on the (A) yield strength (B) ultimate tensile strength and (C) elongation of alloys [27].

Ji et al. also observed a significant effect of alloy Fe and Mn contents on the morphologies of primary Al-Fe intermetallics during HPDC. Figure 2.10 [A, B] shows a microstructure of alloys having 0.21 and 0.09 wt% Fe, respectively. A fine microstructure

with a small amount of Fe intermetallics (labelled as Fe_2) was observed, most of the intermetallics were located on the grain boundaries. No primary AL-Fe intermetallics were observed in the primary α-Al phase (labeled as α_1-Al). The typical composition of the Fe intermetallics were $Al_{24}(Fe,Mn)_6Si$ and $Al_8(Fe,Mn)_2Si$.

Figure 2.10 [C, D, E, F] shows the alloy microstructures having 0.62, 0.62, 1.24 and 1.19 Fe wt% respectively. When the alloy Fe content increased, two types of Al-Fe intermetallics were observed (labeled as Fe_1 and Fe_2) respectively. The Fe_1 intermetallics were usually located on the primary α-Al phase boundary and exhibited a coarse compact morphology, which were found in to tetragonal, pentagonal, hexagonal and needle shaped morphologies. The typical composition of these intermetallics was Al_8FeSi and Al_3FeSi specifically for the needle shaped morphologies. Figure 2.10 [G,H] shows that, when the alloy Fe content was further increased to 1.8 wt%, high aspect ratio needle shaped Al-Fe intermetallics were predominantly found in addition to the compact Al-Fe intermetallics. The typical composition of the needle shape morphologies was observed to be Al_3FeSi.

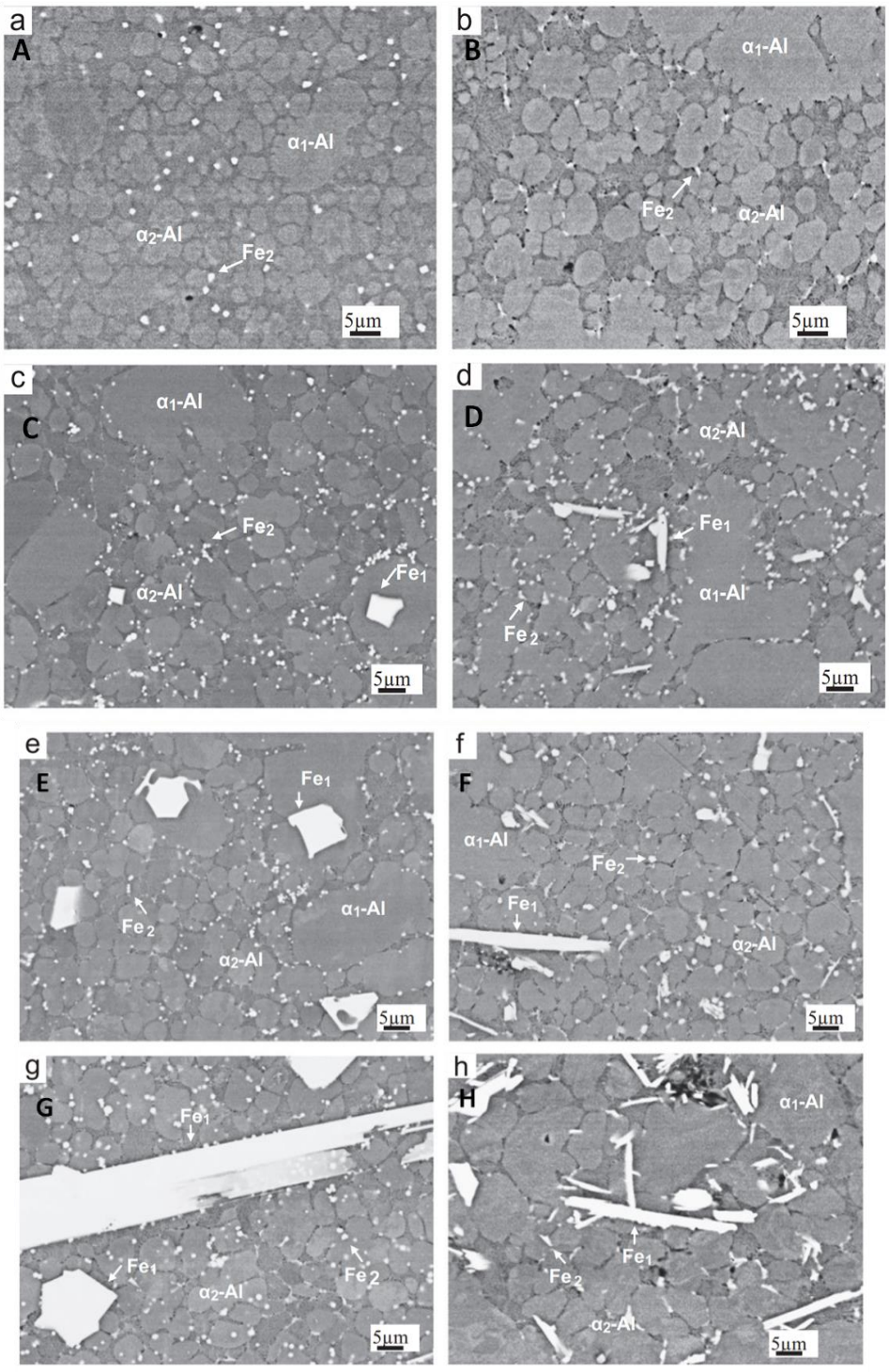

Figure 2.10 [A,B,C,D,E,F,G,H] SEM micrographs of Fe-rich intermetallics in the diecast alloy with different amounts of Fe and Mn (A) 0.54Mn, 0.2 1Fe, (B) 0.02Mn, 0.09 Fe, (C) 0.54Mn, 0.62Fe, (D) 0.02Mn,0.62Fe, (E) 0.54Mn, 1.24Fe (F) 0.02Mn,1.19Fe (G) 0.54Mn, 1.86Fe, (H) 0.02Mn,1.82Fe [27].

2.6 Effect of Fe on castability

It is evident from § 2.1 that the high level of Fe close to its saturation level of 1.3wt% in Al die casting alloys is beneficial in preventing the die soldering tendencies. But, it is always important to keep the Fe levels as low as possible without compromising the mechanical properties. Different casting processes require specific characteristics for the alloy, but in general some critical properties affecting castability are fluidity, resistance to porosity and low hot tearing tendencies for the alloy.

Gowri and Samuel [28] studied a AI-Si-Cu-Mg-Fe (AA380) alloy with 1 to 1.7 wt% Fe, and reported that the fluidity of the alloy decreased with the increase in Fe content. Wang et al. [6] attributed this decrease in fluidity to the increased amount of insoluble intermetallics that formed with the higher Fe content in the alloy. Porosity issues also arose with the decrease in fluidity, which caused improper feeding characteristics in die casting resulting in shrinkage void formation.

It has been reported that a higher Fe content in aluminum alloys increases the high temperature strength of the alloy and also increases the hot tearing resistance. Lisa et al. [29] reported that there was no hot tearing in AA6060 alloys up to 0.22 wt% Fe and, for alloys containing above 0.3 wt% Fe, resistance to hot tearing was high because of the early precipitation of Al-Fe intermetallics significantly increases the eutectic feeding during solidification.

2.7 Effect of Iron on die soldering

Makhlouf et al. [8] reported that the Fe content in the aluminum die cast alloy has a major influence on die soldering; where the addition of Fe close to its maximum liquid solubility value of 1.8wt% saturated the melt at the pouring temperature (660-720° C) and, hence, prevented the diffusion of iron from the die material (H-13). They have also observed no hot tearing in one of the die casting aluminum alloy with 1.84 wt% Fe.

Shankar and Apelian [11,30] studied the AA3xx series of die casting alloys with L-9 and L-16 Taguchi experimental matrices to understand the effect of seven alloying elements on die soldering (refer § 2.1 die soldering in aluminum alloys) .Figure 2.10 shows that Fe has strong effect on the growth of intermetallic layers, where the percentage contribution determined through ANOVA for Fe towards the thickness of the die intermetallic layer was approximately 56% and the contribution of overall alloy chemistry towards die soldering with the H-13 die steel was around 65%. Shankar and Apelian [11.30] also proposed a limiting Fe range between 0.9 to 1.15 wt% Fe to mitigate die soldering.

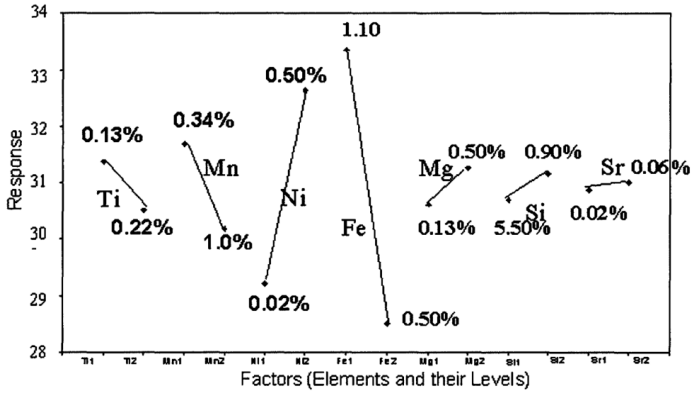

Figure 2.11 Effects of various elements on the thickness of the intermetallic layer in the reaction between H13 and molten aluminum [11]

3. Experimental Methodology

3.1 Alloy matrix design

Nine Al-Zn-Mg-Cu-Fe alloys were designed using an L9 experimental Taguchi orthogonal array with three distinct concentrations of each alloying element. Table 3.1 shows the target factorial levels of the elements and Table 3.2 shows the resulting alloy compositions.

Table 3.1 Factorial matrix for Taguchi designed alloys

Factors	Factorial Level		
	1	**2**	**3**
Zn	3.5	5	6.5
Mg	1.5	2	2.5
Cu	0	1.2	2.4
Fe	0	1.3	2

Table 3.2 Taguchi L9 alloy composition design.

Alloy	**Zn(wt%)**	**Mg(wt%)**	**Cu(wt%)**	**Fe(wt%)**
1	3.5	1.5	0	0
2	3.5	2.0	1.2	1.3
3	3.5	2.5	2.4	2
4	5.0	1.5	1.2	2
5	5.0	2.0	2.4	0
6	5.0	2.5	0	1.3
7	6.5	1.5	2.4	1.3
8	6.5	2.0	0	2.0
9	6.5	2.5	1.2	0

3.2 Alloy preparation

The alloys were prepared at the Light Metal Casting Research Center (LMCRC) at McMaster. The nine experimental alloys were prepared using master alloys of Al-68Mg, Al-33Cu, Al-25Fe, and pure Zn and Al ingots. The input materials (except the Mg-containing alloy) were cut to appropriate weights to make 18kg (40 lb) ingots of the desired alloys, then melted inside a graphite crucible using an electric resistance furnace. The melt temperature was held at 800°C for homogenization and then the Mg-containing master alloy was added just before pouring to avoid oxidation losses of Mg from the melt.

The composition of the precast material samples prepared for the (para-equilibrium and directional) solidification experiments was measured using McMaster's Yvon Horiba Glow Discharge Optical Emission Spectrometer (GD-OES). The results are presented in the Table 3.3, which shows the alloy compositions are consistent with the targeted values range for Zn, Mg, and Cu. However, the Fe content of Alloy 1, 5 and 9 are different (higher) than the targeted values because of the usage of wrong master alloy with high Fe content.

Table 3.3 Average composition of experimental alloys (determined using GD-OES)

Alloy	Zn (wt %)	Mg (wt %)	Cu (wt %)	Fe (wt %)
1	3.5	1.5	0	2.2
2	3.6	2.1	1.2	1.3
3	3.6	2.4	2.3	2.5
4	5.6	1.5	1.8	2.6
5	5.4	2.2	2.2	2.3
6	5.2	2.6	0	1.3
7	6.7	1.5	2.4	1.4
8	6.9	2	0	2
9	7	2.5	1.5	2.1

3.3 Sand mold preparation

The sand mold for the directional solidification experiments was designed based on the standard Jominy experimental set up and was prepared at the Canmet MATERIALS laboratory (Hamilton, ON). Foundry grade silica sand (AFS 75) premixed with 1.3wt% ALPHASET© binder was used to make the casting molds. An 18cm diameter circular mold was designed and fabricated with a 3cm diameter central cylindrical cavity, as shown in Figure 3.1(A).

A 76mm square by 0.4mm thick Cu plate was placed in the bottom of the mold. The purpose of the Cu plate was to contain the melt and to maintain the unidirectional heat transfer from the melt to the cooling liquid. Thermocouple slots were placed in the silica sand mold at various distances in the longitudinal direction from the quenching surface, as shown schematically in Figure 3.1(B).

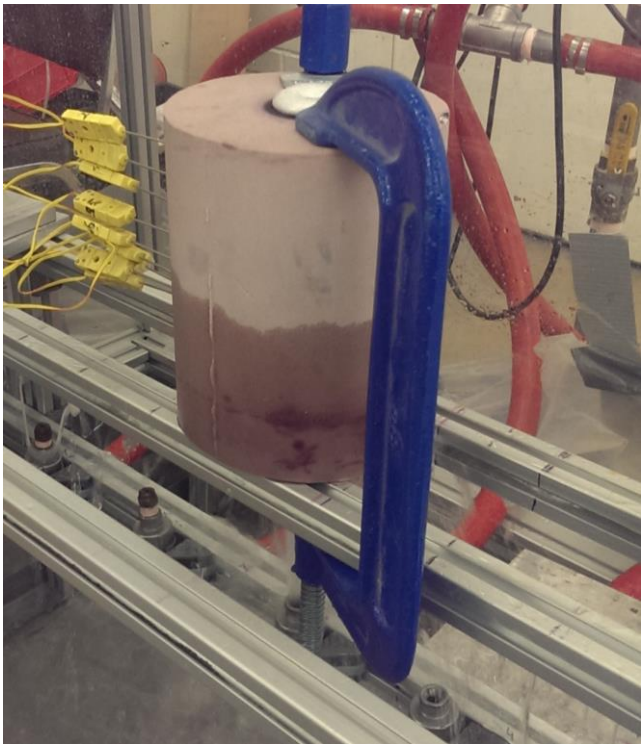

(A)

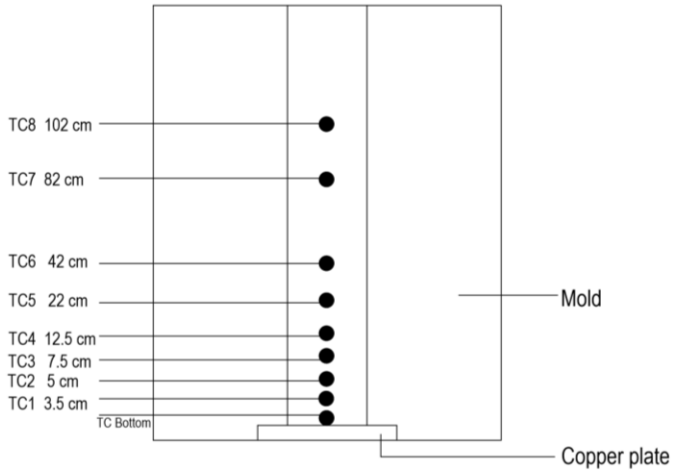

(B)

Figure 3.1 (A) Silica sand mold mounted on the support fixture (B) Schematic diagram of the silica sand mold showing thermocouples locations

3.4 Directional solidification experimental setup

The directional solidification experiments were carried out using a HiperMag test rig located in the LMCRC at McMaster. The test rig consisted of a centrifugal pump connected to a full cone spray nozzle via a manifold controlled by a solenoid valve and then a pressure transducer as shown in Figure 3.2.

The experimental setup was situated inside a PMMA chamber, which also contained the mold mounting platform, spray nozzle, and water-collection tank.

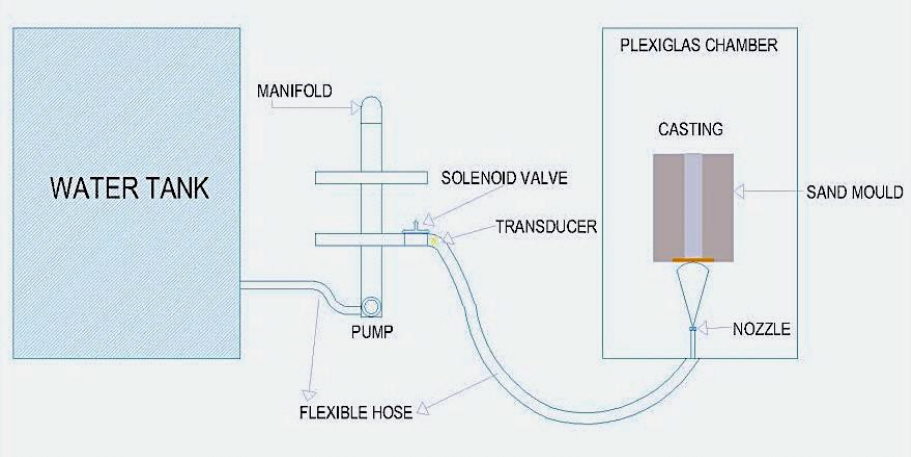

Figure 3.2 Directional solidification experimental setup

3.5 Experimental procedure

The directional solidification experiments were carried out using the following procedure.

1) An 800 g alloy piece was cut from the precast ingot
2) The 800 g alloy piece was melted in the clay crucible using a box furnace set at 760 °C

3) The mold was pre heated at 200 °C to remove moisture
4) The mold was centre mounted on top of the nozzle with clamping bolts. The standoff distance was 12.5cm between the Cu plate and the nozzle edge
5) A set of 1.5 mm diameter K type nickel (Ni)-chromium (Cr) sheathed thermocouples were inserted into the mold slots: locations as shown in Figure 3.1(B)
6) The thermocouples were connected to a data acquisition system and checked for proper operation before pouring.
7) The melt temperature was raised to 800 °C just before pouring to compensate for heat losses during the pouring. A hand held thermocouple probe was used to ensure that the melt was at the target pouring temperature.
8) The water jet was turned on when the melt pour started so that the Cu cold plate was under a constant water stream. The jet pressure was kept at 558kPa (80psi) until the melt sample was completely solidified.
9) The temperature data were recorded for all the thermocouples using the National Instrument data acquisition system with a sampling frequency rate of 1 Hz.

3.6 Sample preparation

A typical directionally solidified ingot with thermocouples embedded is shown in Figure 3.3. The solidified samples were cut in half along the solidification direction and circumferential slices were made at all the thermocouple locations. Eight samples for microstructural examination were prepared from each ingot, starting from the

thermocouple location 2 (located 3.5 mm above the Cu quench plate) to thermocouple location 9 located 102 mm above the Cu quench plate).

Thermocouple 1 was excluded from the analysis because of its direct contact with the cold Cu quench plate and, thus, the measured cooling rate too fast and likely yielded an unrealistic microstructure.

Samples were mounted in hot mounted Bakelite© using a standard compression molding machine and mechanically abraded using an automatic polisher. Specific details of the surface preparation sequence used for each mounted sample are summarized below:

1) SiC abrasive papers with 300, 600 and 1200 grit sizes were used to grind the samples using water as lubricant at 240rpm and 20N applied force for 3mins on each paper.
2) 9 μm non aqueous diamond suspension on an Ultra-Pol©(Silk) cloth at 150 rpm using 20 N applied force for 3 min.
3) 3 μm diamond suspension on a Trident© cloth at 150 rpm with 20N applied force for 5 mins.
4) 1 μm diamond suspension on a Trident© cloth at 150 rpm with 20N applied force for 5 min.
5) 0.05 μm aqueous colloidal alumina suspension on a Chem-pol© cloth disc at 120 rpm with a 15 N applied force for 5 min.
6) The abraded working surfaces were cleaned with running distilled (DI) water after every grinding and polishing step. After the final polishing, the mounted samples

were immersed in an ethanol bath and placed in an ultrasonic cleaner to remove any polishing compounds remaining on the working sample surfaces.

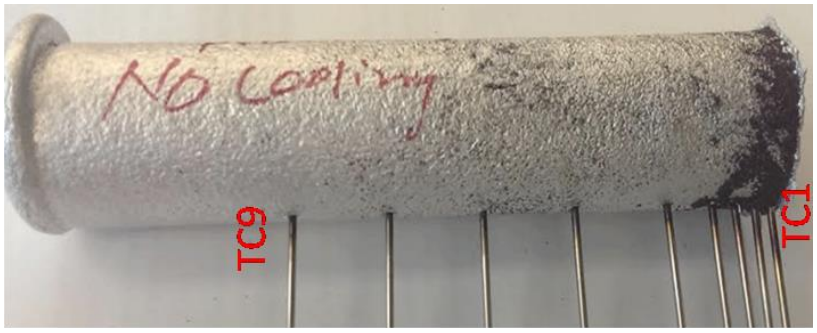

Figure 3.3 As-cast sample showing thermocouples embedded

3.7 Thermal analysis

The near para-equilibrium liquidus and solidus temperature for each alloy was measured by melting the precast ingots in a ceramic crucible in a box furnace then cooling slowly to room temperature while recording the melt temperature. At the liquidus, the slope of the cooling curve changed significantly and, the associated temperature was determined by plotting the derivative of temperature vs time.

During directional solidification experiments, the time vs temperature data for all nine thermocouples was recorded using a National Instrument data logging system.

A set of time vs temperature profiles obtained during directional solidification experiment for Alloy 2 are shown in Figure 3.4 (A) and the derivative curve for thermocouple 2 of the same alloy shown in Figure 3.4(B).

In the directionally cast ingots, the time taken for each thermocouple to drop to the solidus temperature represented the local solidification time. By comparing the

solidification time and the distance between the thermocouples, the solid-liquid interface velocity was determined.

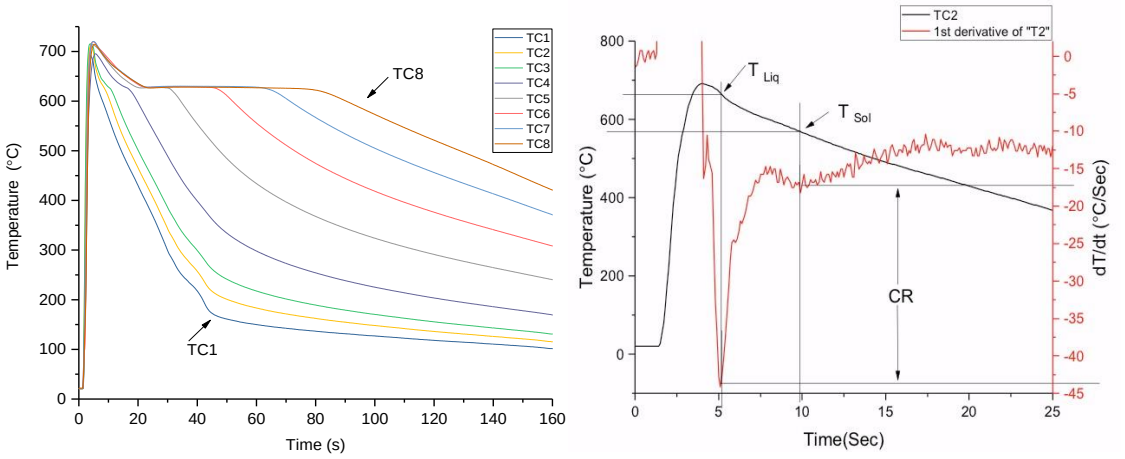

(A) (B)

Figure 3.4 (A) Thermal curves from thermocouple 1-9, (B) cooling rate for thermocouple 2 with T solidus and T liquidus points.

3.8 Microstructural characterization

3.8.1 Scanning electron microscopy (SEM)

A JEOL 6610 SEM was used to examine the microstructure of the as-cast samples. Eight samples for analysis were prepared from each directionally solidified casting (one per thermocouple location 2-9) and were carbon (C) coated to create a conductive surface for optimal SEM viewing. Ten randomly selected fields on every sample were imaged at 1000x magnification (12keV accelerating voltage using, a 10 mm working distance). Ten random fields were chosen to provide a statistically significant data size. Energy dispersive X-ray spectroscopy (EDS) maps were taken from each field to map the distribution of the element of interest. The EDS detector was calibrated for every sample

using a pure Cu strip. Figure 3.5 shows an example of a backscattered electron image of alloy 7 at TC1 location; the corresponding EDS scan is shown in Figure 3.6.The individual elemental maps (Al, Cu, Mg, Zn, and Fe) acquired from EDS scan (Figure 3.6) are shown in Figure 3.7 (A-E) respectively

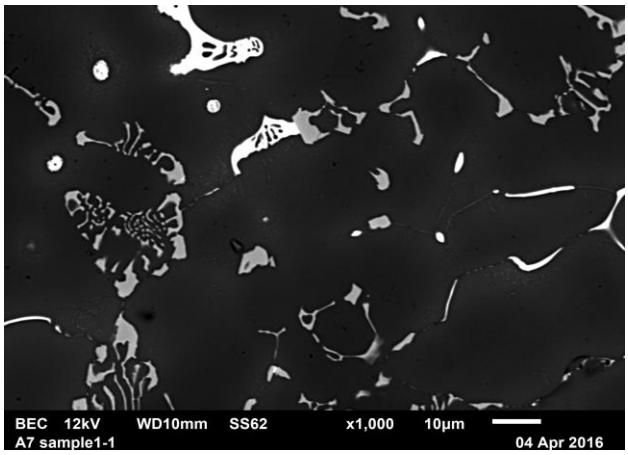

Figure 3.5 Backscattered Electron Image of Alloy 7 @ TC1

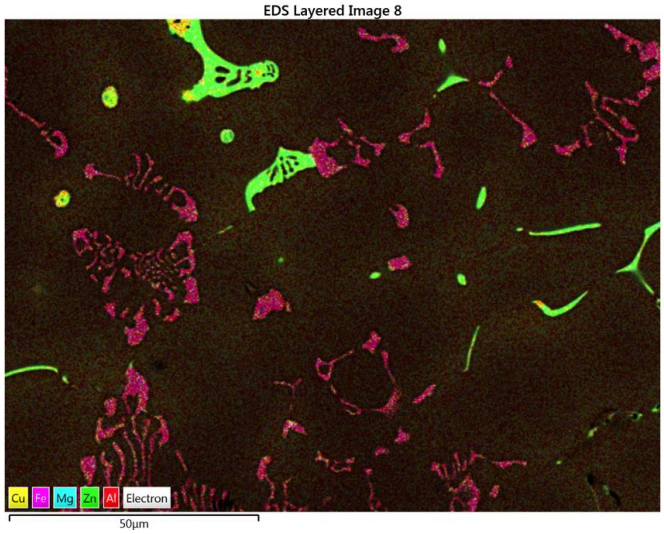

Figure 3.6 Layered EDS scan for alloy7 @ TC1

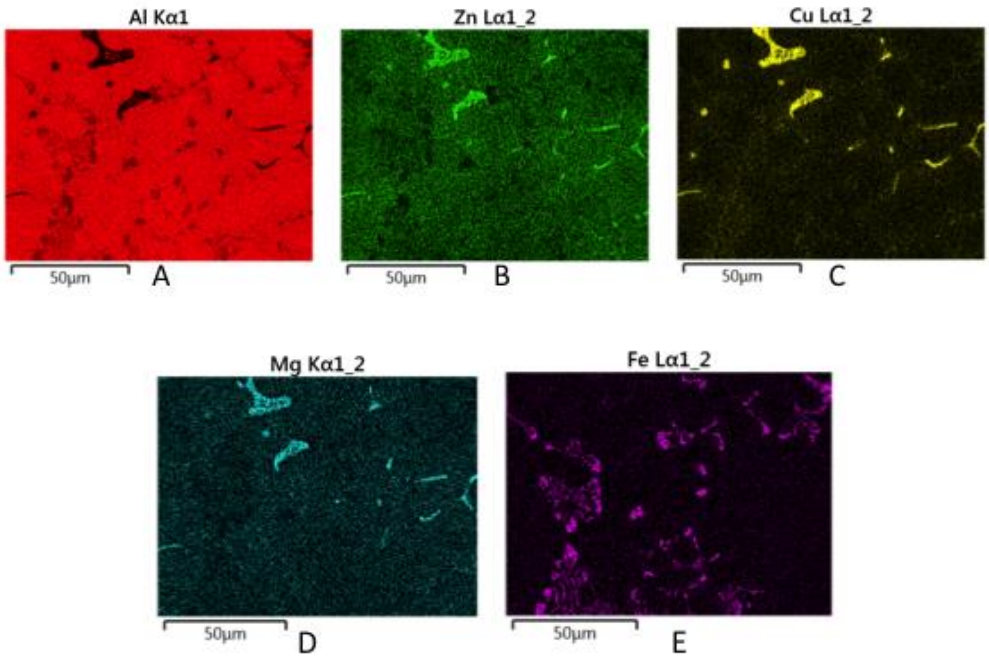

Figure 3.7 (A) - (E) show typical the EDS maps for Al, ZN, Cu, Mg, and Fe

3.8.2 Image analysis

Image J software was used to analyses area and area fraction of the Fe-rich intermetallic phases in the EDS elemental maps, using these steps:

1) The Fe maps were cropped to the edge of the actual mapped area by removing the image borders. A standard image size of 358×270 pixels was selected from the Fe elemental map for analysis.
2) The scale was set by counting the number of pixels in the 50 µm scale marker on the Fe scan. Typically this was 137 pixels, resulting in a final scale for the image processing of approximately 2.75 pixel/µm
3) The image was converted to 8 bit gray scale, resulting in 256 gray values; this default converted the image to a binary image.

4) This image was thresholded to show only the Fe-rich intermetallic phases as black and the remaining material as white (black pixels have a value of 255 and white pixels have a value of 0)
5) Options were selected to measure the number average number, and area percentage of the Fe-rich intermetallic phases in the images, a typically example of which is shown in Figure 3.8 below

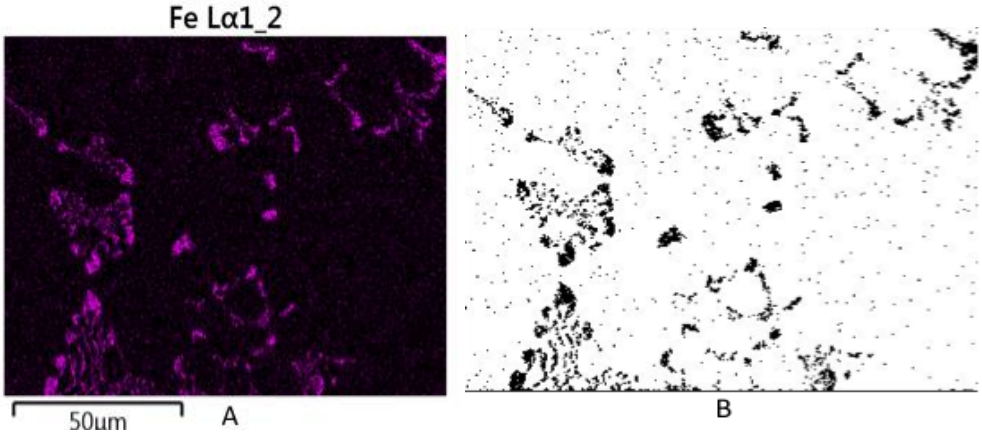

Figure 3.8 (A) Fe elemental EDS map, (B) masked gray scale image of Fe element scan processed by Image J for Alloy 7 @TC 1.

3.8.3 Analysis of microstructure data from Image J

Origin 2017 and Minitab 17 software were used to perform the statistical analysis of the Fe-rich intermetallic phase data obtained using the image J software. The data from the ten SEM images for each thermocouple were aggregated and analyzed together to create a mean area and area fraction estimate for Al-Fe intermetallics from a particular thermocouple location.

3.9 ANOVA and multiple regression analysis

The Analysis of Variance (ANOVA) technique was used to assess the confidence level of the standard deviation of area fraction with the significance level of 0.05%. A sample size of 10 images at each thermocouple location was used for each of the eight samples from each alloy for analysis.

Multiple regression analysis was used to establish a linear relationship between average area fraction of Al-Fe intermetallic phases, cooling rate, and alloy Fe concentration at the eight different thermocouple locations and the experimental alloying elements Zn, Mg, and Cu.

The general form of the multiple regression conducted utilized a linear equation of the form:

$$Y = C + b_1*X_1 + b_2*X_2 + ... + b_n*X_n \qquad \text{Equation 3.1}$$

where, b_1, $b_2 \ldots b_n$ are the regression coefficients, C is the regression constant and X_1,X_2,X_3,X_4 and X_5 are the cooling rate and weight percentage of Zn, Cu, Mg and Fe respectively.

4. Results and Discussion

4.1 Para–equilibrium solidification experiments

Both T_L and T_S were determined from initial para-equilibrium solidification experiments conducted using samples prepared from the precast material of Alloy 4, 7 and 8. As a typical example, the cooling curve and its associated first derivative curve for Alloy 7 is shown in Figure 4.1. The cooling curve (T-t) starts at the pouring temperature of 730 °C and drops rapidly to 632 °C. The nucleation of α-Al begins at this point, which is labeled as the liquidus temperature (T_L), whereby an under-cooling of 1 °C was observed. The respective derivative curve (dT/dt) shows a major inflection point at 632 °C on the cooling curve, which indicates that a major phase change occurred at this point. As the solidification progresses, the temperature drops gradually by releasing a significant amount of heat due to the formation of other secondary eutectic phases. The first derivative curve shows two more inflection points at 470 °C and 450 °C respectively, The inflection point at 450 °C was considered as solidus temperature (T_S). The time between T_L and T_s on the cooling curve is indicated of the solidification time (labeled as t_{sol}), which is 180 s for this case. The average cooling rate (CR) was measured between T_L and T_s, which gave a value of approximately 1 °C/s for this case. The para-equilibrium solidification experiment results for Alloy 4, 7 and 8 are tabulated in the Table 4.1. Considering these results, the holding temperature for the directional solidification experiments should be set above 700 °C to compensate the heat loss during pouring.

Table 4.1 Solidification parameters from para-equilibrium solidification experiments

Alloy	T_L (°C)	T_s (°C)	T_{sol} (s)	CR (°C/s)
4	635	463	175	1.0
7	632	450	180	1.0
8	633	465	150	1.1

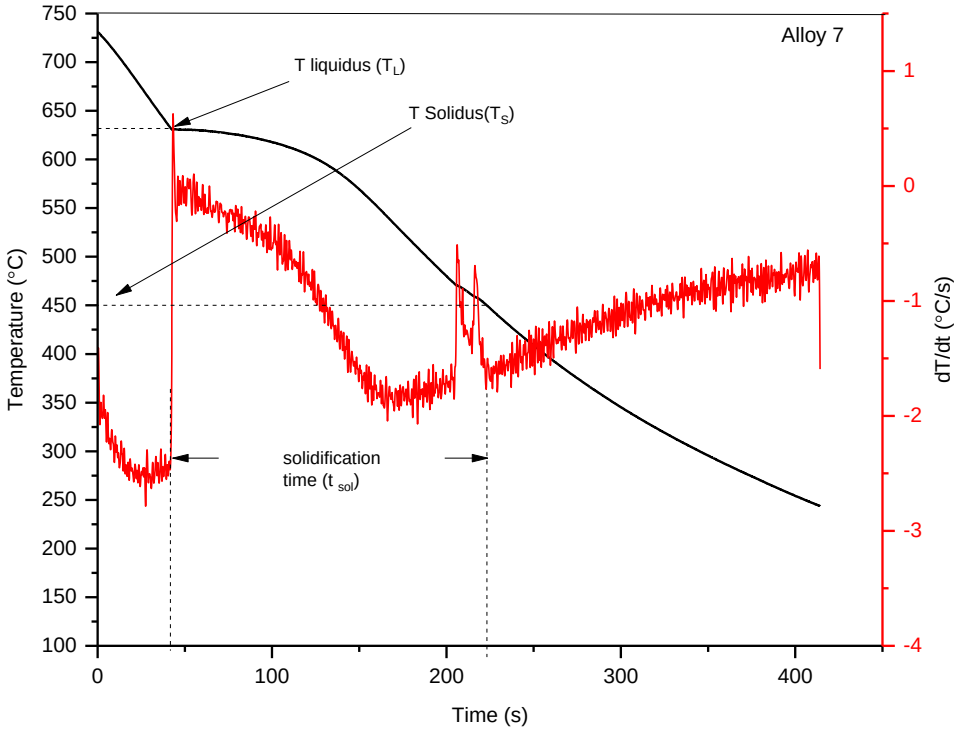

Figure 4.1 Cooling curve and the associated derivative (dT/dt) recorded for the precast Alloy 7 material during the para-equilibrium experiment.

4.2 Directional solidification experiments

The results of the directional solidification experiments for Alloy 1 are presented here as an example of the typical results obtained for each of the nine experimental alloys. The presentation of Alloy 1 results is provided at each TC location (TC1 to TC8) separately, showing the cooling curve, associated set of SEM images of the microstructures and

associated EDS elemental spot analyses of the intermetallics present. The complete set of directional solidification experimental results for the nine experimental alloys are provided in Appendix A.

An average cooling rate was measured for each TC locations. Equation 4.1 shows the formula used to calculate this rate, which is essentially the linearized slope of the cooling curve between the T_L and T_S at each TC location:

$$\textbf{Cooling rate} = \frac{(T_L - T_S)}{(t_L - t_S)} \ ^\circ\text{C/s} \qquad \text{Eqn 4.1}$$

where, T_L and T_S are the liquidus and solidus temperatures respectively, and t_L and t_S are the times at which the liquidus and solidus temperatures were respectively reached on the cooling curve. Because of the sharp peaks associated with the (dT/dt) derivative curve, the onset point for a given peak was considered to be the start time for the average cooling rate measurement.

From the data acquired by the initial para- equilibrium solidification experiments, typical T_L and T_S values for Alloy 4, 7, 8 were determined to be in the range of 630 ± 5 °C and 450 ± 15 °C respectively (as shown in Table 4.1). The average cooling rate attained during those experiments is approximately 1 °C/s. However, at higher average cooling rates expected in the directional solidification experiments, the solidification parameters are expected to differ because of the non-equilibrium nature of the solidification. Figure 4.2 shows the set of cooling curves recorded from each of the eight TCs for Alloy 1. Also included in the text box is the associated average cooling rates, as calculated using Equation 4.1.

The first four TCs (TC1-TC4), which are located close (within 12 mm) to the quench plate (refer Figure 3.1 (B)), revealed relatively rapid solidification as indicated by the "narrow" cooling curves. The average cooling rate associated with TC1, TC2, TC3, and TC4 steadily decreases: from about 40 °C/s at TC1 to 16 °C/s at TC4. The thermal arrest points cannot be accurately measured on these narrow cooling curves because of the relatively high cooling rates.

The remaining four TCs (TC5-TC8) revealed relatively slow solidification, as indicated by a "wide" cooling curves that clearly show the thermal arrest region as a plateau (marked as (TA) on the graph). A more drastic decrease in the average cooling rate is observed at TC5 and TC6, which reveals a rate of 5 °C/s and 2 °C/s respectively. However, TC7 and TC8 show a slightly higher average cooling rates of 6 °C/s and 7 °C/s respectively. The slightly higher rates are consistent with both TCs being mounted near the extreme end of the sample and, thus being influenced by the air cooling due to natural convection above the open top of the sample. This trend is observed to be typical of the set of nine experimental alloys (Appendix A).

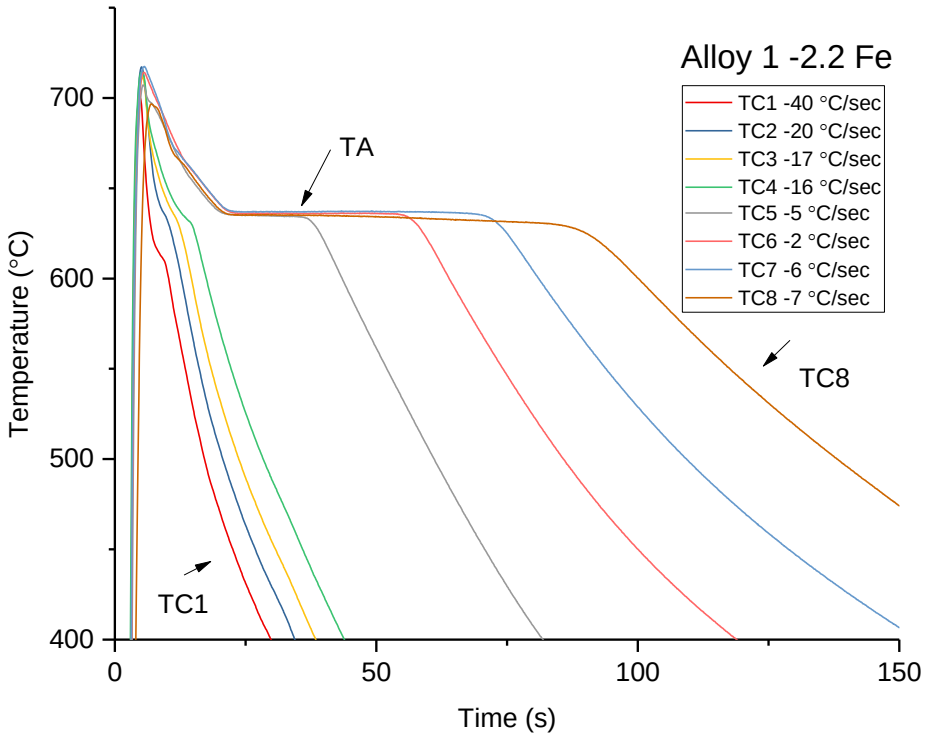

Figure 4.2 Complete set of cooling curves recorded from all eight TC locations (TC1 - TC8) during directional solidification of Alloy 1.

Figure 4.3 and 4.4 (A and B) presents the cooling curve and the associated SEM image of the sample extracted from the TC1 location for Alloy 1 respectively. Figure 4.3 shows a major inflection point on the dT/dt curve at 680 °C, which is the on-set point for T_L and a second major inflection point at 595 °C, which is the on-set point for T_S. The corresponding average cooling rate is 40° C/s and the total solidification time is about 5 s (between T_L and T_S). There were no other major inflection points observed between T_L and T_S, which indicates a suppression of the thermal arrest zone due to a high cooling rate. This is likely an indication of the growth suppression of secondary intermetallics, particularly Al_6Fe intermetallics with high aspect ratios. The latter was confirmed by the SEM images, as shown in Figure 4.4 (A). A dendritic microstructure with fine globular and polyhedral shaped eutectic particles was observed with the size in the order of 1-2

µm. The higher magnification image (Figure 4.4 (B)) show the locations of the five (labeled as 1-5) EDS spot analysis for intermetallic composition.

A typical sum spectrum acquired is shown in Figure 4.5 (A and B) in comparison with a sum spectrum acquired from the matrix. The results of the five EDS spot analyses are listed in the Table 4.2, which clearly indicates that the intermetallics are predominantly Fe containing. All of the particles have Fe concentrations below 22%, which signifies that these intermetallics are metastable phases that form during the primary solidification process and coexists with the α-Al matrix. The Al-Fe intermetallics predominantly form before the eutectic region because of the large amount of Fe in the alloy and high cooling rates.

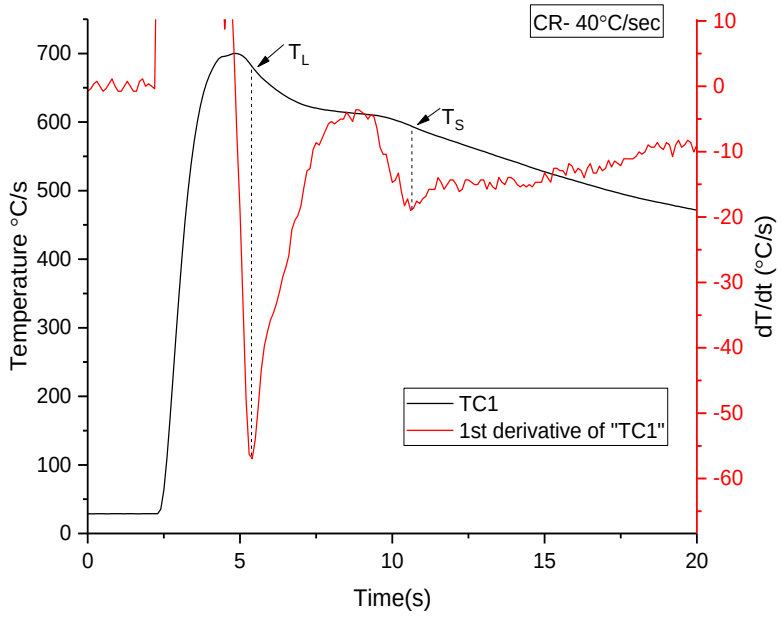

Figure 4.3 Cooling curve and the associated dT/dt curve acquired from the TC1 location during directional solidification of Alloy 1.

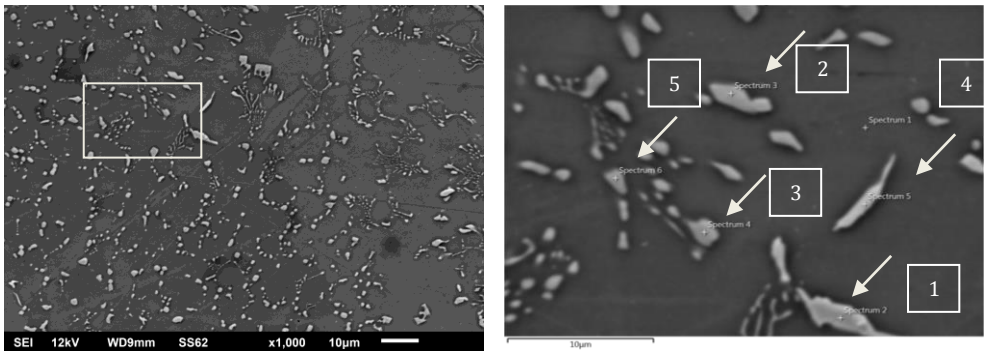

(A) (B)

Figure 4.4 SEM images of the microstructure of the sample extracted from the TC1 location of Alloy 1(A) lower magnification and (B) higher magnification showing locations of EDS spot analysis for intermetallic composition.

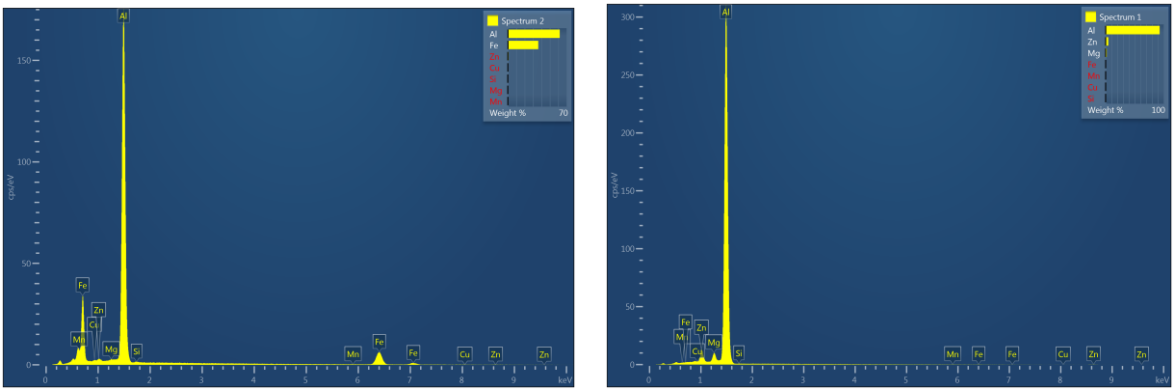

A **B**

Figure 4.5 EDS sum spectra comparison showing a typical spectrum acquired from an intermetallic site (A) relative to one acquired from the matrix (B) of the sample extracted from the TC1 location of the alloy.

Table 4.2 Elemental composition of intermetallics in Figure 4.4 (B) determined by EDS

Phase # as marked in the image	Al at%	Fe at%	Phase
1	77	21	Al_6Fe
2	83	14	Al_6Fe
3	84	14	Al_6Fe
4	80	20	Al_6Fe
5	85	13	Al_6Fe

Figure 4.6 (A, B and C) presents the cooling curve and the associated SEM images, respectively, of the sample extracted from the TC2 location for Alloy 1. T_L and T_S were determined to be 690 °C and 588 °C, respectively , with a corresponding average cooling rate of 20 °C/s and total solidification time of approximately 7s.

Similar to the TC1 location, a dendritic microstructure with fine polyhedral shaped particles having 2-3 µm in size was observed. The higher magnification (Figure 4.6 B) shows the locations of the five (labeled as 1-5) sites selected for EDS spot analysis for intermetallic composition. The results of the five EDS spot analyses are listed in the Table 4.3, which clearly indicates that the intermetallics are predominantly Fe containing. All of the particles have Fe concentrations below 10% indicating that they are consistent with Al_6Fe.

Figure 4.7 (A, B and C) presents the cooling curve and the associated SEM images, respectively of the sample extracted from the TC3 location for Alloy 1. T_L and T_S were determined to be 696 °C and 585 °C, respectively, with an average cooling rate of 17 °C/s and the total solidification time of approximately 9 s.

Figure 4.7 (B, C) shows a dendritic microstructure with some sharp edged polyhedral shaped intermetallics 2-3 µm in size. The higher magnification image (Figure 4.7 B) shows the locations of the five (labeled as 1-5) sites selected for EDS spot analysis for intermetallic composition. The results of the five EDS spot analyses are listed in the Table 4.3, which clearly indicates that the intermetallics are predominantly Fe containing. All of the particles have Fe concentrations below 14%, which are consistent with Al_6Fe.

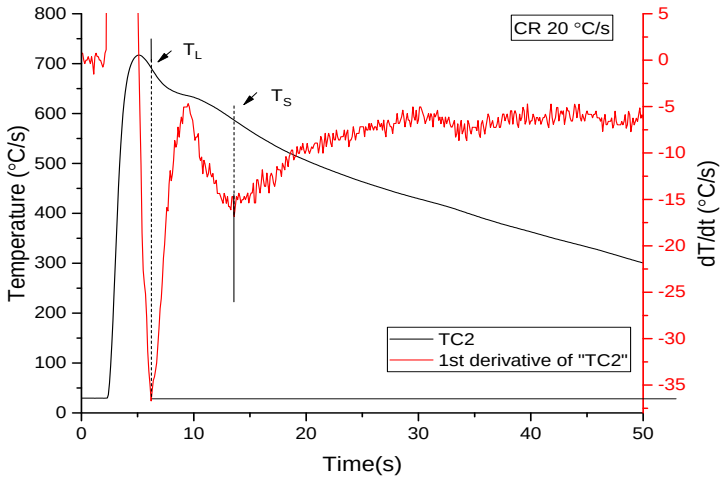

(A)

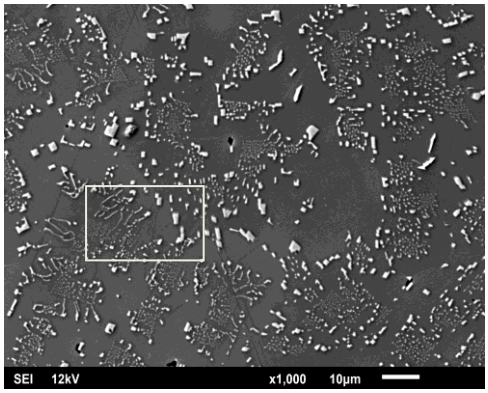

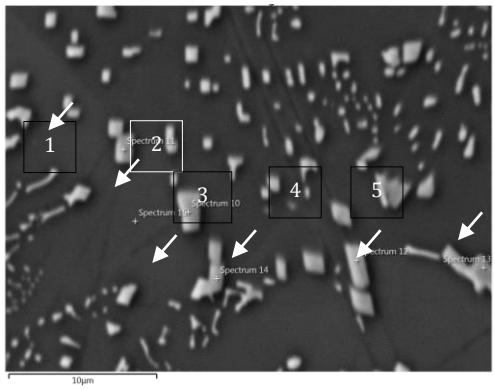

(B) (C)

Figure 4.6 (A) Cooling curve and the associated dT/dt curve acquired from the TC2 location during directional solidification of Alloy 1.
SEM images of the microstructure of the sample extracted from the TC2 location of Alloy 1 lower magnification (B) and (C) higher magnification showing locations of the EDS spot analyses for intermetallic composition.

Table 4.3 Elemental composition of intermetallics in Figure 4.6 (B) determined by EDS

Phase # as marked in the image	Al	Fe	phase
	at%	at%	
1	88	8	Al_6Fe
2	86	10	Al_6Fe
3	87	9	Al_6Fe
4	85	10	Al_6Fe
5	85	11	Al_6Fe

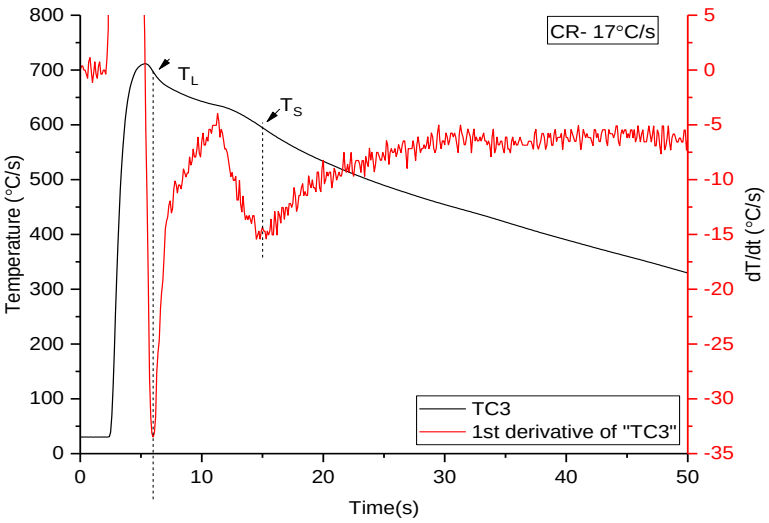

(A)

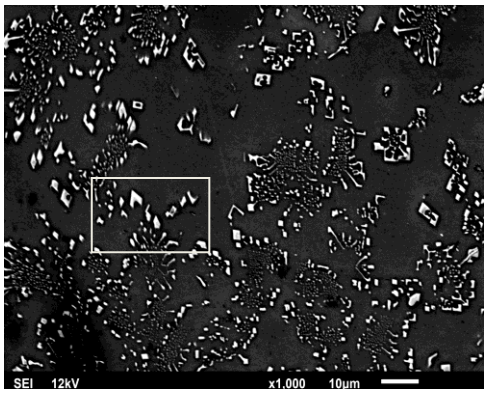

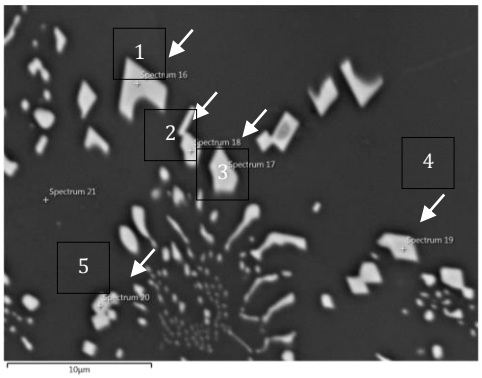

(B) (C)

Figure 4.7 (A) Cooling curve and the associated dT/dt curve acquired from the TC3 location during directional solidification of Alloy 1.
SEM images of the microstructure of the sample extracted from the TC2 location of Alloy 1 lower magnification (B) and (C) higher magnification showing locations of the EDS spot analyses for intermetallic composition.

Table 4.4 Elemental composition of intermetallics in Figure 4.7 (B) determined by EDS

Phase # as marked in the image	Al at%	Fe at%	phase
1	83	14	Al_6Fe
2	84	13	Al_6Fe
3	84	14	Al_6Fe
4	84	14	Al_6Fe
5	85	11	Al_6Fe

Figure 4.8 (A, B and C) presents the cooling curve and the associated SEM images, respectively of the sample extracted from the TC4 location for Alloy 1. T_L and T_S were determined to be 702 °C and 610 °C, respectively, with an average cooling rate of 16 °C/s and total solidification time was approximately 10 s.

Figure 4.8 (B, C) shows the precipitation of sharp edged needle shaped intermetallics combined with a star shaped bulky intermetallic approximately 15-20 µm in size. The higher magnification image (Figure 4.8 C) shows the locations of the five (labeled as 1-5) sites selected for EDS spot analysis for intermetallic composition. The results of the five EDS spot analyses are listed in the Table 4.4, which clearly indicates that the intermetallics are predominantly Fe containing. All of the particles have Fe concentrations above 23 %, which are consistent with Al_3Fe.

A major transition in the morphology of the Fe containing intermetallics was observed at TC4, with an average cooling rate of 16 °C/s.

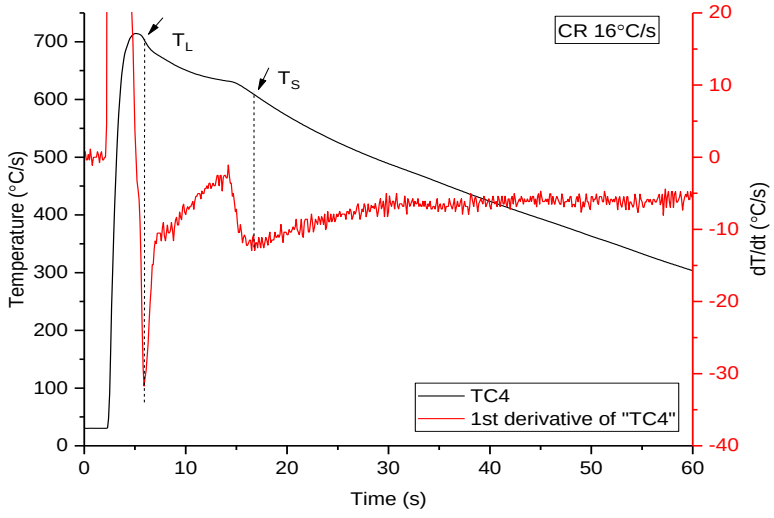

(A)

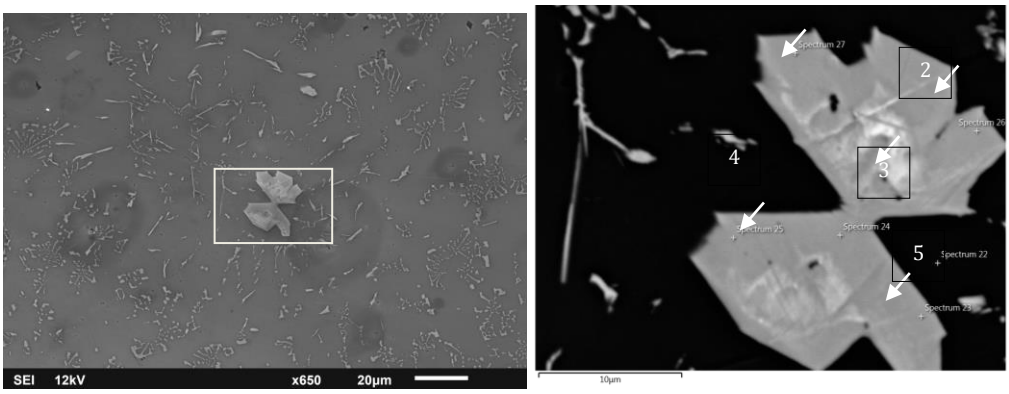

(B) (C)

Figure 4.8 (A) Cooling curve and the associated dT/dt curve acquired from the TC4 location during directional solidification of Alloy 1.
SEM images of the microstructure of the sample extracted from the TC2 location of Alloy 1 lower magnification (B) and (C) higher magnification showing locations of EDS spot analyses for intermetallic composition.

Table 4.5 Elemental composition of intermetallics in Figure 4.8 (B) determined by EDS

Phase # as marked in the image	Al	Fe	
	at%	at%	phase
1	78	22	Al_3Fe
2	77	23	Al_3Fe
3	77	23	Al_3Fe
4	78	22	Al_3Fe
5	77	24	Al_3Fe

Collectively (TC5-TC8) shows similar behavior in terms of precipitation of secondary intermetallics. A plateau region was observed in all the cooling curves, which indicates the existence of a thermal arrest zone (TA) and, correspondingly, the evolution of secondary eutectic phases. A major inflection point between T_L and T_S is taken as the eutectic temperature (T_E).

Figure 4.9 to 4.12 presents the cooling curves and the associated SEM images, respectively, of the sample extracted from the TC5-TC8 locations for Alloy 1. Table 4.6 shows the results obtained from the cooling curves.

Table 4.6 Solidification parameters obtained from cooling curves of TC5-TC8 for Alloy1.

TC	T_L (°C)	T_S (°C)	T_E (°C)	t_{sol} (s)	CR °C/s
5	695	630	680	37	5
6	702	640	690	55	2
7	690	615	655	67	6
8	675	600	650	90	7

From the SEM images of all the TC locations (TC5-TC8), it was observed that the intermetallics have a relatively high aspect ratio with sharp edges. A range of morphologies were observed in these images including needle-likes, blocky clusters and star-like.

Tables 4.7 to 4.10 show the results of the five EDS spot analysis conducted on the sites identified on the SEM images shown in Figure 4.9 (B) to 4.12 (B), which clearly indicates that the intermetallics are Fe containing with the concentration above 23%. These, are the primary Al-Fe intermetallics that form during solidification process due to low cooling rates. From the results (Tables 4.7 to 4.10) it is evident that the intermetallics observed at high cooling rates (above about 16 °C/s) are metastable and all of the intermetallics analyzed are consistent with Al_6Fe with an aspect ratio close to unity (spherical particles). At low cooling rates (below about 16 °C) the intermetallics observed are likely having Al_3Fe intermetallics with a high aspect ratio.

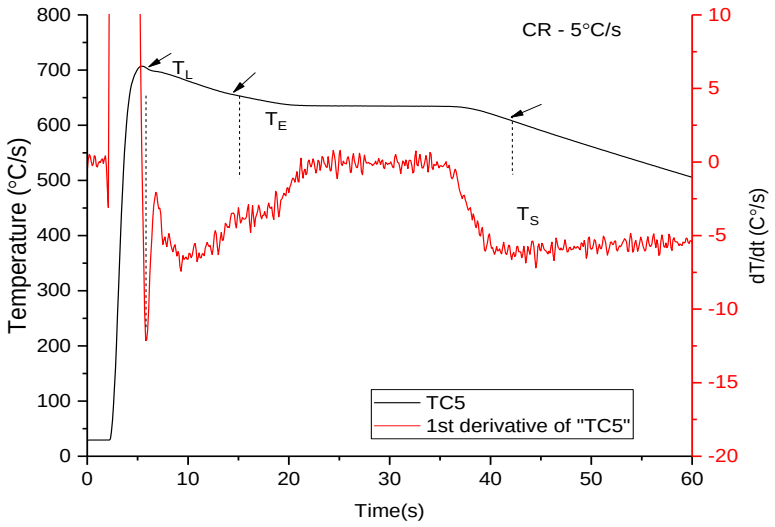

(A)

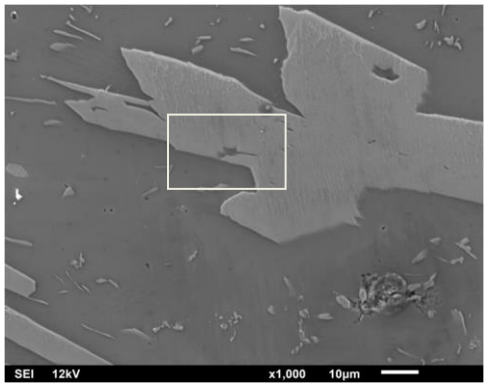

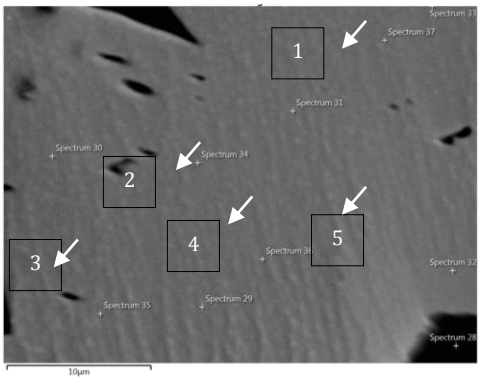

(B) (C)

Figure 4.9 (A) Cooling curve and the associated dT/dt curve acquired from the TC5 location during directional solidification of Alloy 1
SEM images of the microstructure of the sample extracted from the TC5 location of Alloy 1: lower magnification (B) and (C) higher magnification showing locations of the EDS spot analyses for intermetallic composition.

Table 4.7 Elemental composition of intermetallics in Figure 4.9 (B) determined by EDS

Phase # as marked in the image	Al at%	Fe at%	phase
1	76	23	Al_3Fe
2	77	23	Al_3Fe
3	76	23	Al_3Fe
4	76	24	Al_3Fe
5	76	24	Al_3Fe

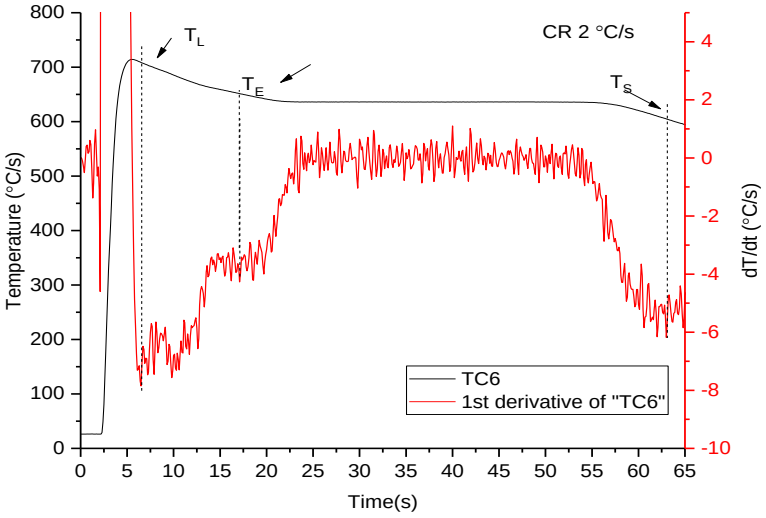

(A)

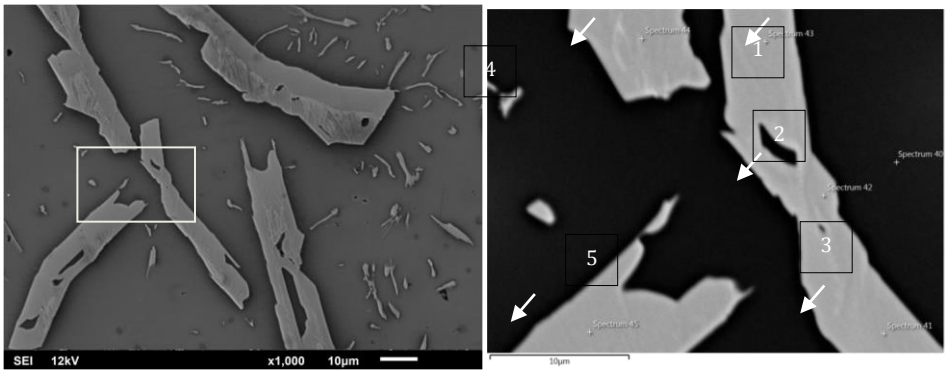

(B) (C)

Figure 4.10 (A) Cooling curve and the associated dT/dt curve acquired from the TC6 location during directional solidification of Alloy 1
SEM images of the microstructure of the sample extracted from the TC6 location of Alloy 1 lower magnification (B) and (C) higher magnification showing locations of EDS spot analysis for intermetallic composition.

Table 4.8 Elemental composition of intermetallics in Figure 4.10 (B) determined by EDS spot analysis

Phase # as marked in the image	Al at%	Fe at%	phase
1	77	23	Al_3Fe
2	76	23	Al_3Fe
3	76	24	Al_3Fe
4	76	24	Al_3Fe
5	77	23	Al_3Fe

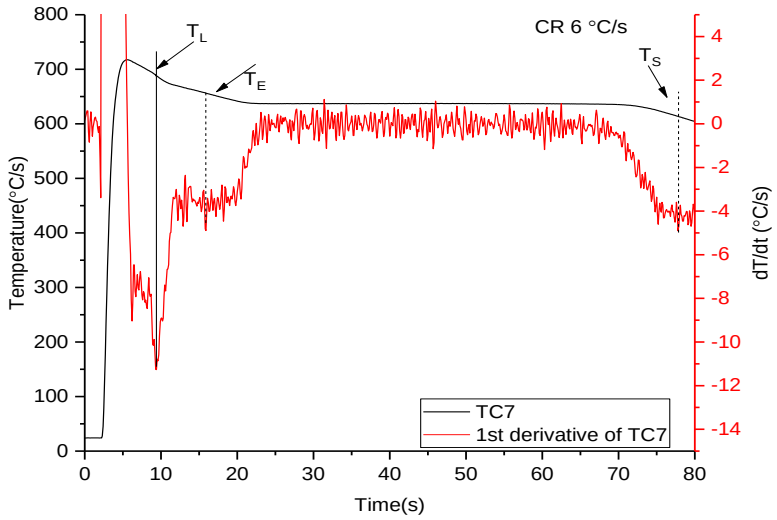

(A)

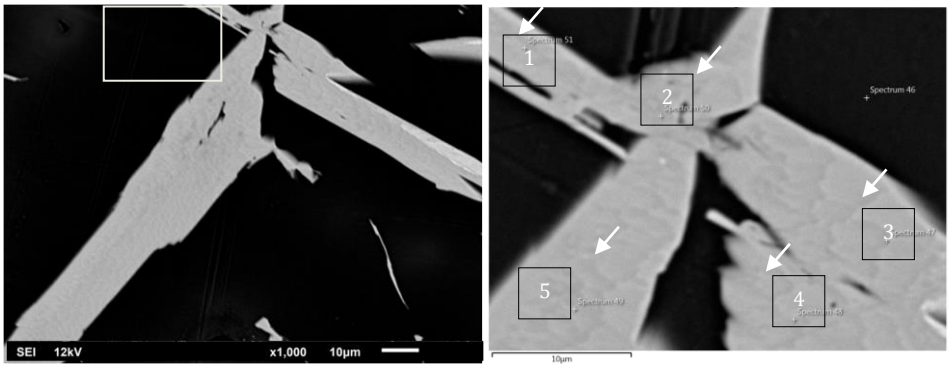

(B) (C)

Figure 4.11 (A) Cooling curve and the associated dT/dt curve acquired from the TC7 location during directional solidification of Alloy 1
SEM images of the microstructure of the sample extracted from the TC7 location of Alloy 1: lower magnification (B) and (C) higher magnification showing locations of the EDS spot analyses for intermetallic composition.

Table 4.9 Elemental composition of intermetallics in Figure 4.11 (B) determined by EDS

Phase # as marked in the image	Al at%	Fe at%	phase
1	76	23	Al_3Fe
2	76	23	Al_3Fe
3	76	23	Al_3Fe
4	77	23	Al_3Fe
5	76	23	$FeAl_3$

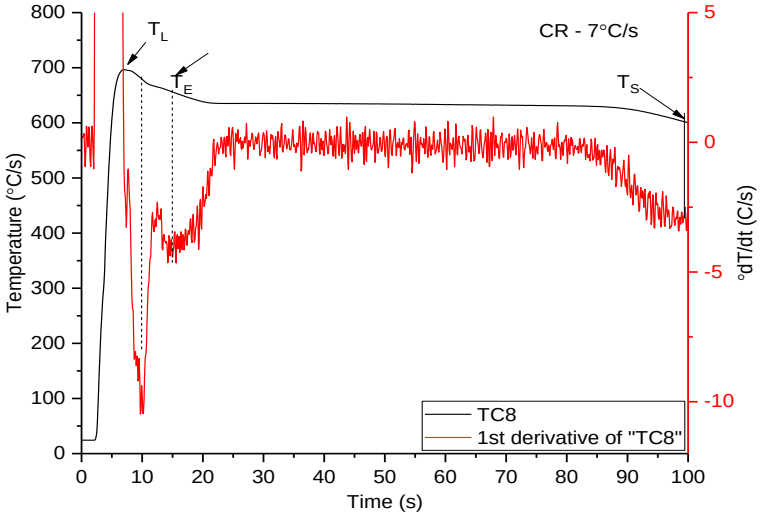

(A)

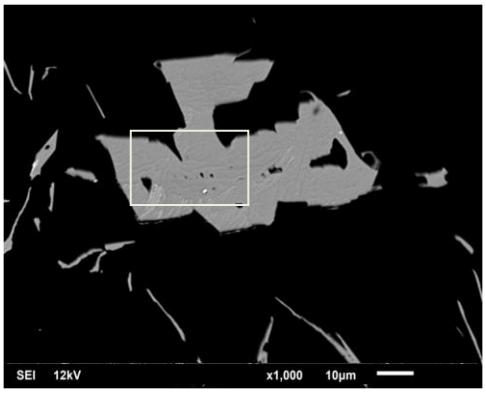

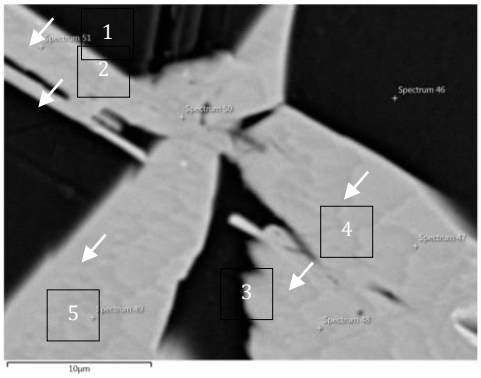

(B) (C)

Figure 4.12 (A) Cooling curve and the associated dT/dt curve acquired from the TC8 location during directional solidification of Alloy 1
SEM images of the microstructure of the sample extracted from the TC8 location of Alloy 1: lower magnification (B) and (C) higher magnification showing locations of the EDS spot analyses for intermetallic composition.

Table 4.10 Elemental composition of intermetallics in Figure 4.12 (B) determined by EDS

Phase # as marked in the image	Al at%	Fe at%	phase
1	76	23	Al_3Fe
2	76	24	Al_3Fe
3	77	23	Al_3Fe
4	76	23	Al_3Fe
5	76	23	Al_3Fe

4.3 Statistical analysis of the Al-Fe intermetallics

Ten SEM images were taken at a consistent magnification from each TC location during the directional solidification experiments conducted using each of the nine experimental alloys. Associated EDS spot analyses were performed on the intermetallics present to determine the type. The ten SEM images were further analyzed by image analysis to determine the area fraction associated with the set of ten images. These parameters provide useful insight into the effect of cooling rate on microstructure evolution during non-equilibrium solidification. The statistical analysis was performed for all the nine experimental alloys (Appendix B), the results discussed below pertain to only Alloy 1.

4.3.1 Type (Fe content)

Figure 4.13 shows the Fe content (at%) in the intermetallics as a function of average cooling rate (TC location) for Alloy 1. The error bars represents the 95% confidence interval from the data acquired from five spectra selected for analysis from each of the ten SEM images taken at each of the eight TC locations (average cooing rates). Lower Fe contents are detected in the intermetallics formed at the higher cooling rates associated with 40 °C/s (TC1), 20 °C/s (TC2), 17 °C/s (TC3). A considerable increase in the Fe content occurs when the average cooling rate drop below that associated with TC4 (16 °C/s), the transition presumably from Al_6Fe (Fe < 22%) to Al_3Fe (Fe >22%) occurs at a critical average cooling rate of 16°C/s (TC4).

It is evident from Tables 4.2 - 4.10 that the intermetallics formed at average cooling rates associated with TC4 to TC5 are (based on the Fe:Al content (at%) ratio) to be predominantly Al_3Fe. The Al_3Fe phase is the first thermodynamically stable phase that forms in the Al-Fe phase diagram as the Fe content increases. There is significant

evidence in the literature that shows there is an evolution of metastable phase formation involved during non-equilibrium cooling of Al-Fe alloys [14, 15, 17, 18, 20].

For example, Al_6Fe is one of the metastable phase that has been reported to form during solidification at relatively high cooling rates in Al-Fe alloys with less than 22 at% Fe [14, 17]. As shown in table 4.2 to 4.4 most of the identified intermetallics contain less than 22 at% Fe and greater than 80 at% Al. Therefore, the intermetallics formed at higher cooling rates (> 16 °C/s) likely are metastable [14, 17, 21].

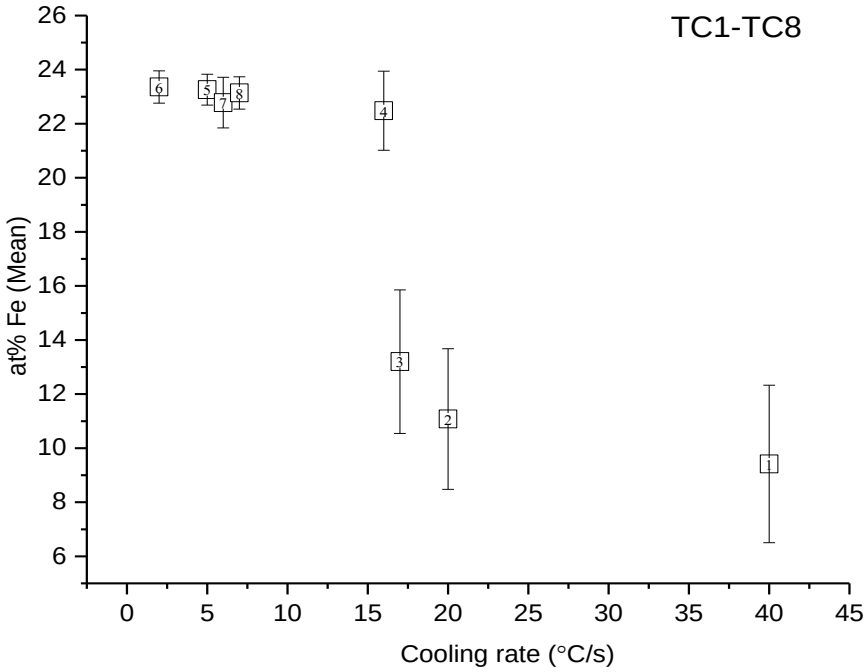

Figure 4.13 Fe content (at%) of intermetallic as a function of the average cooling rate for Alloy 1

Figure 4.14 a collective graph of nine alloys shows that there is a trend that exists with the variation Fe content (at%) in the intermetallics as a function of average cooling rate (TC location) for Alloy 1-9. The error bars represents the 95% confidence interval from the data acquired from five spectra selected for analysis from each of the ten SEM images

taken at each of the eight TC locations (average cooing rates). Although, the transition from Al_3Fe to Al_6Fe occur at a critical temperature, it will be difficult to determine that which depends on the individual alloy solidification conditions. All the nine alloys show a transition over a range of temperatures that depends upon the individual TC cooling rates. Alloy 1, Alloy 4, Alloy 7, and alloy 8 reveals a transition at the cooling rate approximately 15 °C., Alloy 3, Alloy 5, Alloy 6, and Alloy 9 reveals a transition approximately at 10 °C.

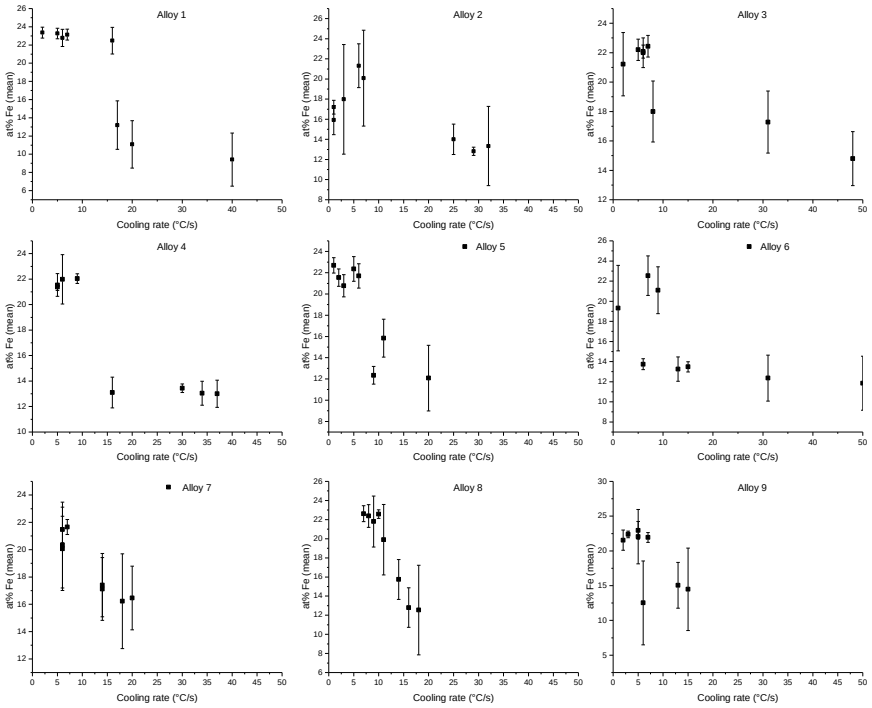

Figure 4.14 Collective graphs of Fe content (at%) of intermetallic as a function of the average cooling rate for Alloy 1-9

4.3.2 Area fraction distribution

Figures 4.15 to 4.22 shows a set of histograms of the area fraction distribution of the Al-Fe intermetallics determined from set of ten images acquired from each of the eight TC locations respectively, of Alloy 1. Collectively, the area fraction histograms show that the distribution peak shift towards smaller sizes, which are large in number (frequency) and indicates trend towards bimodal distribution of small and large sized intermetallics. This shows that the resultant statistics is biased, especially towards large sized intermetallics.

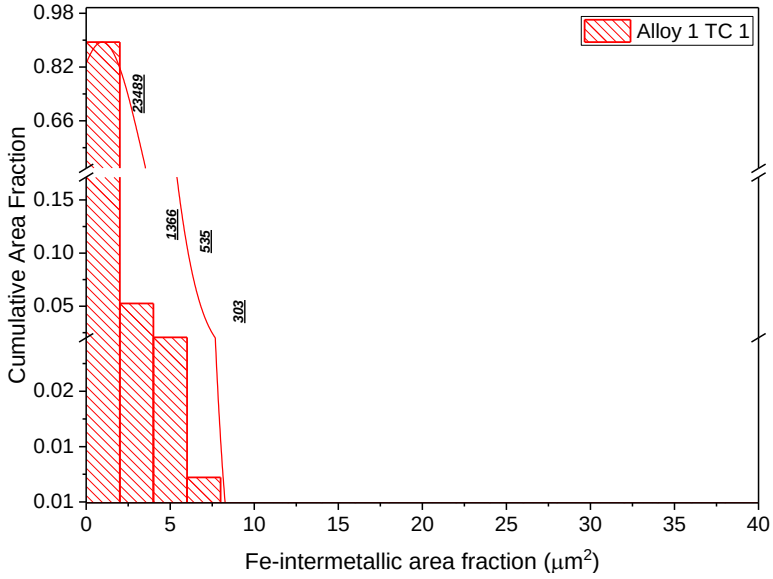

Figure 4.15 Distribution plot of the area fraction of the intermetallics acquired from the set of ten images taken at the TC1 location in Alloy 1

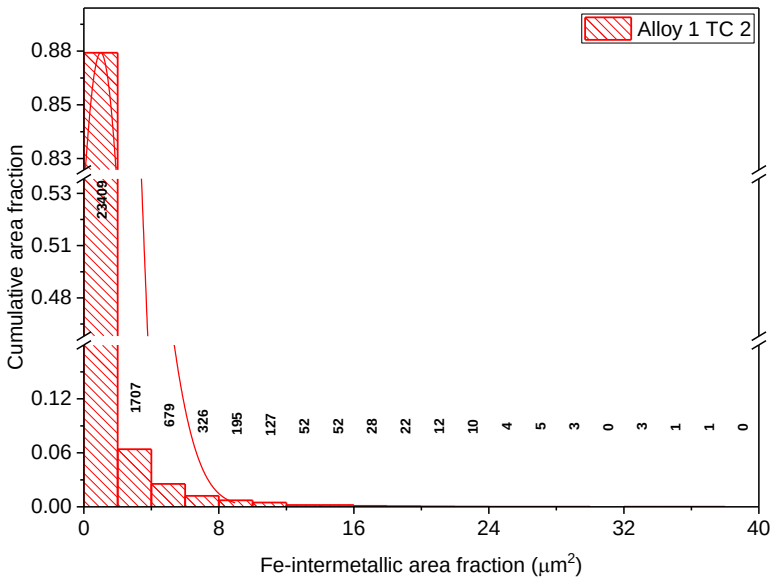

Figure 4.16 Distribution plot of the area fraction of the intermetallics acquired from the set of ten images taken at the TC2 location in Alloy 1

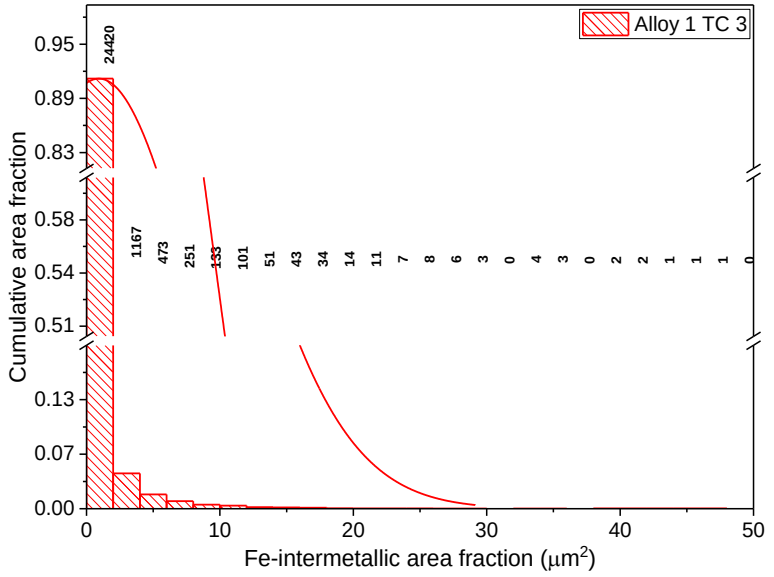

Figure 4.17 Distribution plot of the area fraction of the intermetallics acquired from the set of ten images taken at the TC3 location in Alloy 1

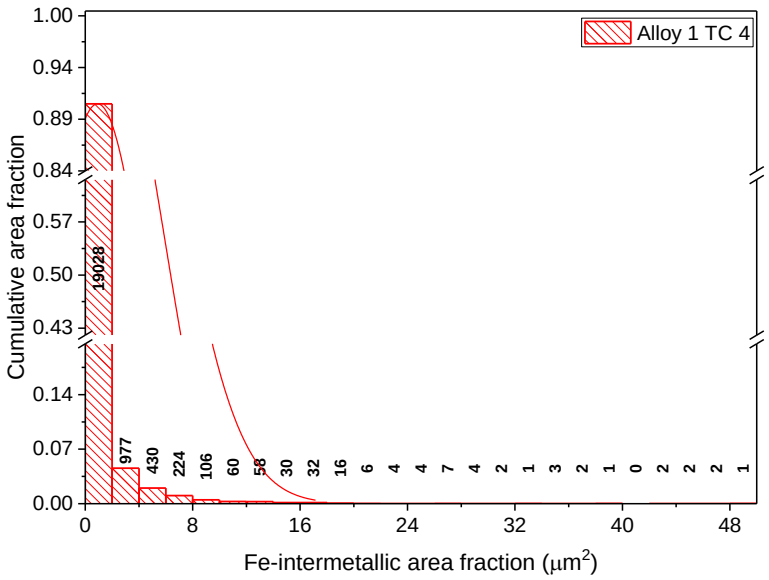

Figure 4.18 Distribution plot of the area fraction of the intermetallics acquired from the set of ten images taken at the TC4 location in Alloy 1

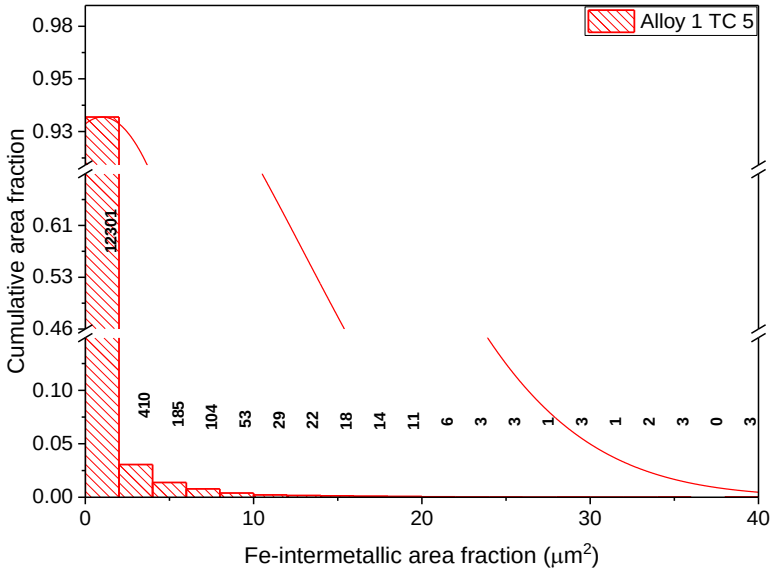

Figure 4.19 Distribution plot of the area fraction of the intermetallics acquired from the set of ten images taken at the TC5 location in Alloy 1

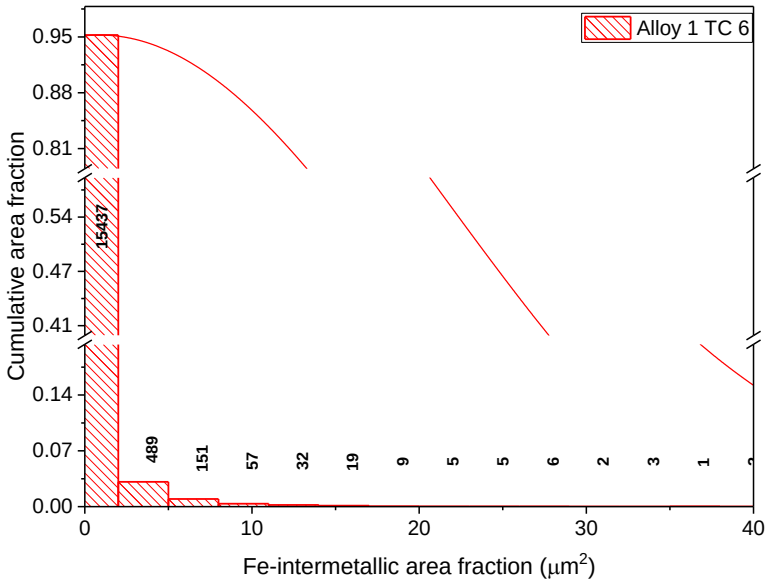

Figure 4.20 Distribution plot of the area fraction of the intermetallics acquired from the set of ten images taken at the TC6 location in Alloy 1

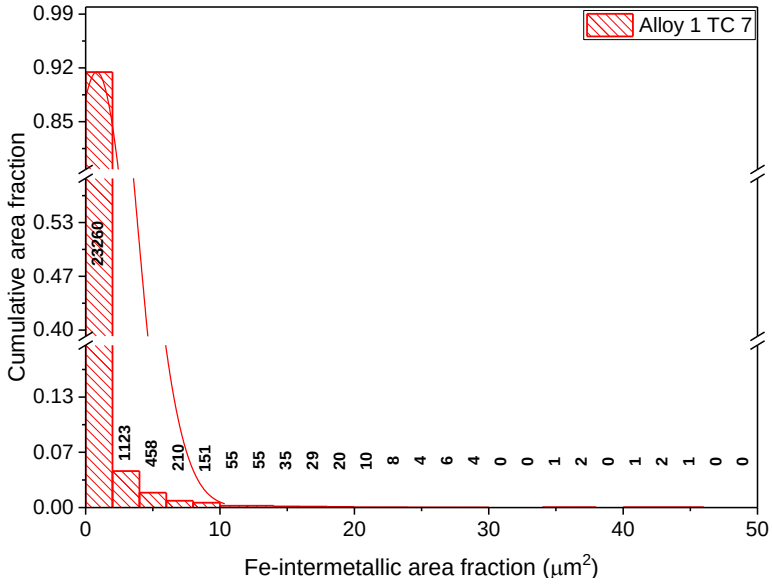

Figure 4.21 Distribution plot of the area fraction of the intermetallics acquired from the set of ten images taken at the TC7 location in Alloy 1

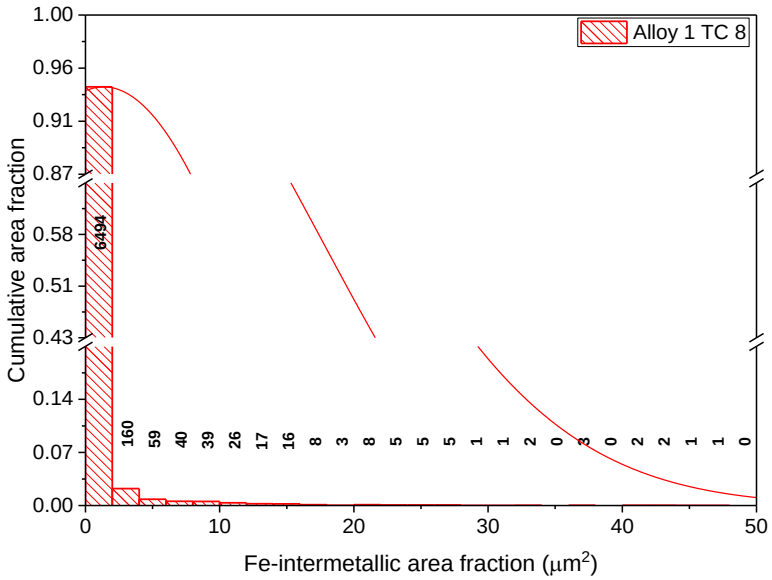

Figure 4.22 Distribution plot of the area fraction of the intermetallics acquired from the set of ten images taken at the TC8 location in Alloy 1

4.3.3 Area fraction

Figure 4.23 shows the area fraction (%) of the Al-Fe intermetallics as a function of the average cooling rate (TC location) for Alloy 1. TC5, TC6, and TC8 with a relatively low average cooling rate, coincides with a lower area fraction of Al-Fe intermetallics, this indicates that the Al-Fe intermetallics are bigger in size and less in number within a specific area of interest.

Again, the reason for the bigger size at a lower average cooling rate is the increased time available for the Al-Fe intermetallics to grow during non-equilibrium solidification. A higher area fraction associated with the TC1, TC2, TC3, TC4, and TC7 locations indicates that a large number of finer Al-Fe intermetallics cover a larger area of the frame.

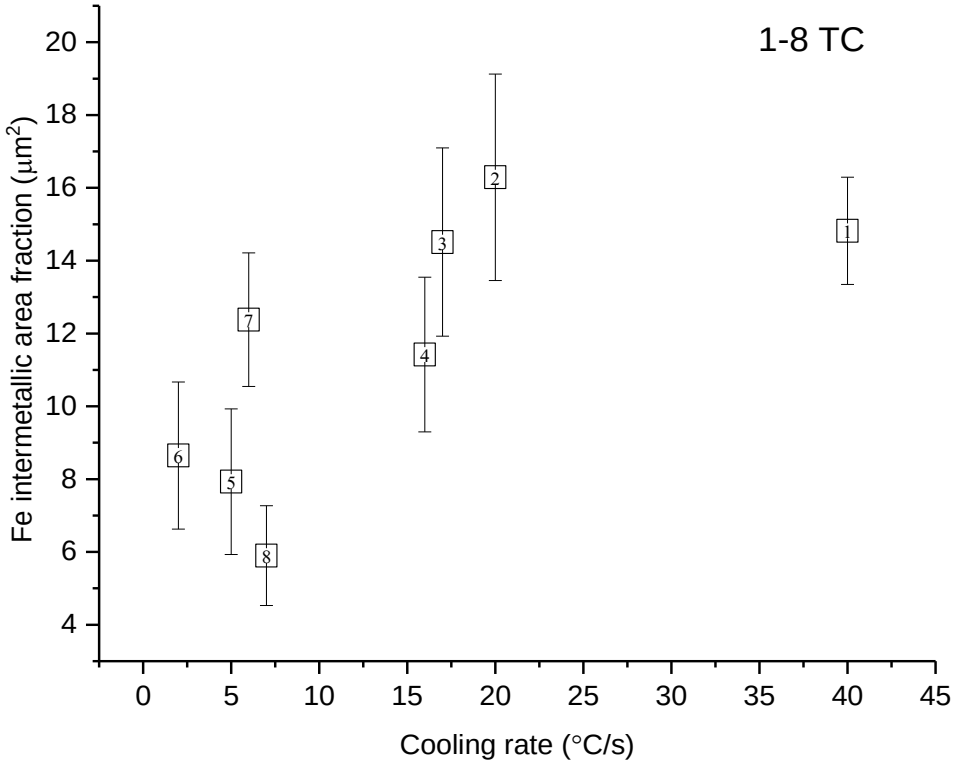

Figure 4.23 Area fractions of Al-Fe intermetallics plotted as a function of the average cooling rate for alloy 1

The trend looks like there is an increase in area fraction as the average cooling rate increases. However, the area fraction at TC locations with a high average cooling rate varies from 11 to 17 μm^2, whereas it varies 6 to 9 μm^2 at TC locations with a low average cooling rate. The difference is not very significant compared to the relatively large area fraction occupied by the individual Al-Fe intermetallics at different thermocouple locations. It is possible that some of the larger size particles exist at low cooling rates were not captured during the imaging because of the limitation in sampling number. The trend for the dependence of area fraction on the average cooling rate can be more quantitatively determined, provided there are a significant number of fields to generate a

representative sampling of the intermetallic population at the higher average cooling rates.

The increase in area fraction at higher cooling rates can be attributed to the consequential effect of transition in particle chemistry from low to high cooling rates as shown in Figure 4.13. The transition from Al_3Fe to Al_6Fe yields intermetallics with different densities which in turn forms a trend in area fraction distribution in a manner consistent with obeying the global Fe mass balance in the alloy.

4.4 Global correlation assessments

Sections 4.2 and 4.3 present and discuss the directional solidification experimental results obtained for Alloy 1 in terms of the effect that of cooling rate has on the type, morphology and area fraction of the Al-Fe intermetallics. A similar analysis was performed on the remaining eight experimental alloys (refer Table 3.1) the results of which are provided in Appendix A. A multiple regression analysis method available in the Minitab's software was applied to the entire data set to determine the global effect of the cooling rate and alloy composition on the type, morphology, and area fraction of the Al-Fe intermetallics.

The cooling rate and alloy composition (Zn, Mg, Cu and, Fe content) were used as continuous variables and the area fraction was used as a response variable. The resulting system of equations generated by the Minitab software describes the relationship between the input variable and how they affected the outcome of the experiments. The model is helpful in predicting the Fe content (type) and area fraction of the Al-Fe intermetallics in the alloy based on the composition and cooling rate.

4.5 Intermetallic Fe content (type) correlations

Figures 4.24 to 4.28 illustrate the effect of cooling rate and alloy composition (Fe, Cu, Mg and Zn content) on the Fe-content (type) of the Al-Fe intermetallics formed. Figure 4.24 show that the Fe content in the intermetallic has a positive correlation with the cooling rate. As discussed in Section 4.3.1, at low cooling rates, stable Al_3Fe intermetallics with relatively high Fe content tends to form since sufficient time is available for growth. However, at higher cooling rates, due to more non-equilibrium solidification conditions, metastable phases low in Fe content tend to form.

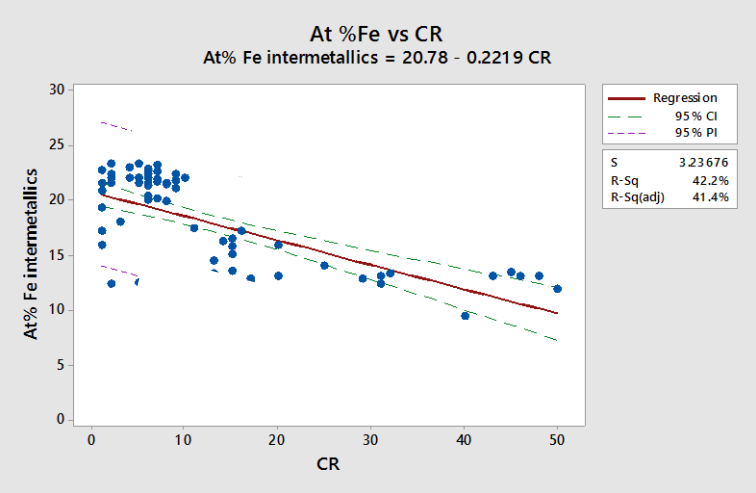

Figure 4.24 Regression plot showing the effect of cooling rate on the Fe content of the Al-Fe intermetallics formed.

In contrast, the alloy composition (Fe, Cu, Mg and Zn content) do not show any significant influence on the Fe content of the Al-Fe intermetallics formed, as shown in Figures 4.25 and 4.28 respectively.

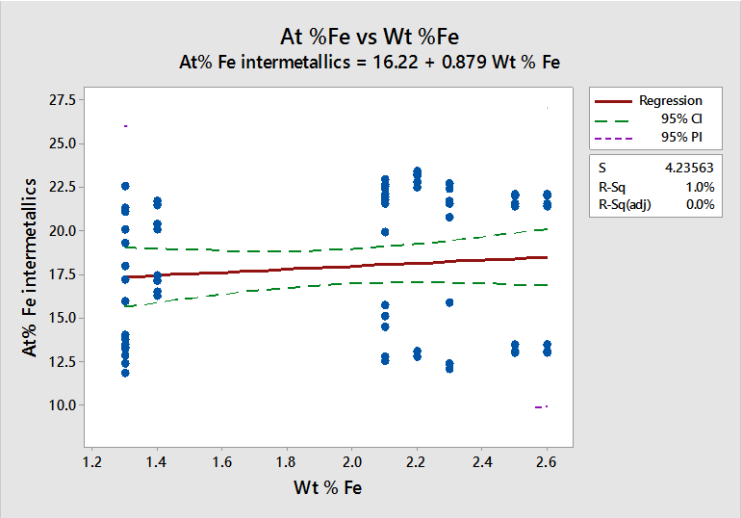

Figure 4.25 Regression plot showing the effect of alloy Fe content on the Fe content of the Al-Fe intermetallics formed.

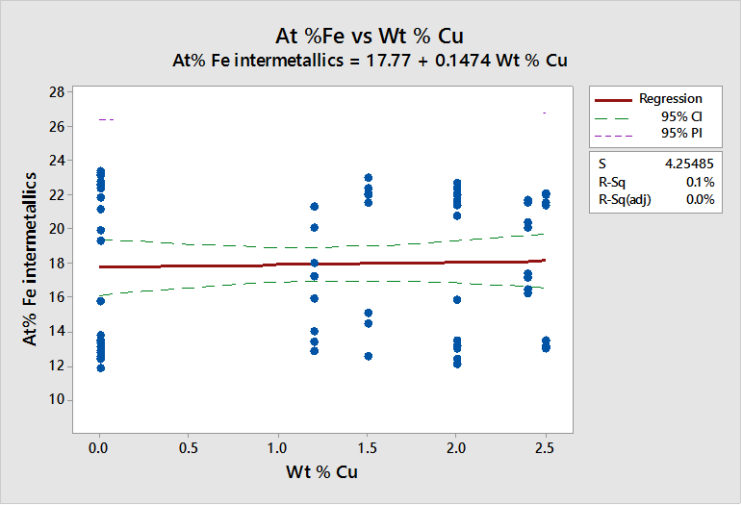

Figure 4.26 Regression plot showing the effect of alloy Cu content on the Fe content of the Al-Fe intermetallics formed.

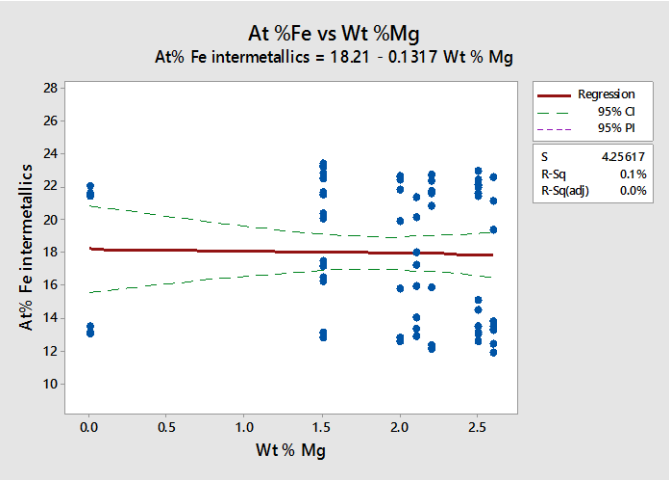

Figure 4.27 Regression plot showing the effect of alloy Mg content on the Fe content of the Al-Fe intermetallics formed.

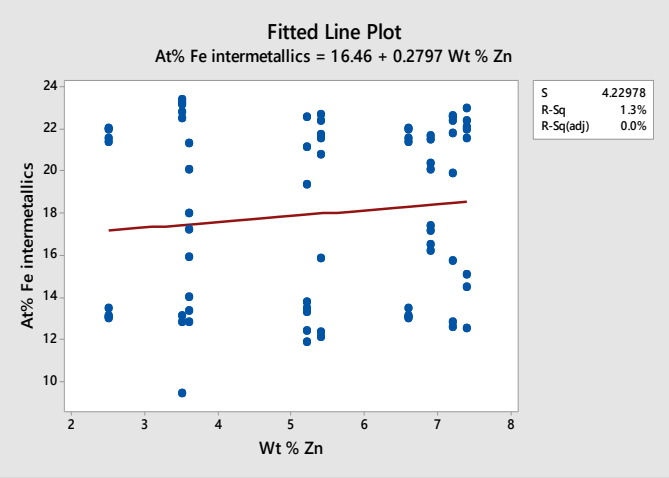

Figure 4.28 Regression plot showing the effect of alloy Zn content on the Fe content of the Al-Fe intermetallics formed.

The overall equation developed from this regression model that considers the effect of cooling rate and alloy Fe, Mg, Cu, and Zn content on the Fe content of the Al-Fe intermetallics formed is given as:

$$\textbf{at\% Fe intermetallics} = 23.06 - 0.2392\,CR - 1.099\,\textbf{wt \% Mg} \quad \text{Eqn 4.2}$$

Table 4.11 P values corresponding to regression Equation 4.2

Variables	CR	wt% Fe	wt% Mg	wt% Cu	wt% Zn
P-values	0	0.39	0.84	0.77	0.31

Removing the statistically insignificant factors with P-values greater than 0.1 (see Table 4.11) gives the following simplified correlation equation:

$$\textbf{at\% Fe intermetallics} = 23.06 - 0.2392\,CR \quad \text{Eqn 4.3}$$

4.6 Intermetallic area fraction correlations

Figures 4.29 to 4.33 illustrate the effect of cooling rate and, alloy composition (Fe, Mg, Cu, and Zn content) on the area fraction of the Al-Fe intermetallics formed. From Figure 4.29, it is evident that the cooling rate has a moderate influence on the area fraction as indicated by an R square value of 22%. As discussed in the Section 4.3.3, this apparent correlation may not be the exact representation of the dependence because of the limitation in sampling number for the statistical analysis conducted.

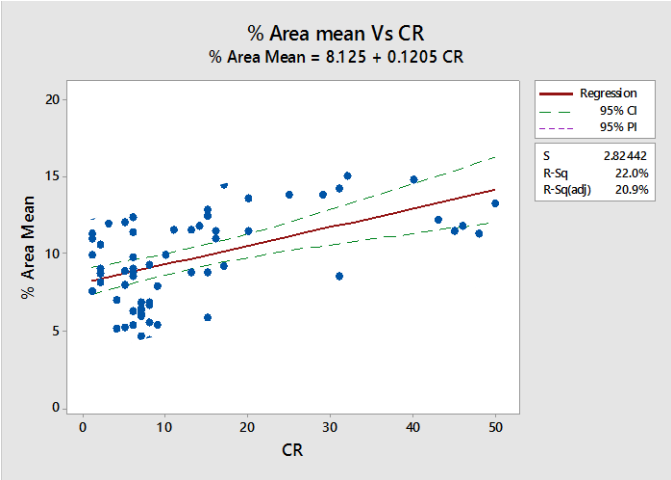

Figure 4.29 Regression plot showing the effect of cooling rate on the area fraction of the Al-Fe intermetallics formed.

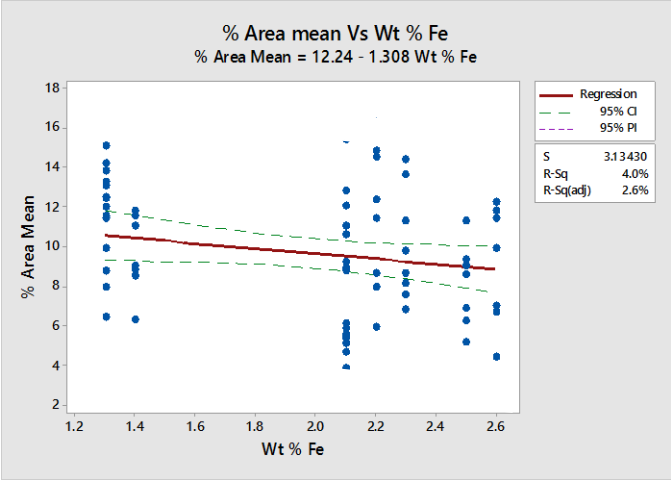

Figure 4.30 Regression plot showing the effect of alloy Fe content on the area fraction of the Al-Fe intermetallics formed.

The Fe content of the alloy shows a minor negative correlation with area fraction, whereas the three other alloying elements show no correlation as shown in Figures 4.31 to 4.33

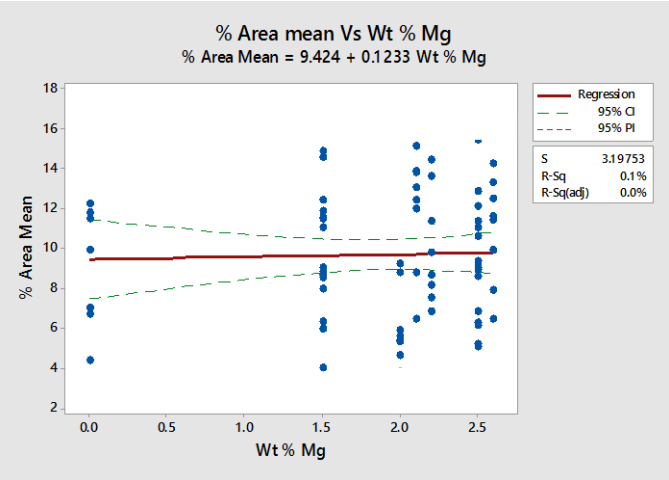

Figure 4.31 Regression plot showing the effect of alloy Mg content on the area fraction of the Al-Fe intermetallics formed.

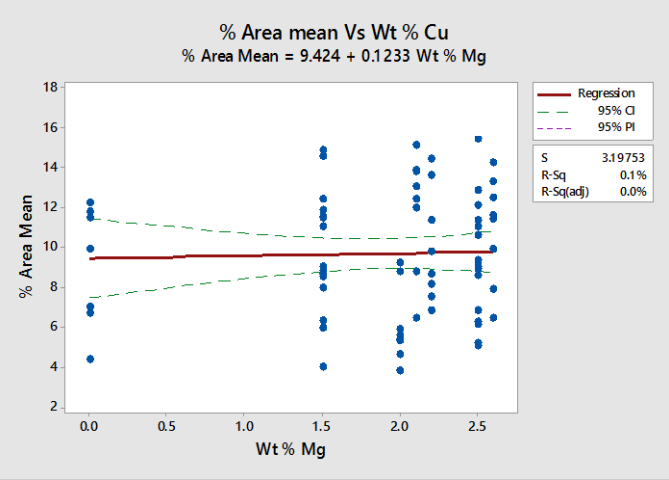

Figure 4.32 Regression plot showing the effect of alloy Cu content on the area fraction of the Al-Fe intermetallics formed.

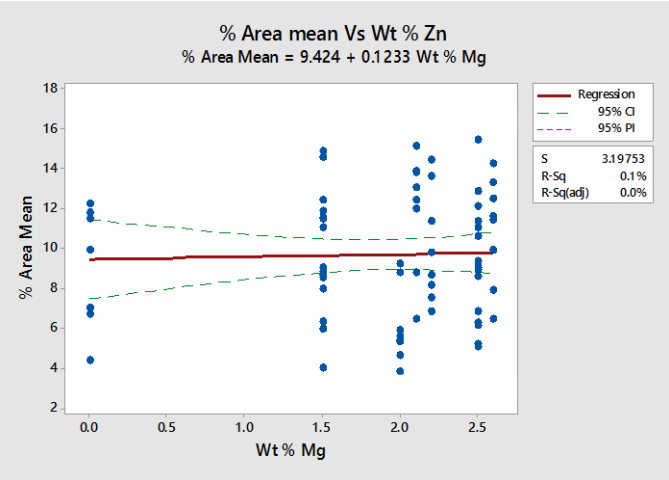

Figure 4.33 Regression plot showing the effect of alloy Zn content on the area fraction of the Al-Fe intermetallics formed.

The effect of cooling rate and alloy composition (Fe, Mg, Cu, and Zn content) on the area fraction of Fe-rich intermetallics is expressed by the following general regression equation:

Area Fraction Mean = 12.41 + 0.1222 CR + 0.025 wt % Cu - 1.470 wt % Fe + 0.126 wt % Mg - 0.310 wt % Zn

Equation 4.4

Table 4.12 P values corresponding to regression Equation 4.4

Variables	CR	wt% Fe	wt% Mg	wt% Cu	wt% Zn
P-values	0	0.051	0.79	0.94	0.12

The cooling rate and the alloy Fe content have significant multipliers in Equation 4.4. Removing the factors with P-values greater than 0.1 (see Table 5.18) gives the following simplified correlation equation:

% Area Fraction Mean = 12.90 + 0.1201 CR - 1.524 wt % Fe

Equation 4.5

4.7 Al-Fe intermetallic microstructure and mechanical properties

It has been firmly established from § 4.3 that the cooling rate has a strong influence on the morphology of the Fe intermetallic particles, the morphology of the intermetallics changes from globular to lamellar and further to long needle-like Al-Fe phases with increased volume fractions as the cooling rate decreases. Nevertheless, increasing in Fe levels always increases the Al-Fe intermetallics with high volume fractions, and hence the needle-like Al-Fe intermetallics, which can be controlled with high cooling rates.

The area fraction distribution curves in § 4.3.2 indicates that at TC locations having high cooling rates the intermetallics are spherical and polyhedral in shape which are relatively high in number and well distributed. These intermetallics are predominantly Al_6Fe having relatively low mass density. Figure 4.8 - 4.12 shows that the intermetallics at TC locations with lower cooling rates are having needle shape, star-like shape and bulky clusters with sharp edges and high aspect ratios. These intermetallics are determined as Al_3Fe having relatively high mass density.

Through microstructural observations (§ 4.2) it can be determined that the alloys solidified with cooling rates (approximately above 15 °C/s) yields a finely distributed

globular microstructure containing Al-Fe intermetallics of approximately within 1-5 µm in size. On the other hand, alloys solidified with low cooling rates (< 15 °C/s) are having sharp edged morphologies with high aspect ratios.

Intermetallics with sharp edges, specifically elongated needle shaped morphologies are detrimental for mechanical properties of the alloy; presence of these intermetallics limits the plastic deformation and induces the brittle fracture which consequently reduces the strength and elongation [6, 5, 22, 24, 27]. A typical fracture mechanism in the alloys with needle shaped Al-Fe intermetallics preferentially initiates at the interface between the needle-like intermetallic and Al matrix, under tensile loading a high stress concentration in the interface develops the crack formation which leads to brittle fracture prior to yield. The stress on the matrix near the intermetallics was calculated to be about 1.5 to 2 times that of the applied stress [31].

The study concludes that, for HPDC the alloys having higher Fe levels solidified with cooling rates approximately above (< 15 °C/s) having a well distributed globular shaped fine compact Al-Fe intermetallics preferably within 1-3 µm in size is highly desirable in order to achieve the desired mechanical properties. However, Fe levels should be optimized to balance the desired mechanical properties and die soldering advantageous.

In addition, a speculative assumption can be made that the increased volume fraction of the non deleterious finely distributed Al-Fe intermetallics may help in minimizing the die soldering tendency by decreasing the chemical potential gradient between aluminum melt and die steel. This hypothetical assumption can only be true provided the Fe levels are close / higher to solubility limit at near eutectic temperature of the alloy.

5. Conclusions

An investigation was conducted on the effect of alloy chemistry and cooling rate on the microstructural development focusing on the Al-Fe particle size, size distribution and chemistry of nine candidate AA7xxx+Fe alloys. The results obtained from this investigation can be summarized as follows:

1. It was determined that the dominant intermetallic species changes from the equilibrium Al_3Fe to the metastable Al_6Fe alloys for cooling rates in excess of approximately10 °C/s.
2. It was determined that the morphology of the Al-Fe particles transitions from a relatively low aspect ratio particles to a high aspect, needle-like particle for cooling rates less than approximately 10 °C/s.
3. Due to the above change in particle chemistry from Al_3Fe to Al_6Fe for cooling rates in excess of 10 °C/s, the area fraction of Al-Fe intermetallics within the microstructure increases in a manner consistent with obeying the global Fe mass balance in the alloy.

6. Appendix

A. Cooling curves for Alloy 2-9

Figure 6.1 - 6.8 complete set of cooling curves recorded from all eight TC locations (TC1-TC8) during directional solidification of Alloy 2-9

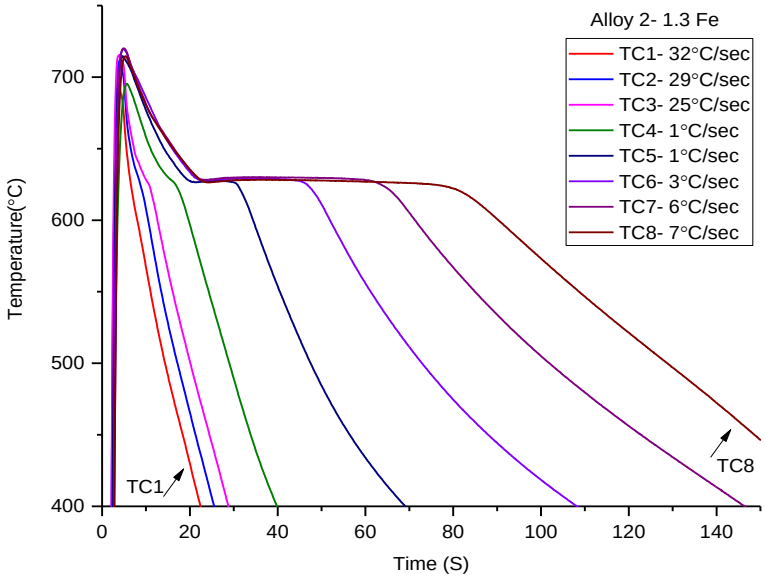

Figure 6.1 Cooling curves TC1-TC8 for Alloy 2

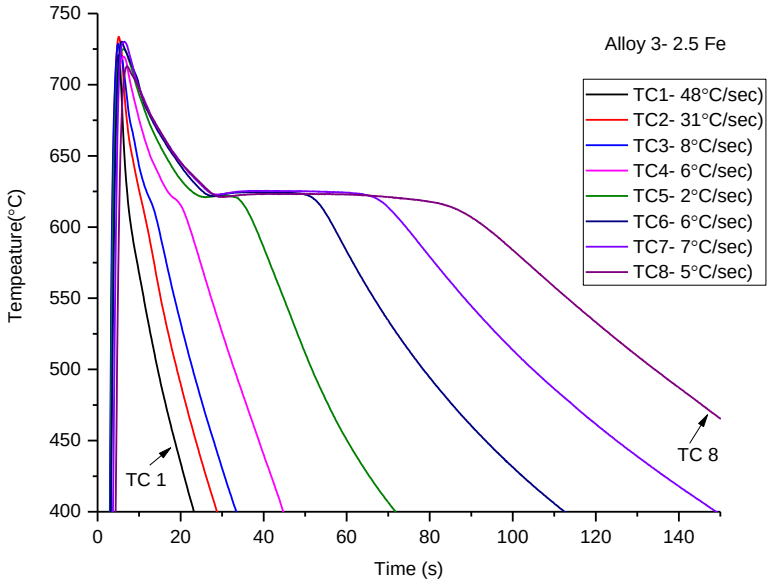

Figure 6.2 Cooling curves TC1-TC8 for Alloy 3

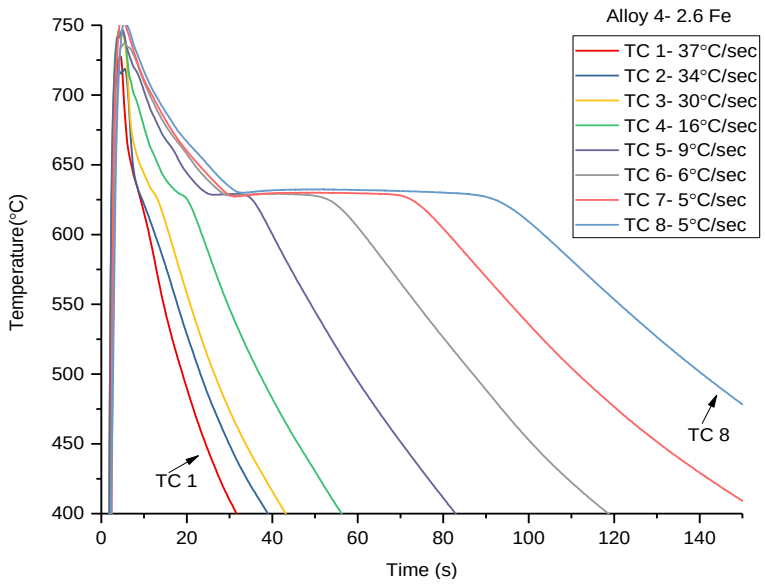

Figure 6.3 Cooling curves TC1-TC8 for Alloy 4

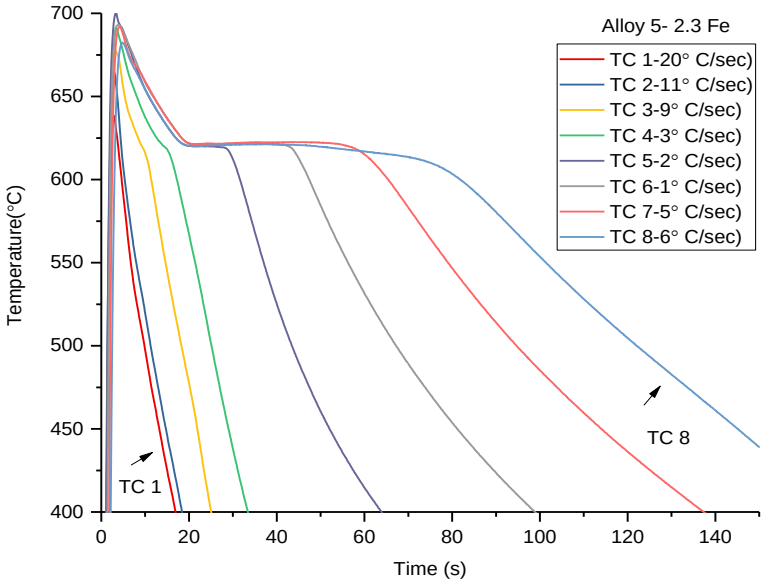

Figure 6.4 Cooling curves TC1-TC8 for Alloy 5

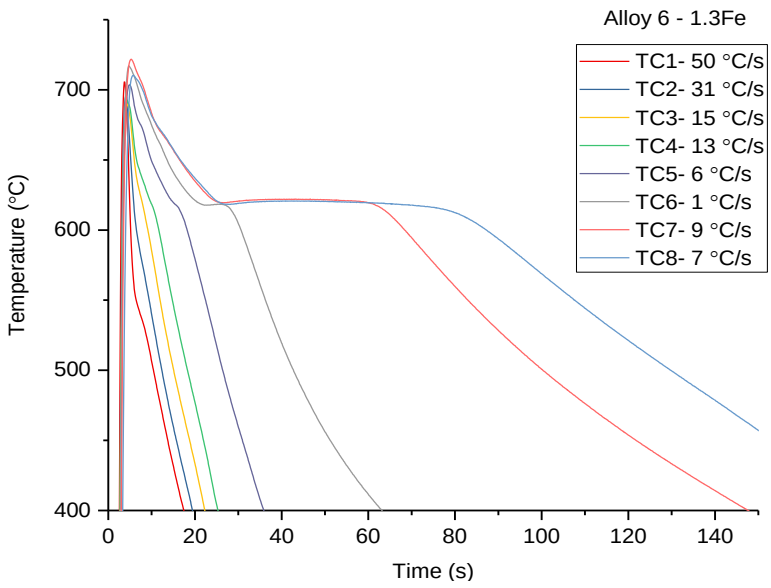

Figure 6.5 Cooling curves TC1-TC8 for Alloy 6

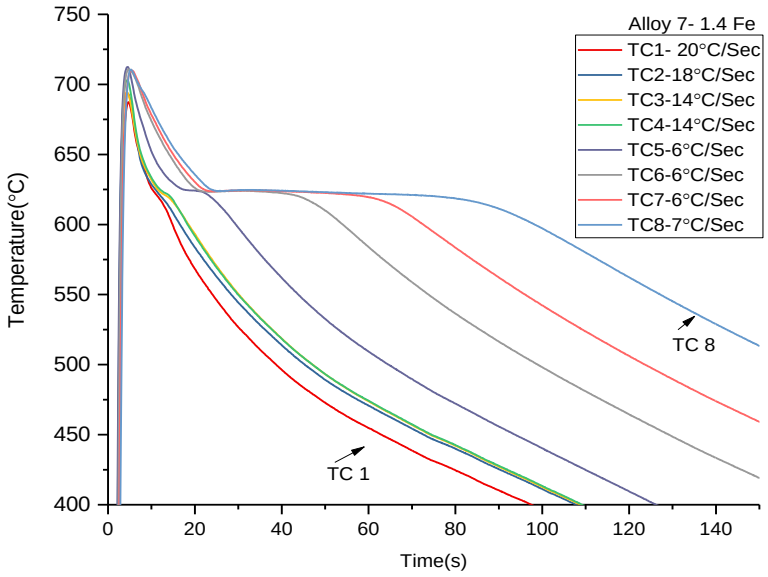

Figure 6.6 Cooling curves TC1-TC8 for Alloy 7

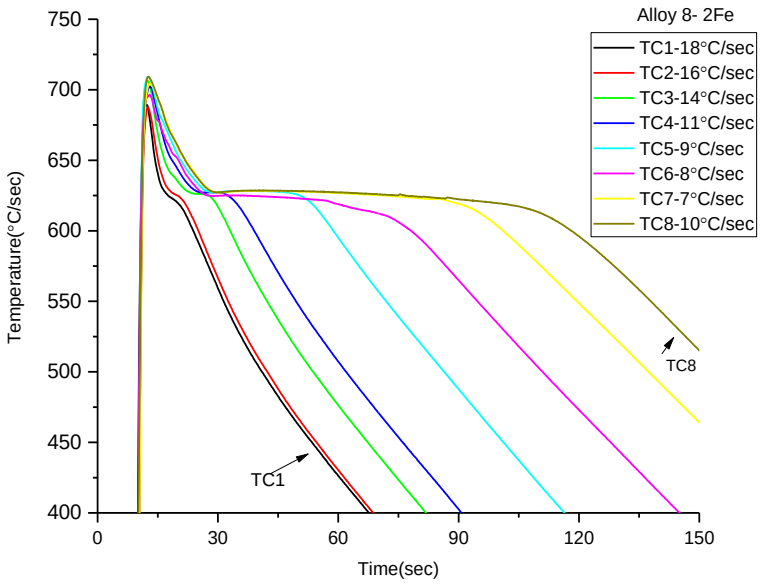

Figure 6.7 Cooling curves TC1-TC8 for Alloy 8

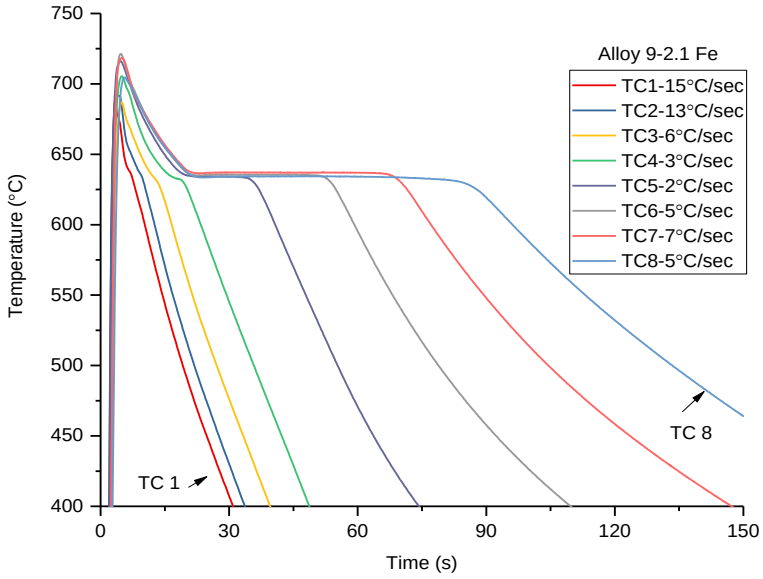

Figure 6.8 Cooling curves TC1-TC8 for Alloy 9

B. Cooling curves (TC1-TC8) with associated dT/dt curve and SEM images with associated EDX analysis table for alloy 2-9.

Alloy 2

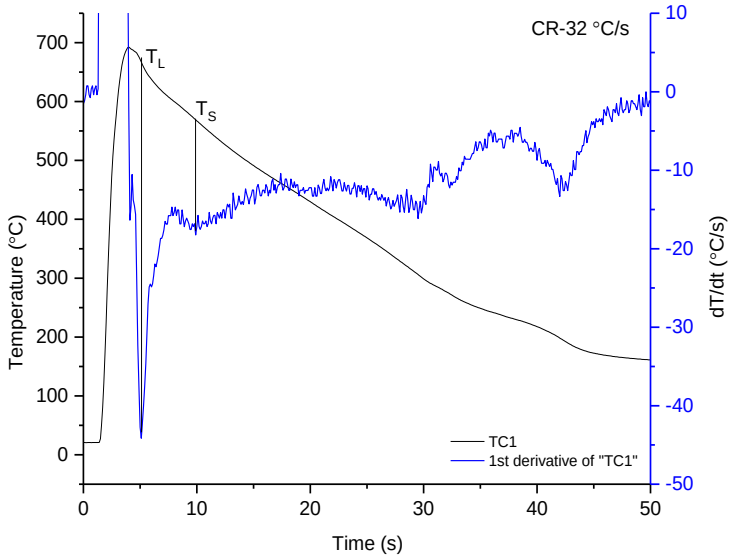

Figure 6.9 Cooling curve and the associated dT/dt curve for TC1 location

A 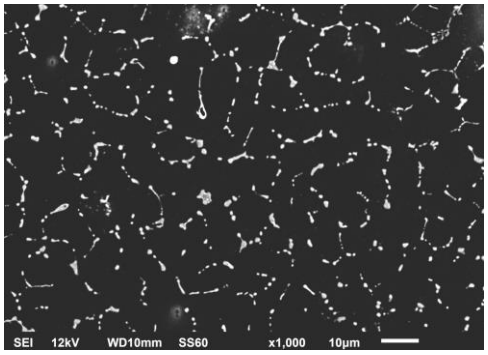

B 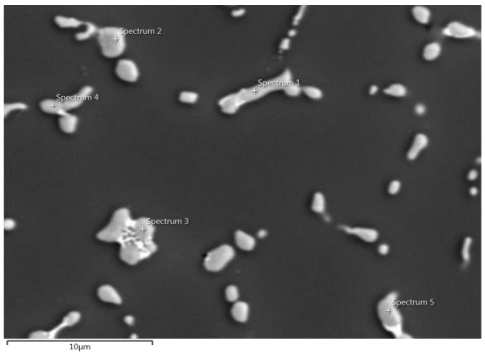

Figure 6.10 (A) SEM images of TC1 of Alloy 2 (B) Magnified EDS image used for Elemental analysis

Table 6.1 Elemental composition of intermetallics marked on Figure 6.10 B

Phase # as marked in the image	Al		Fe		
	wt%	at%	wt%	at%	phase
1	67	81	20	12	$FeAl_6$
2	69	82	24	14	$FeAl_6$
3	66	80	26	15	$FeAl_6$
4	66	80	20	12	$FeAl_6$
5	69	82	25	14	$FeAl_6$

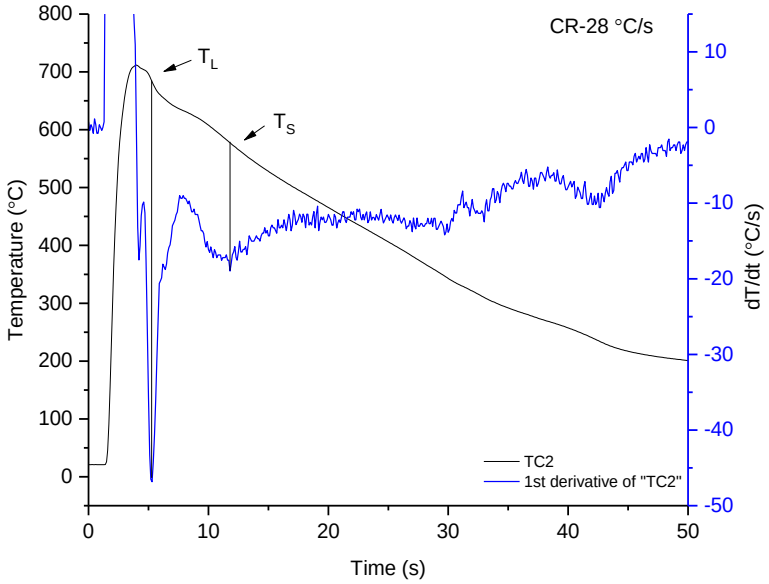

Figure 6.11 Cooling curve and the associated dT/dt curve for TC2 location

A 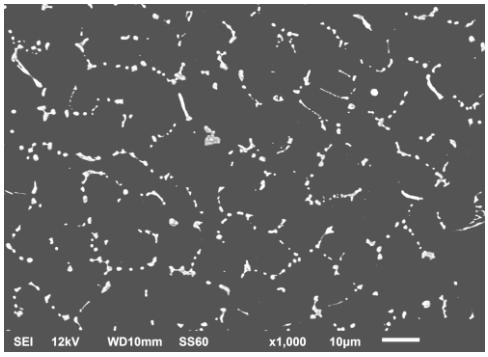

B 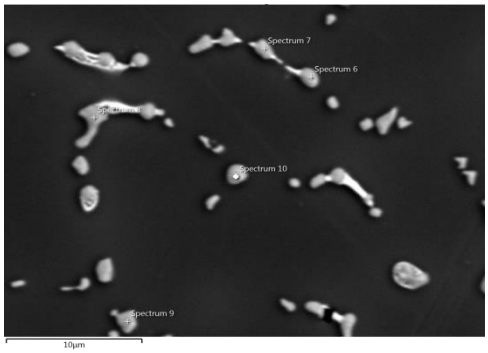

Figure 6.12 (A) SEM images of TC2 of Alloy 2 (B) Magnified EDS image used for Elemental analysis

Table 6.2 Elemental composition of intermetallics marked on Figure 6.12 B

Phase # as marked in the image	Al		Fe		
	wt%	at%	wt%	at%	phase
1	67	81	22	13	$FeAl_6$
2	70	83	23	14	$FeAl_6$
3	66	81	22	13	$FeAl_6$
4	66	81	22	13	$FeAl_6$
5	70	83	23	13	$FeAl_6$

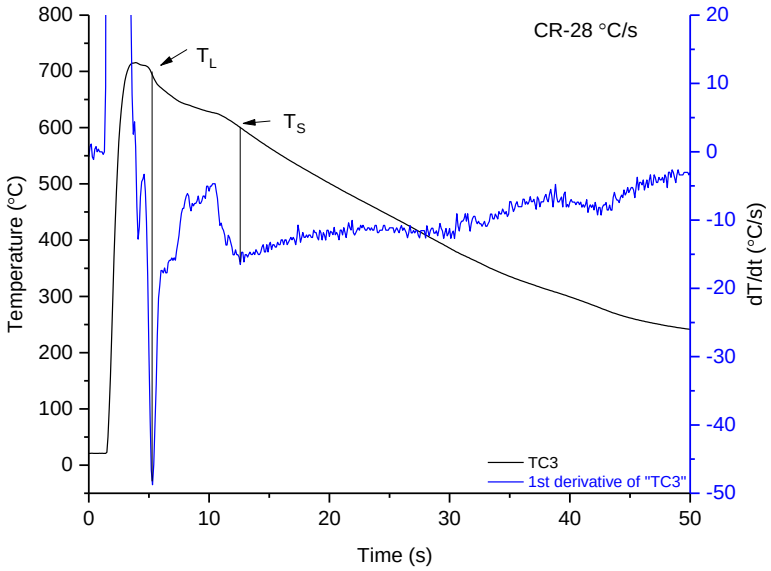

Figure 6.13 Cooling curve and the associated dT/dt curve for TC3 location

A 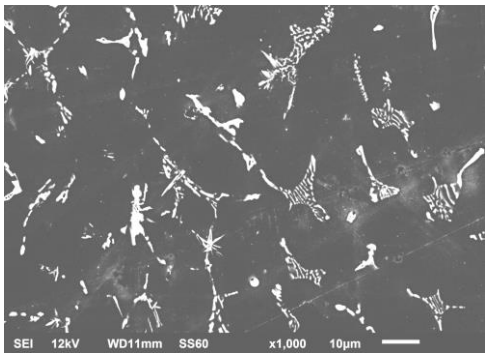

B 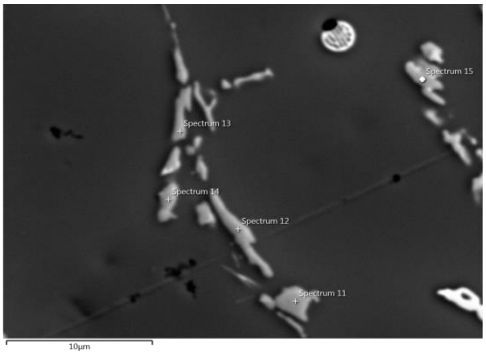

Figure 6.14 (A) SEM images of TC3 of Alloy 2 (B) Magnified EDS image used for Elemental analysis

Table 6.3 Elemental composition of intermetallics marked on Figure 6.14 B

Phase # as marked in the image	Al		Fe		
	wt%	at%	wt%	at%	phase
1	68	82	30	18	$FeAl_6$
2	71	83	28	16	$FeAl_6$
3	72	84	27	15	$FeAl_6$
4	69	82	29	17	$FeAl_6$
5	65	80	28	16	$FeAl_6$

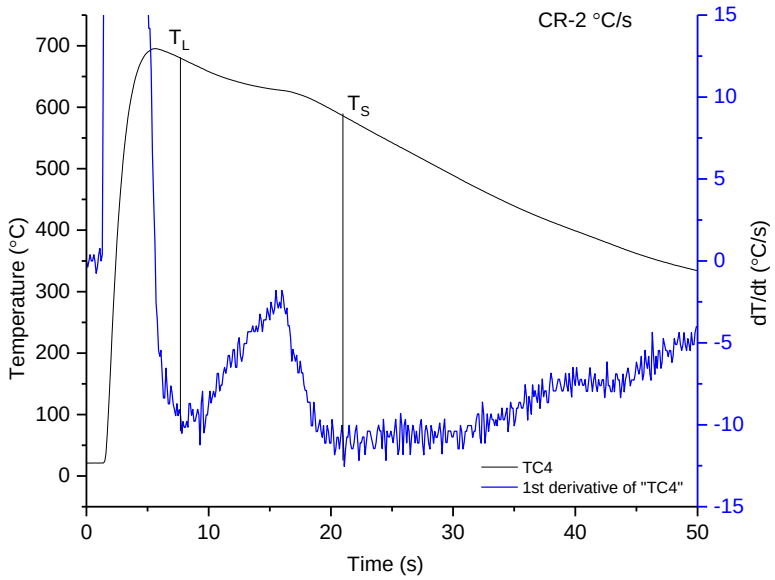

Figure 6.15 Cooling curve and the associated dT/dt curve for TC4 location

A 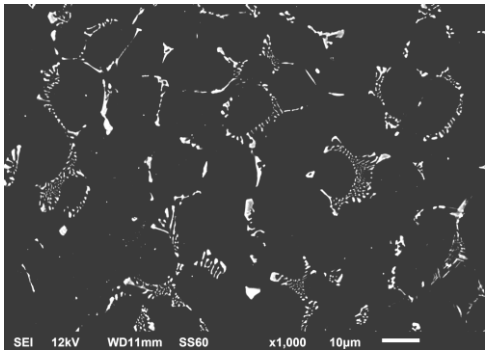

B 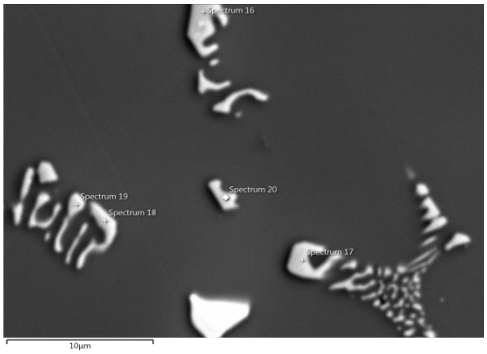

Figure 6.16 (A) SEM images of TC4 of Alloy 2 (B) Magnified EDS image used for Elemental analysis

Table 6.4 Elemental composition of intermetallics marked on Figure 6.16 B

Phase # as marked in the image	Al		Fe		
	wt%	at%	wt%	at%	phase
1	66	80	29	17	$FeAl_6$
2	67	80	30	18	$FeAl_6$
3	65	78	29	17	$FeAl_6$
4	65	80	28	17	$FeAl_6$
5	66	80	29	17	$FeAl_6$

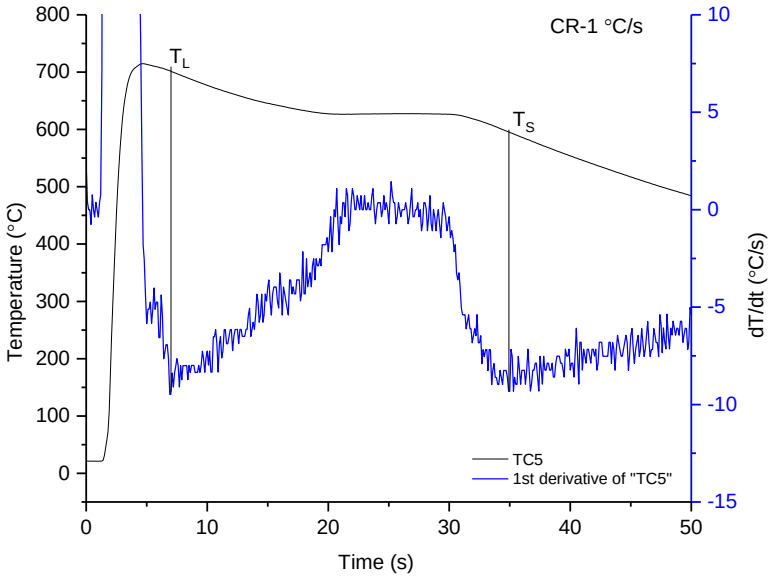

Figure 6.17 Cooling curve and the associated dT/dt curve for TC5 location

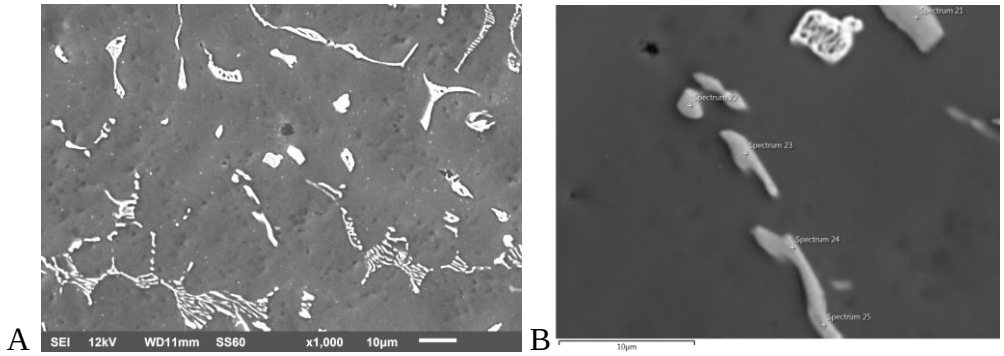

Figure 6.18 (A) SEM images of TC5 of Alloy 2 (B) Magnified EDS image used for Elemental analysis

Table 6.5 Elemental composition of intermetallics marked on Figure 6.18 B

Phase # as marked in the image	Al		Fe		
	wt%	at%	wt%	at%	phase
1	62	77	31	19	$FeAl_6$
2	63	78	30	18	$FeAl_6$
3	65	80	28	17	$FeAl_6$
4	68	82	25	15	$FeAl_6$
5	63	78	30	18	$FeAl_6$

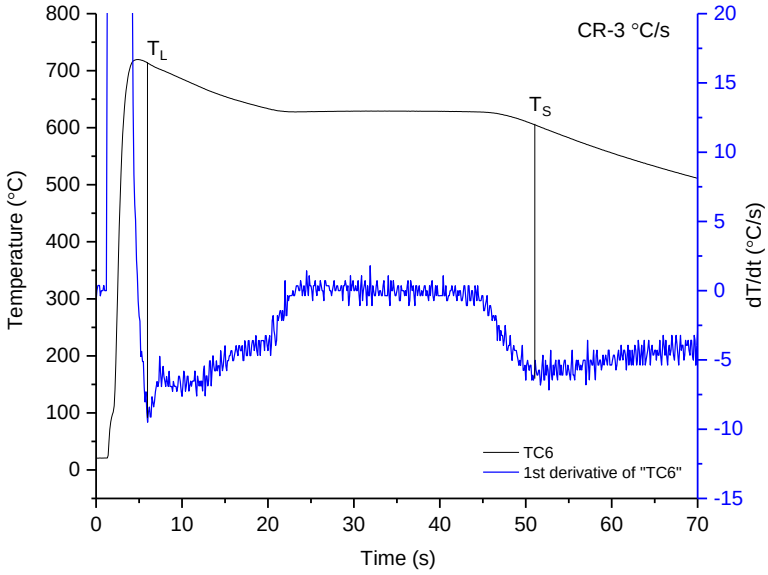

Figure 6.19 Cooling curve and the associated dT/dt curve for TC6 location

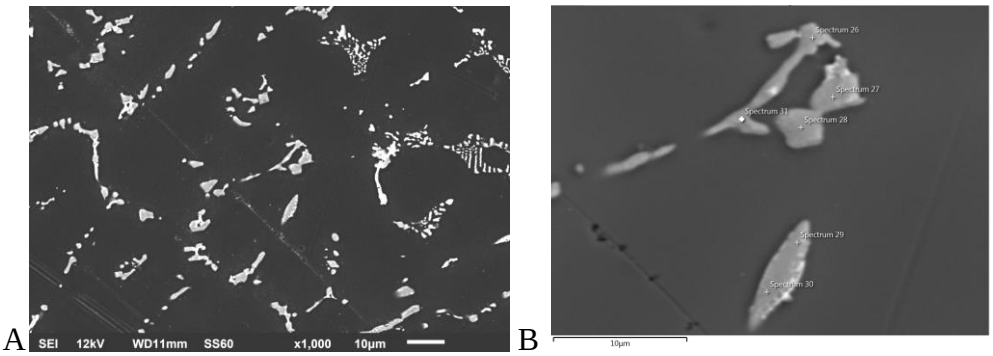

Figure 6.20 (A) SEM images of TC6 of Alloy 2 (B) Magnified EDS image used for Elemental analysis

Table 6.6 Elemental composition of intermetallics marked on Figure 6.20 B

Phase # as marked in the image	Al		Fe		
	wt%	at%	wt%	at%	phase
1	68	82	25	14	$FeAl_6$
2	68	82	25	14	$FeAl_6$
3	68	82	25	15	$FeAl_6$
4	65	80	23	14	$FeAl_6$
5	65	80	23	14	$FeAl_6$

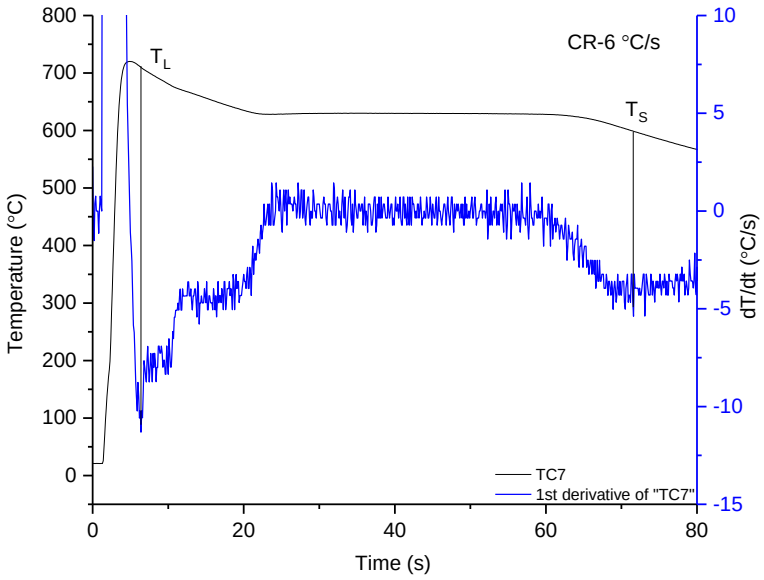

Figure 6.21 Cooling curve and the associated dT/dt curve for TC7 location

A 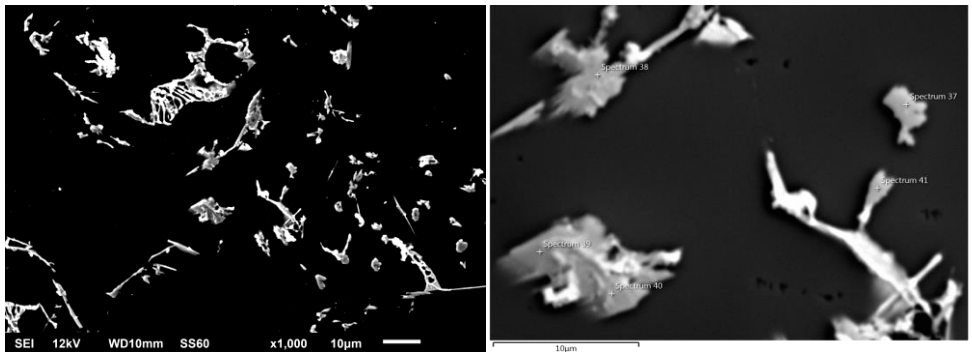

Figure 6.22 (A) SEM images of TC7 of Alloy 2 (B) Magnified EDS image used for Elemental analysis

Table 6.7 Elemental composition of intermetallics marked on Figure 6.22 B

Phase # as marked in the image	Al		Fe		
	wt%	at%	wt%	at%	phase
1	60	76	36	22	$FeAl_3$
2	61	77	32	20	$FeAl_3$
3	61	76	35	21	$FeAl_3$
4	58	74	34	21	$FeAl_3$
5	63	76	35	21	$FeAl_3$

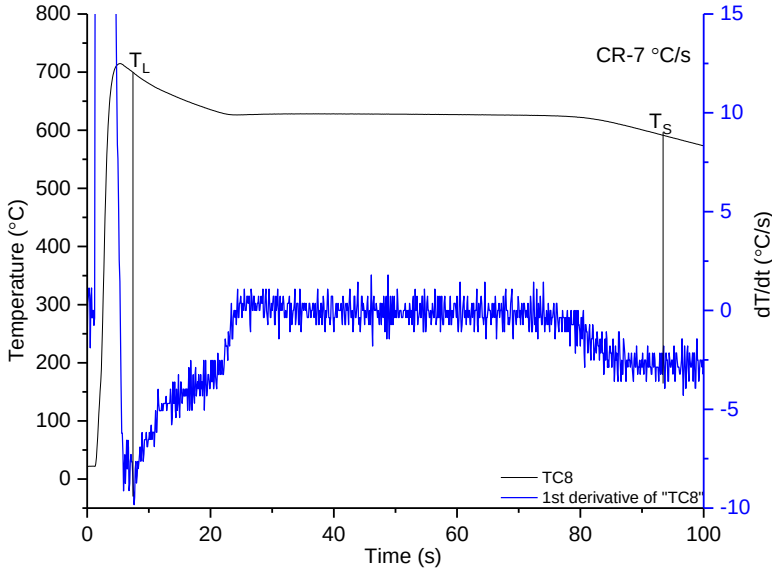

Figure 6.23 Cooling curve and the associated dT/dt curve for TC8 location

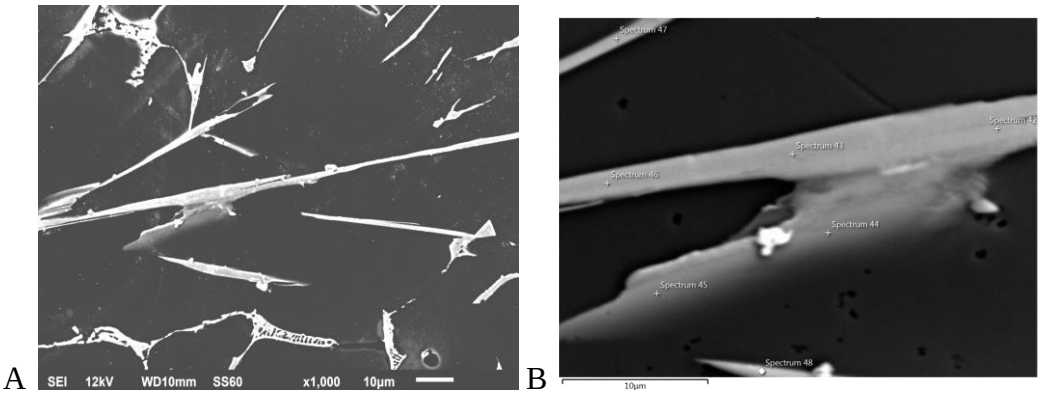

A B

Figure 6.24 (A) SEM images of TC8 of Alloy 2 (B) Magnified EDS image used for Elemental analysis

Table 6.8 Elemental composition of intermetallics marked on Figure 6.24 B

Phase # as marked in the image	Al		Fe		
	wt%	at%	wt%	at%	phase
1	63	78	34	21	$FeAl_6$
2	62	77	36	22	$FeAl_3$
3	72	84	27	15	$FeAl_6$
4	76	86	26	14	$FeAl_6$
5	62	77	35	21	$FeAl_3$

Alloy 3

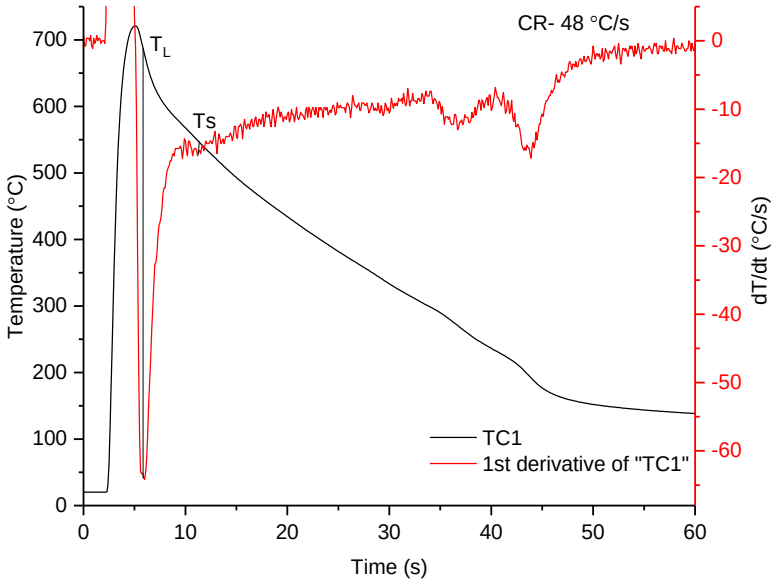

Figure 6.25 Cooling curve and the associated dT/dt curve for TC1 location

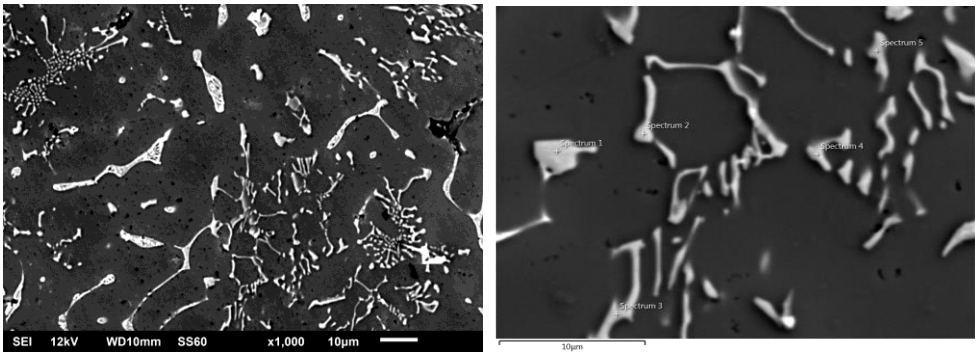

Figure 6.26 (A) SEM images of TC1 of Alloy 3
(B) Magnified EDS image used for
Elemental analysis

Table 6.9 Elemental composition of intermetallics marked on Figure 6.26 B

Phase # as marked in the image	Al		Fe		
	wt%	at%	wt%	at%	phase
1	62	77	29	18	$FeAl_6$
2	68	81	25	15	$FeAl_6$
3	69	82	24	14	$FeAl_6$
4	66	81	27	16	$FeAl_6$
5	70	83	25	15	$FeAl_6$

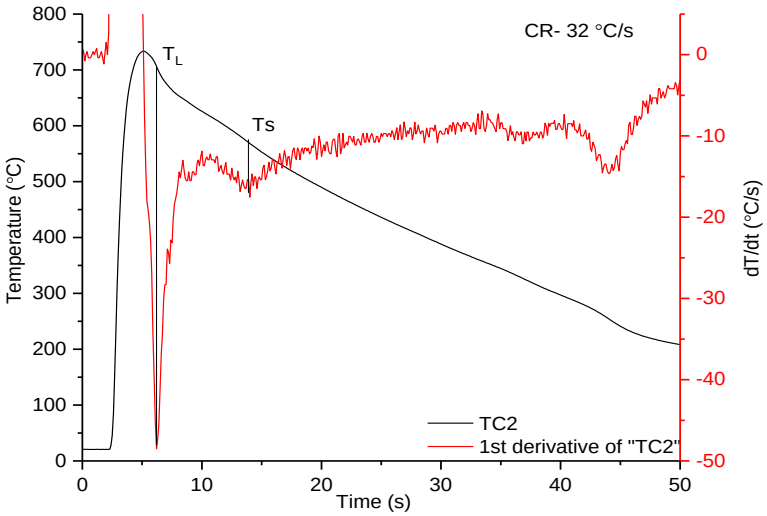

Figure 6.27 Cooling curve and the associated dT/dt curve for TC2 location

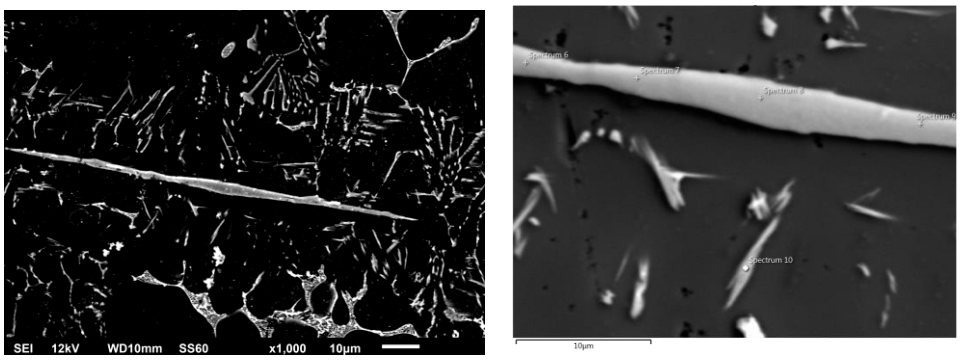

Figure 6.28 (A) SEM images of TC2 of Alloy 3 (B) Magnified EDS image used for Elemental analysis

Table 6.10 Elemental composition of intermetallics marked on Figure 6.28 B

Phase # as marked in the image	Al		Fe		
	wt%	at%	wt%	at%	phase
1	62	77	35	21	$FeAl_6$
2	62	73	36	22	$FeAl_3$
3	61	76	36	22	$FeAl_3$
4	61	77	36	22	$FeAl_3$
5	67	80	27	16	$FeAl_6$

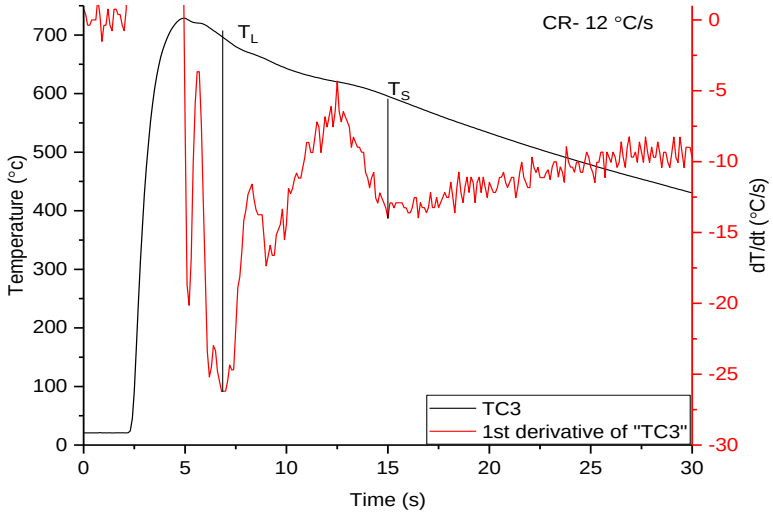

Figure 6.29 Cooling curve and the associated dT/dt curve for TC3 location

A 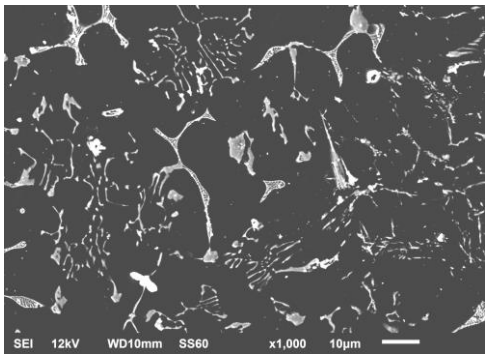

B 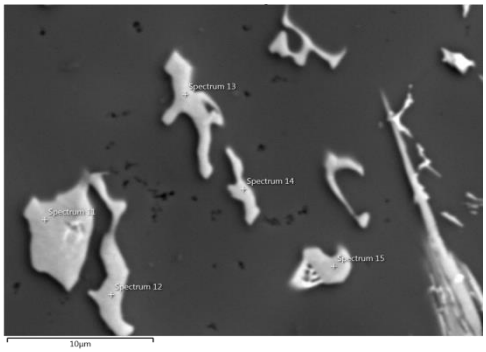

Figure 6.30 (A) SEM images of TC3 of Alloy 3 (B) Magnified EDS image used for Elemental analysis

Table 6.11 Elemental composition of intermetallics marked on Figure 6.30 B

Phase # as marked in the image	Al		Fe		
	wt%	at%	wt%	at%	phase
1	65	79	29	17	$FeAl_6$
2	63	79	30	18	$FeAl_6$
3	64	78	27	16	$FeAl_6$
4	66	80	30	18	$FeAl_6$
5	64	79	32	19	$FeAl_6$

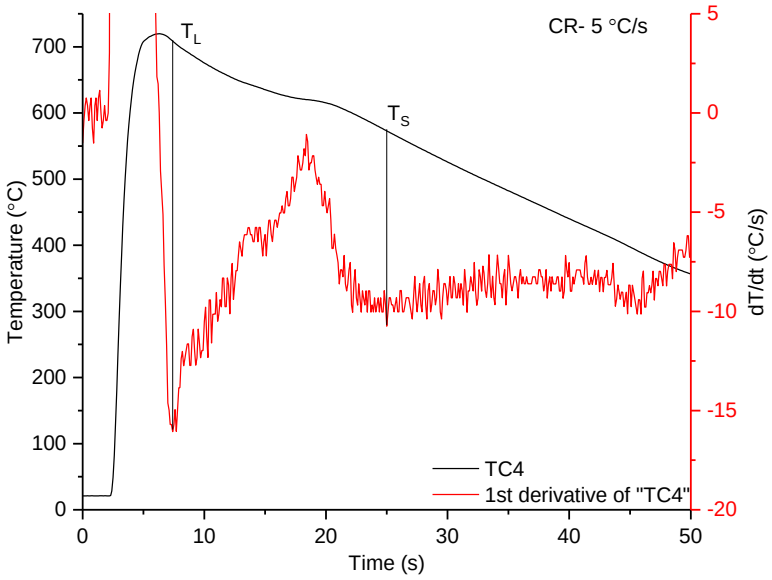

Figure 6.31 Cooling curve and the associated dT/dt curve for TC4 location

A 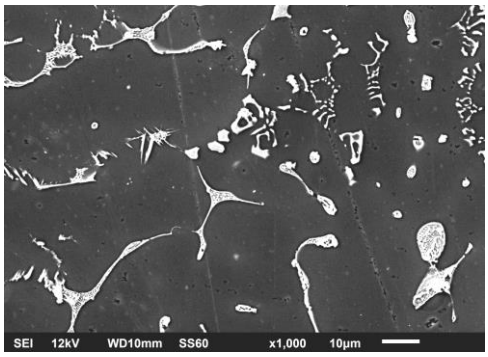

B 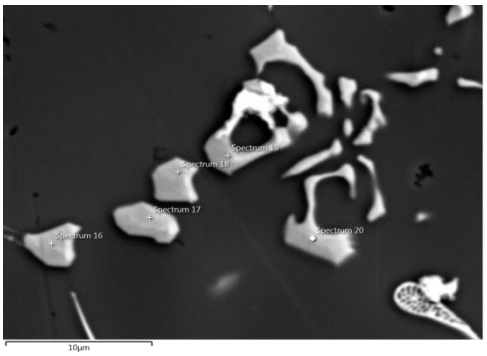

Figure 6.32 (A) SEM images of TC4 of Alloy 3 (B) Magnified EDS image used for Elemental analysis

Table 6.12 Elemental composition of intermetallics marked on Figure 6.32 B

Phase # as marked in the image	Al		Fe		
	wt%	at%	wt%	at%	phase
1	61	77	29	18	$FeAl_6$
2	61	77	29	18	$FeAl_6$
3	62	78	30	18	$FeAl_6$
4	68	78	24	14	$FeAl_6$
5	61	77	30	18	$FeAl_6$

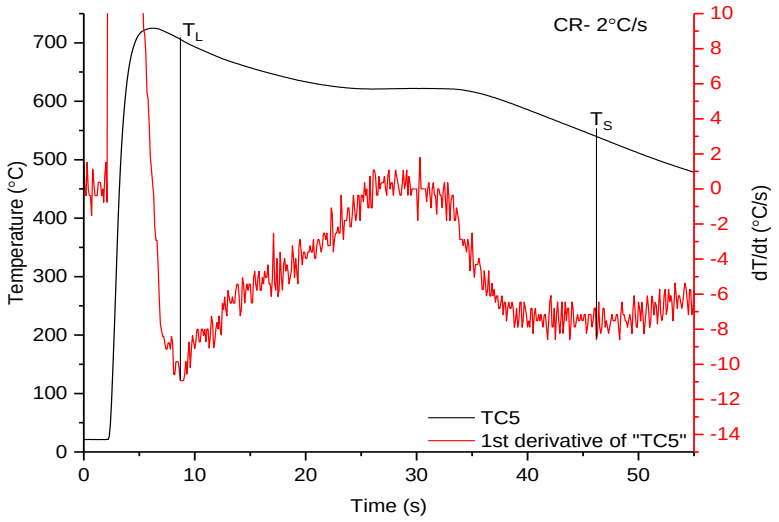

Figure 6.33 Cooling curve and the associated dT/dt curve for TC5 location

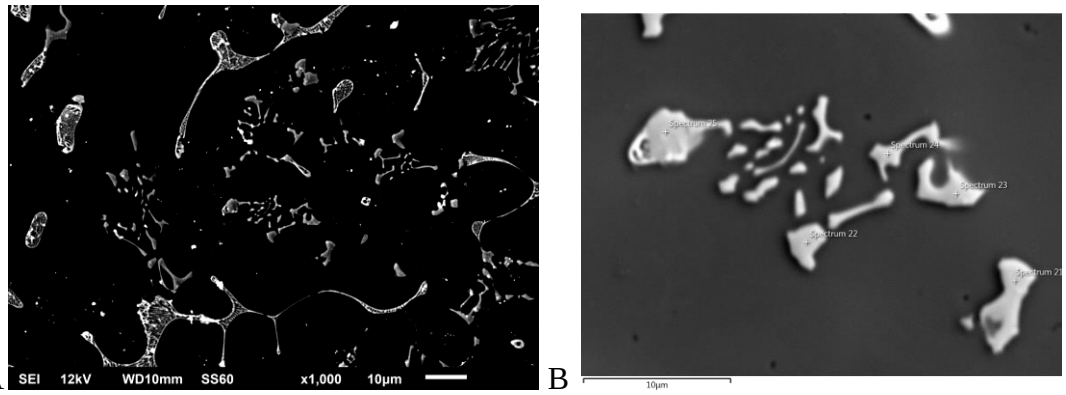

A B

Figure 6.34 (A) SEM images of TC5 of Alloy 3 (B) Magnified EDS image used for Elemental analysis

Table 6.13 Elemental composition of intermetallics marked on Figure 6.34 B

Phase # as marked in the image	Al		Fe		
	wt%	at%	wt%	at%	phase
1	63	78	30	18	$FeAl_6$
2	64	79	30	18	$FeAl_6$
3	63	79	30	18	$FeAl_6$
4	64	79	29	17	$FeAl_6$
5	62	77	30	18	$FeAl_6$

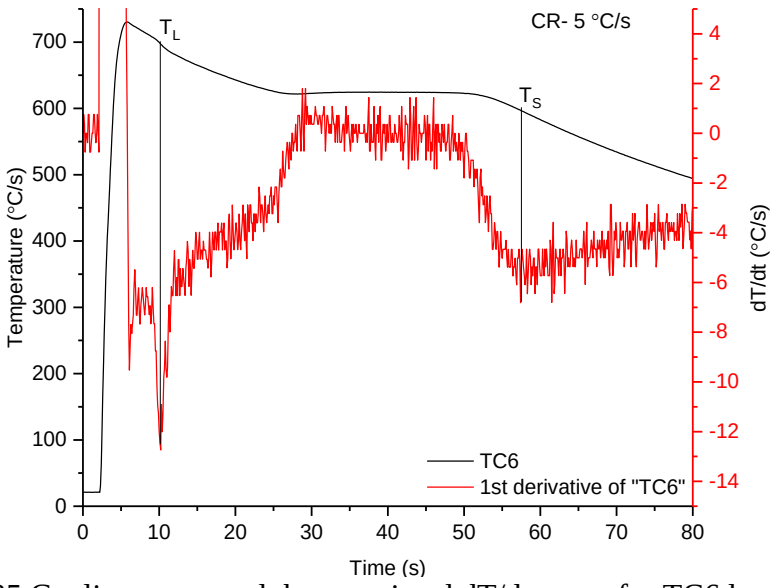

Figure 6.35 Cooling curve and the associated dT/dt curve for TC6 location

A 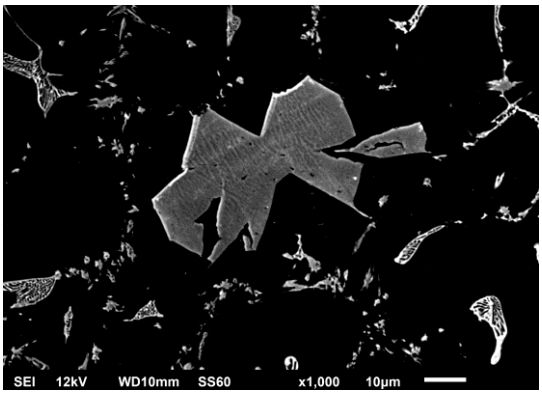

B 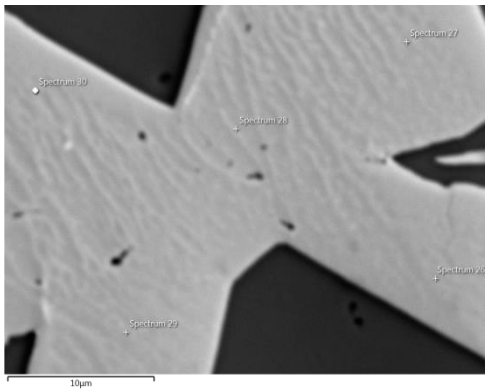

Figure 6.36 (A) SEM images of TC6 of Alloy 3 (B) Magnified EDS image used for Elemental analysis

Table 6.14 Elemental composition of intermetallics marked on Figure 6.36 B

Phase # as marked in the image	Al		Fe		
	wt%	at%	wt%	at%	phase
1	61	76	36	22	$FeAl_3$
2	61	76	37	22	$FeAl_3$
3	61	76	37	22	$FeAl_3$
4	61	76	37	22	$FeAl_3$
5	61	76	37	22	$FeAl_3$

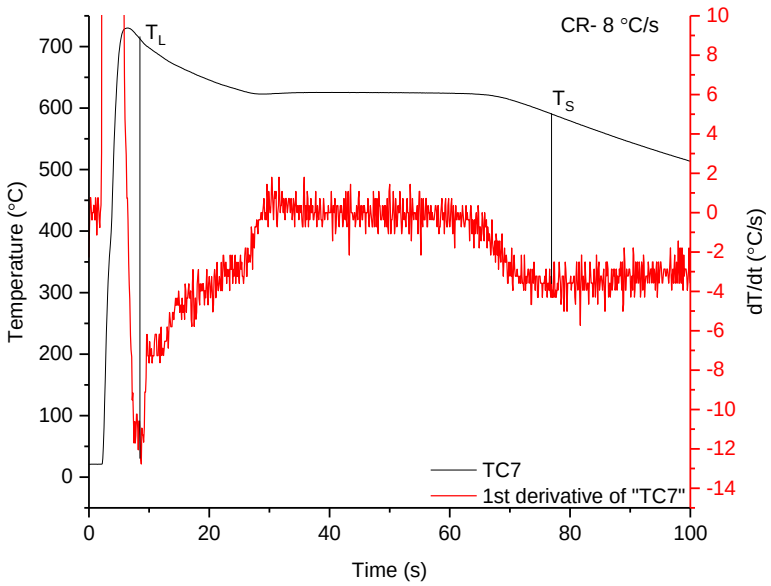

Figure 6.37 Cooling curve and the associated dT/dt curve for TC7 location

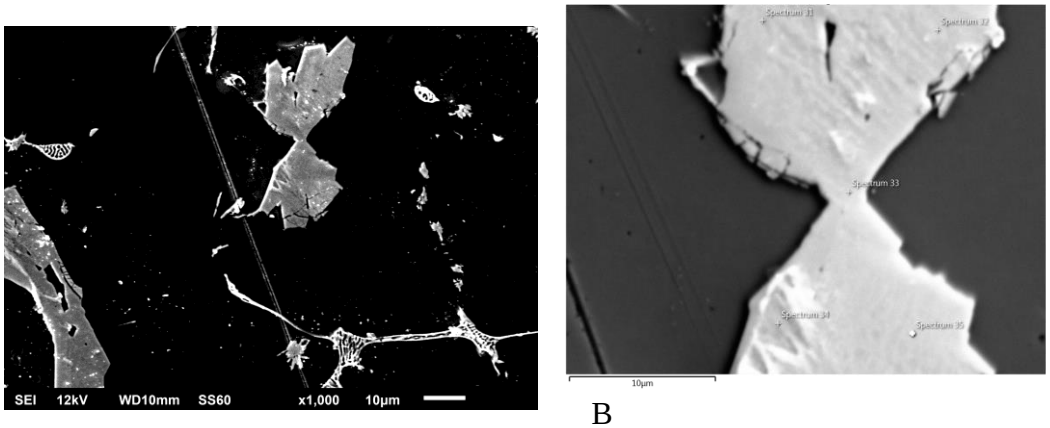

A = B

Figure 6.38 (A) SEM images of TC7 of Alloy 3 (B) Magnified EDS image used for Elemental analysis

Table 6.15 Elemental composition of intermetallics marked on Figure 6.38 B

Phase # as marked in the image	Al		Fe		
	wt%	at%	wt%	at%	phase
1	61	76	37	22	$FeAl_3$
2	60	76	37	23	$FeAl_3$
3	60	76	37	23	$FeAl_3$
4	60	76	37	22	$FeAl_3$
5	60	76	37	23	$FeAl_3$

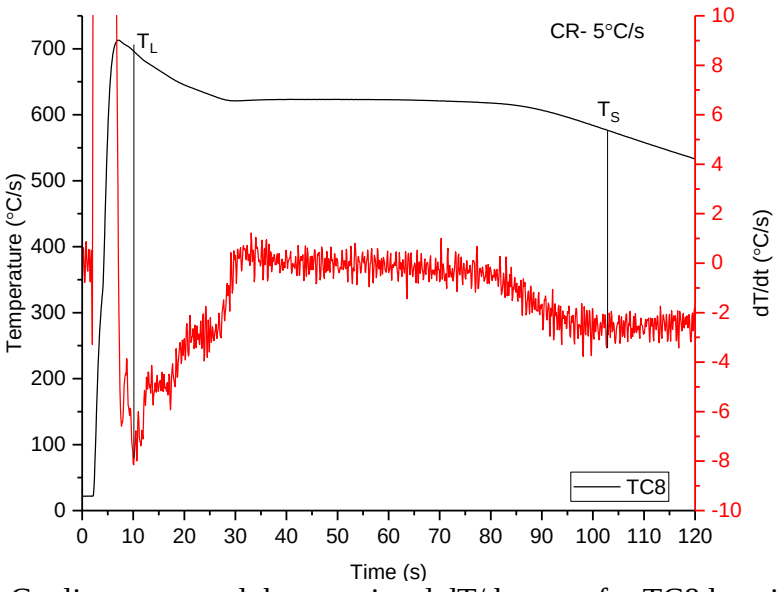

Figure 6.39 Cooling curve and the associated dT/dt curve for TC8 location

A 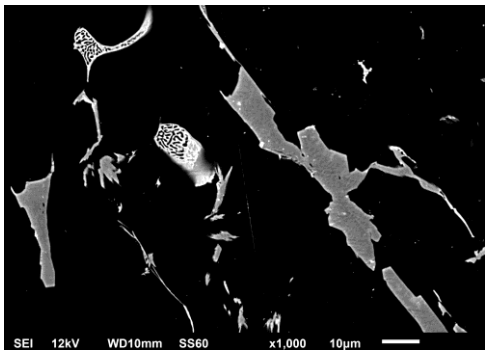

B 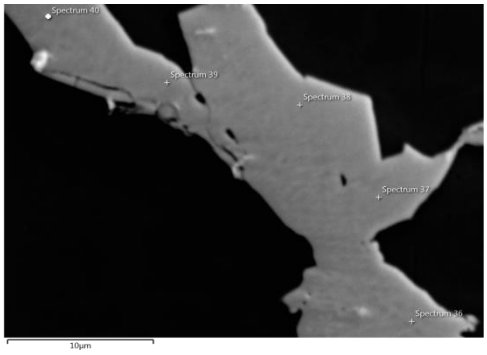

Figure 6.40 (A) SEM images of TC8 of Alloy 3 (B) Magnified EDS image used for Elemental analysis

Table 6.16 Elemental composition of intermetallics marked on Figure 6.40 B

Phase # as marked in the image	Al		Fe		
	wt%	at%	wt%	at%	phase
1	61	77	36	22	$FeAl_3$
2	61	76	37	23	$FeAl_3$
3	60	76	37	22	$FeAl_3$
4	61	77	36	22	$FeAl_3$
5	61	77	36	22	$FeAl_3$

Alloy 4

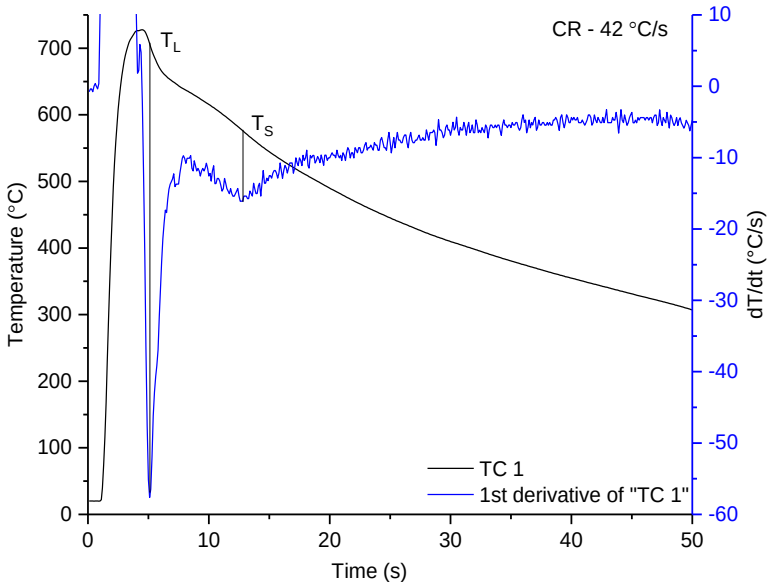

Figure 6.41 Cooling curve and the associated dT/dt curve for TC1 location

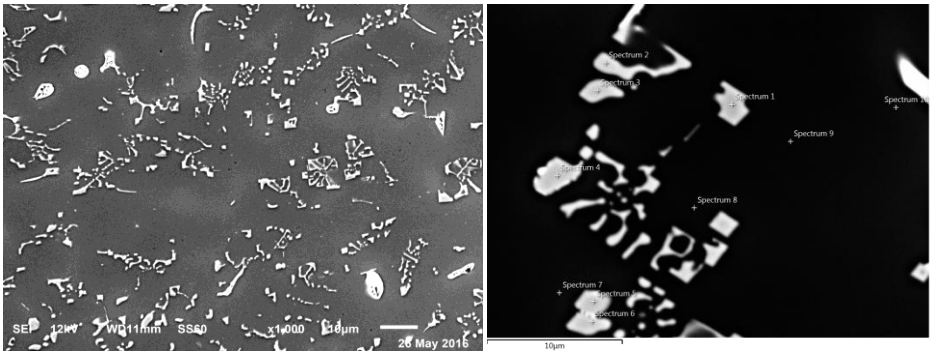

Figure 6.42 (A) SEM images of TC1 of Alloy 4 (B) Magnified EDS image used for Elemental analysis

Table 6.17 Elemental composition of intermetallics marked on Figure 6.42 B

Phase # as marked in the image	Al		Fe		
	wt%	at%	wt%	at%	phase
1	68	82	22	13	$FeAl_6$
2	67	81	21	12	$FeAl_6$
3	66	81	22	13	$FeAl_6$
4	66	80	23	14	$FeAl_6$
5	66	81	22	13	$FeAl_6$

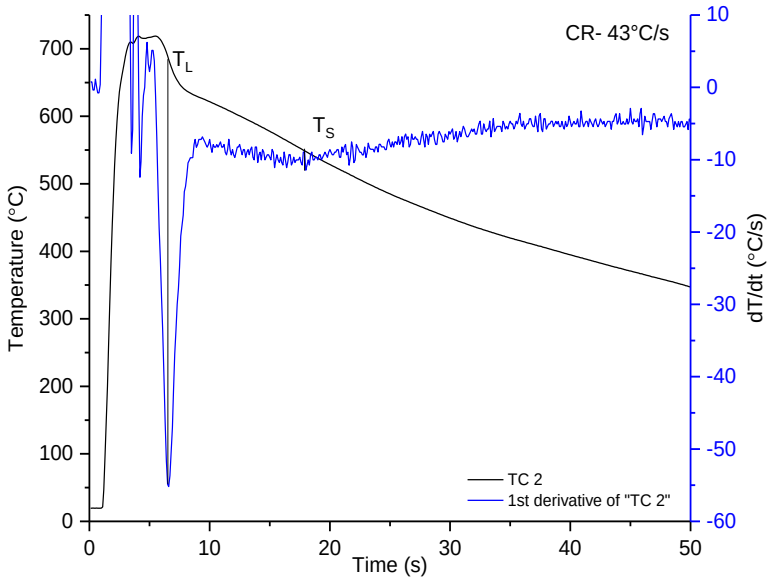

Figure 6.43 Cooling curve and the associated dT/dt curve for TC2 location

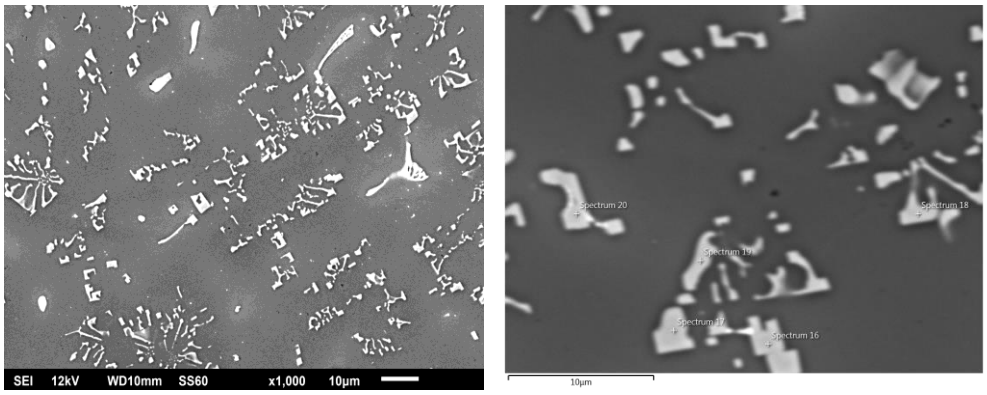

Figure 6.44 (A) SEM images of TC2 of Alloy 4 (B) Magnified EDS image used for Elemental analysis

Table 6.18 Elemental composition of intermetallics marked on Figure 6.44 B

Phase # as marked in the image	Al		Fe		
	wt%	at%	wt%	at%	phase
1	66	81	22	13	$FeAl_6$
2	67	81	23	13	$FeAl_6$
3	68	82	22	13	$FeAl_6$
4	67	82	21	12	$FeAl_6$
5	64	79	22	13	$FeAl_6$

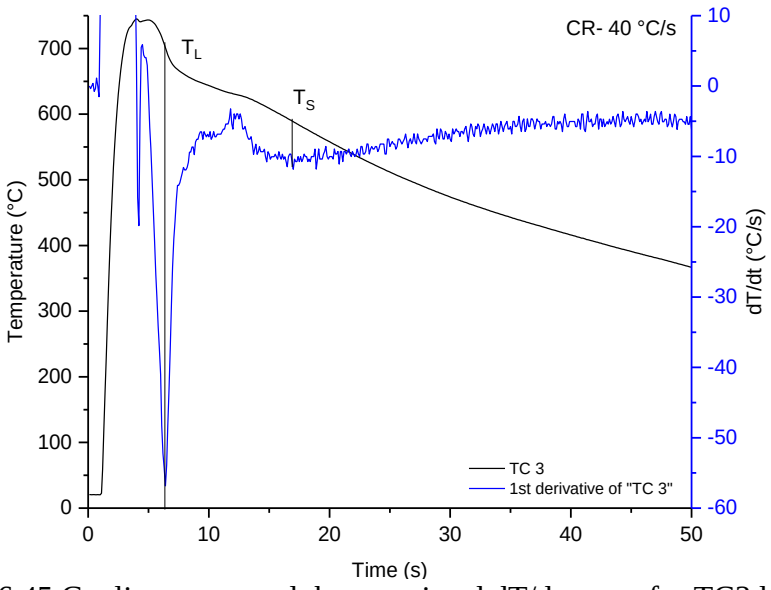

Figure 6.45 Cooling curve and the associated dT/dt curve for TC3 location

A 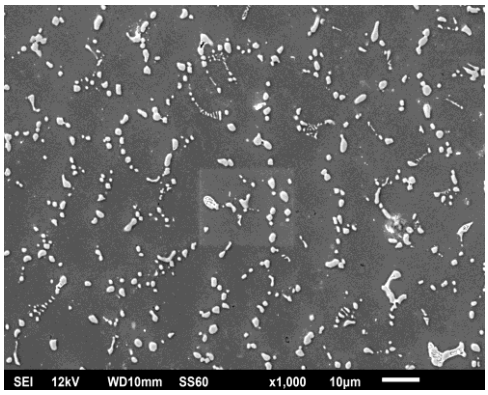

B 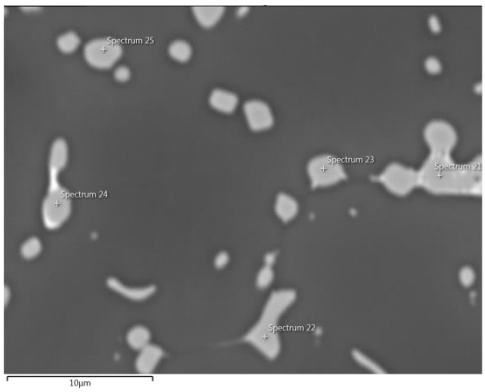

Figure 6.46 (A) SEM images of TC3 of Alloy 4 (B) Magnified EDS image used for Elemental analysis

Table 6.19 Elemental composition of intermetallics marked on Figure 6.46 B

Phase # as marked in the image	Al		Fe		
	wt%	at%	wt%	at%	phase
1	66	80	23	14	$FeAl_6$
2	66	81	23	14	$FeAl_6$
3	66	81	22	13	$FeAl_6$
4	65	80	23	14	$FeAl_6$
5	66	81	22	13	$FeAl_6$

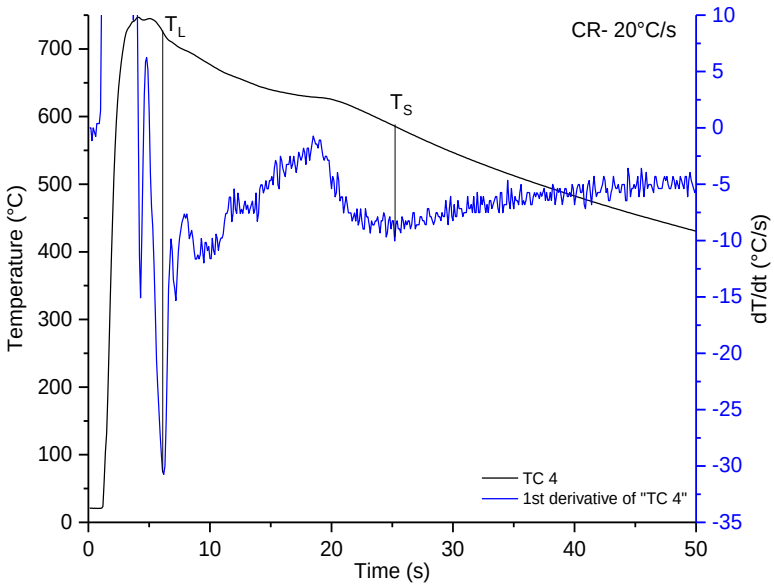

Figure 6.47 Cooling curve and the associated dT/dt curve for TC4 location

A 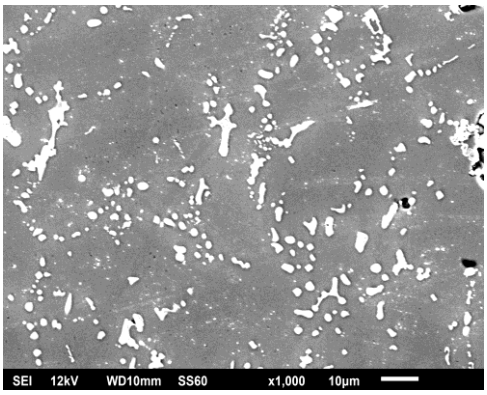

B 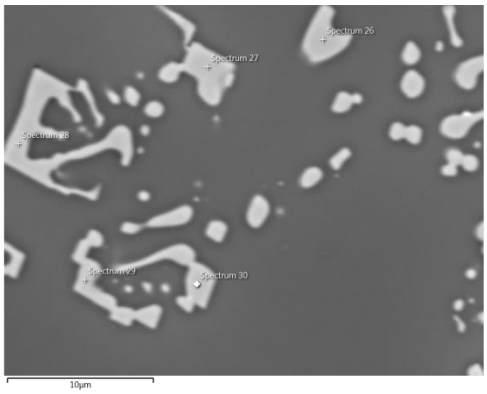

Figure 6.48 (A) SEM images of TC4 of Alloy 4 (B) Magnified EDS image used for Elemental analysis

Table 6.20 Elemental composition of intermetallics marked on Figure 6.48 B

Phase # as marked in the image	Al		Fe		
	wt%	at%	wt%	at%	phase
1	67	81	23	13	$FeAl_6$
2	66	81	23	13	$FeAl_6$
3	66	81	22	13	$FeAl_6$
4	67	81	21	12	$FeAl_6$
5	66	81	22	13	$FeAl_6$

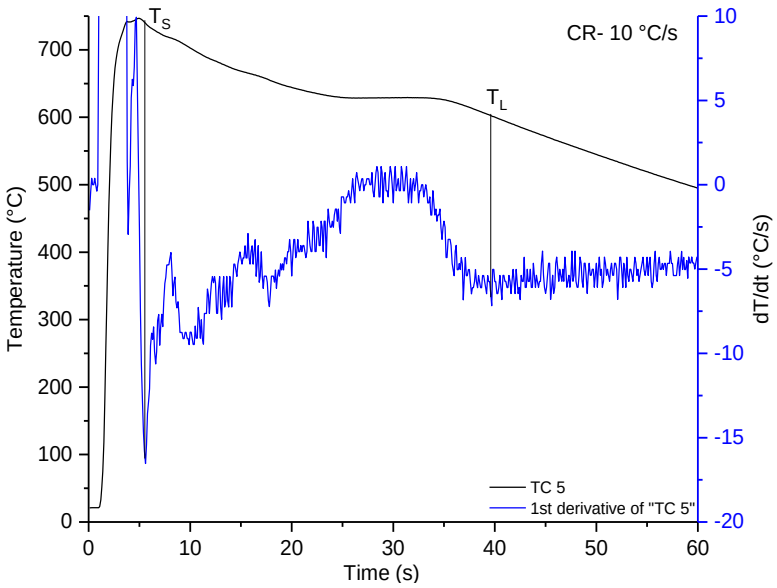

Figure 6.49 Cooling curve and the associated dT/dt curve for TC5 location

A 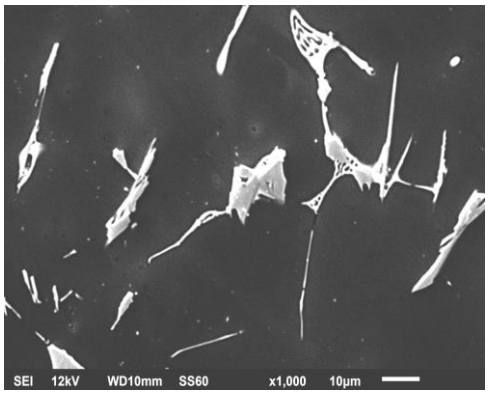

B 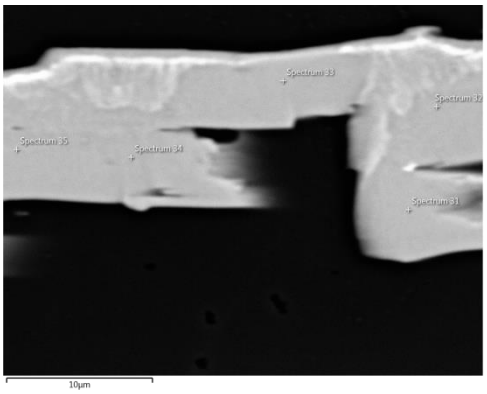

Figure 6.50 (A) SEM images of TC5 of Alloy 4 (B) Magnified EDS image used for Elemental analysis

Table 6.21 Elemental composition of intermetallics marked on Figure 6.50 B

Phase # as marked in the image	Al		Fe		
	wt%	at%	wt%	at%	phase
1	61	72	36	22	$FeAl_3$
2	61	76	37	22	$FeAl_3$
3	61	77	37	22	$FeAl_3$
4	61	77	36	22	$FeAl_3$
5	61	76	36	22	$FeAl_3$

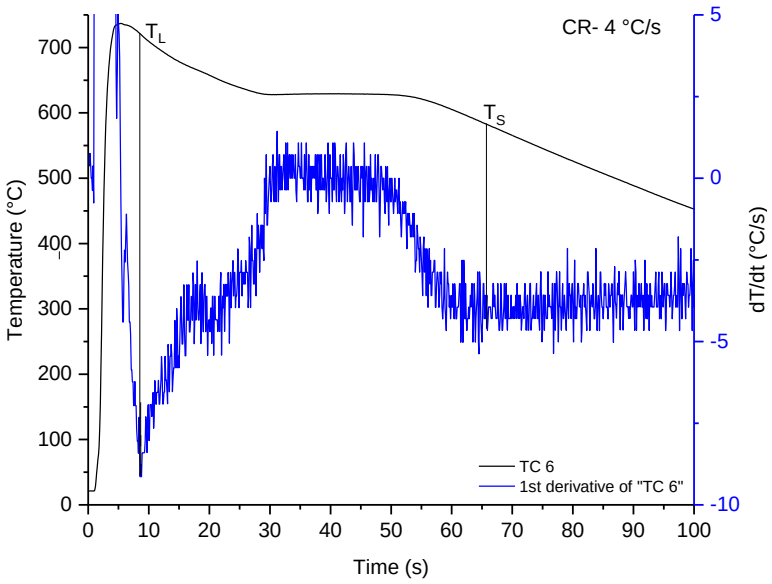

Figure 6.51 Cooling curve and the associated dT/dt curve for TC6 location

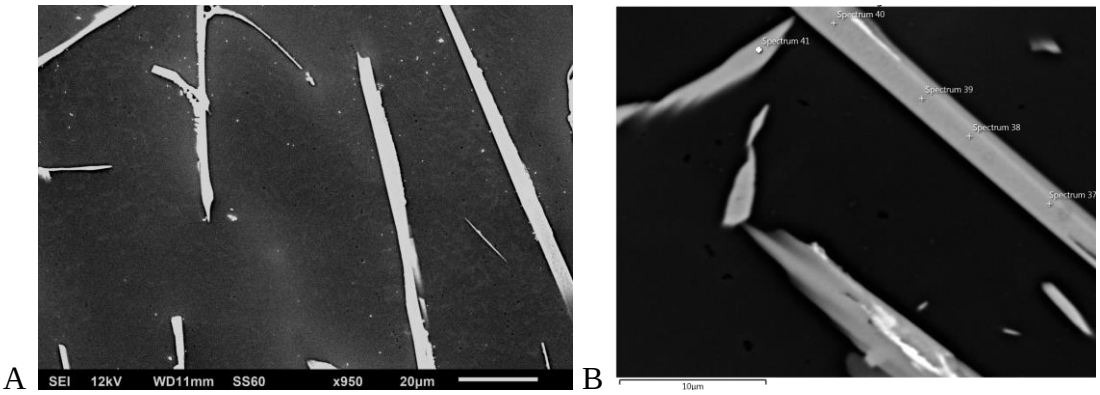

Figure 6.52 (A) SEM images of TC6 of Alloy 4 (B) Magnified EDS image used for Elemental analysis

Table 6.22 Elemental composition of intermetallics marked on Figure 6.52 B

Phase # as marked in the image	Al		Fe		
	wt%	at%	wt%	at%	phase
1	61	76	37	23	$FeAl_3$
2	61	76	37	22	$FeAl_3$
3	61	76	37	22	$FeAl_3$
4	62	77	36	22	$FeAl_3$
5	62	78	34	21	$FeAl_6$

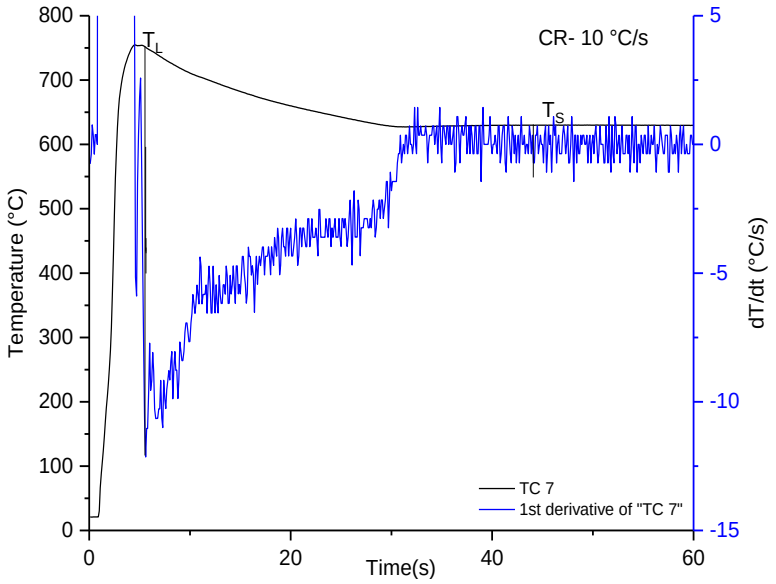

Figure 6.53 Cooling curve and the associated dT/dt curve for TC7 location

A 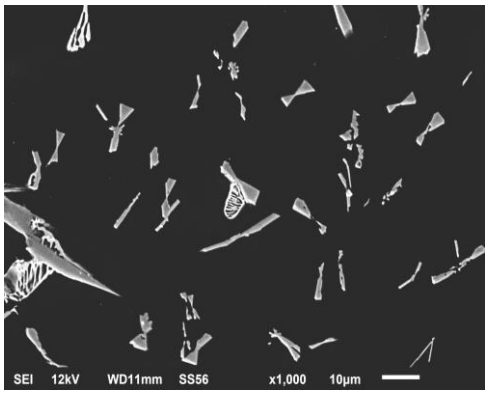

B 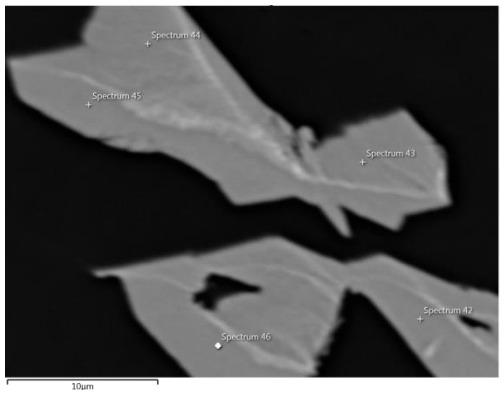

Figure 6.54 (A) SEM images of TC8 of Alloy 4 (B) Magnified EDS image used for Elemental analysis

Table 6.23 Elemental composition of intermetallics marked on Figure 6.54 B

Phase # as marked in the image	Al		Fe		
	wt%	at%	wt%	at%	phase
1	61	77	35	22	$FeAl_3$
2	62	77	36	22	$FeAl_3$
3	62	77	35	22	$FeAl_3$
4	61	77	35	22	$FeAl_3$
5	62	77	35	22	$FeAl_3$

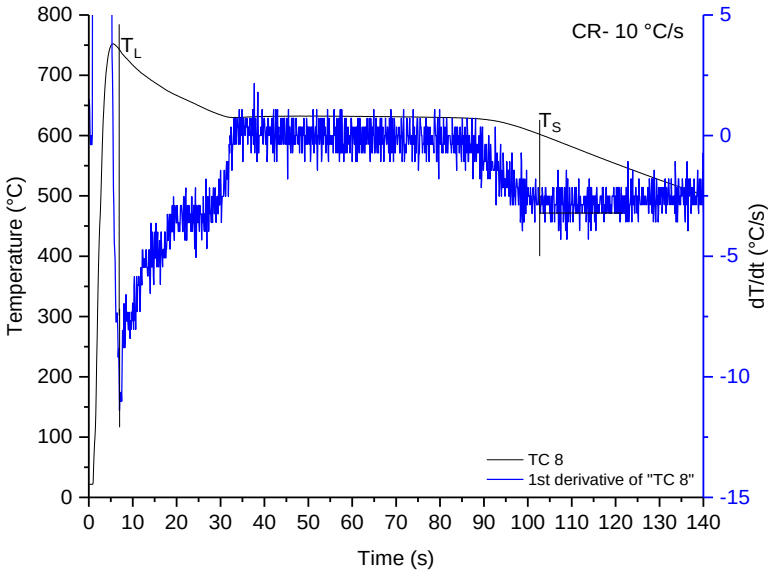

Figure 6.55 Cooling curve and the associated dT/dt curve for TC8 location

A 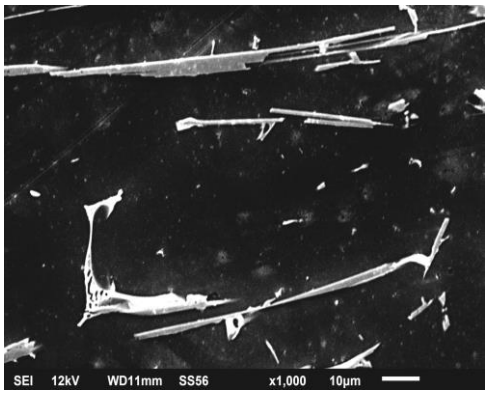

B 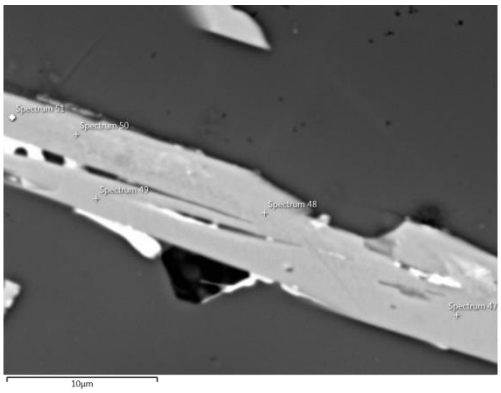

Figure 6.56 (A) SEM images of TC8 of Alloy 4 (B) Magnified EDS image used for Elemental analysis

Table 6.24 Elemental composition of intermetallics marked on Figure 6.56 B

Phase # as marked in the image	Al		Fe		
	wt%	at%	wt%	at%	phase
1	62	77	36	22	$FeAl_3$
2	61	77	36	22	$FeAl_3$
3	60	76	35	21	$FeAl_6$
4	61	77	35	22	$FeAl_3$
5	61	76	36	22	$FeAl_3$

Alloy 5

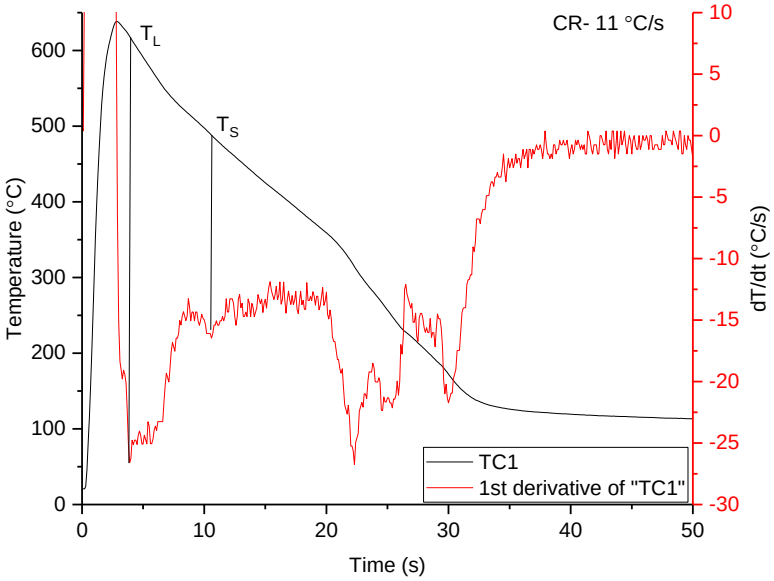

Figure 6.57 Cooling curve and the associated dT/dt curve for TC1 location

A 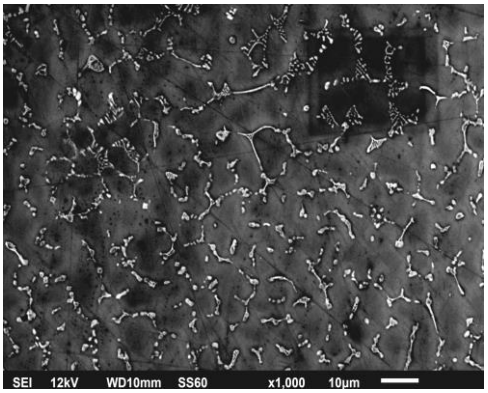

B 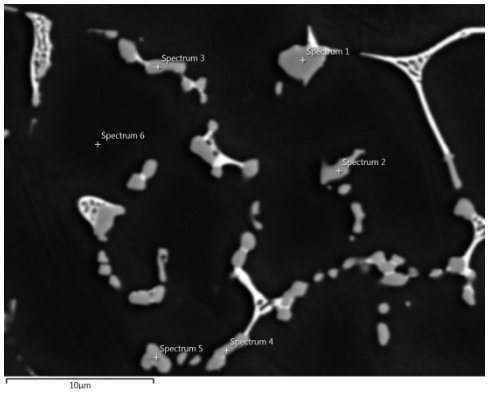

Figure 6.58 (A) SEM images of TC1 of Alloy 5 (B) Magnified EDS image used for Elemental analysis

Table 6.25 Elemental composition of intermetallics marked on Figure 6.58 B

Phase # as marked in the image	Al		Fe		
	wt%	at%	wt%	at%	phase
1	66	80	23	14	$FeAl_6$
2	68	82	21	12	$FeAl_6$
3	67	81	21	12	$FeAl_6$
4	67	81	16	10	$FeAl_6$
5	66	80	19	11	$FeAl_6$

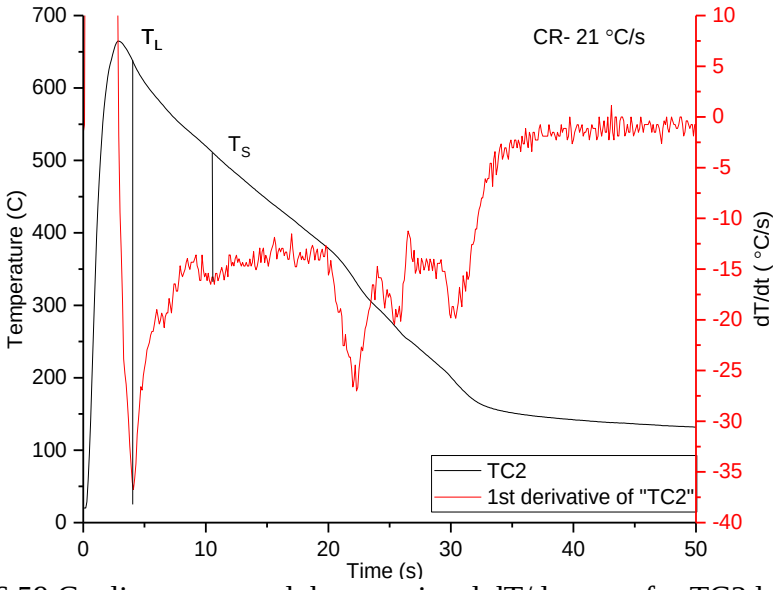

Figure 6.59 Cooling curve and the associated dT/dt curve for TC2 location

A 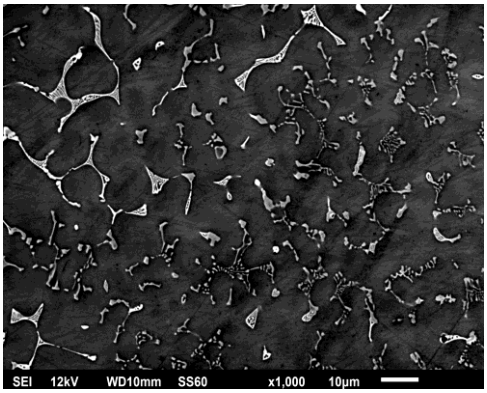

B 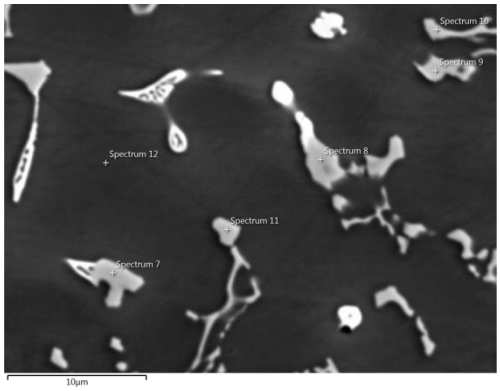

Figure 6.60 (A) SEM images of TC2 of Alloy 5 (B) Magnified EDS image used for Elemental analysis

Table 6.26 Elemental composition of intermetallics marked on Figure 6.60 B

Phase # as marked in the image	Al		Fe		
	wt%	at%	wt%	at%	phase
1	62	78	30	18	$FeAl_3$
2	65	80	26	15	$FeAl_6$
3	61	77	27	17	$FeAl_6$
4	66	80	25	15	$FeAl_6$
5	64	79	28	16	$FeAl_6$

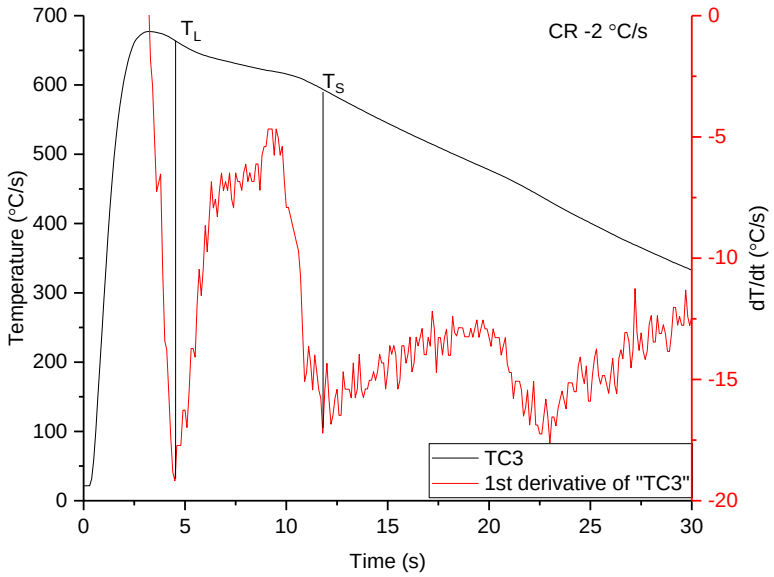

Figure 6.61 Cooling curve and the associated dT/dt curve for TC3 location

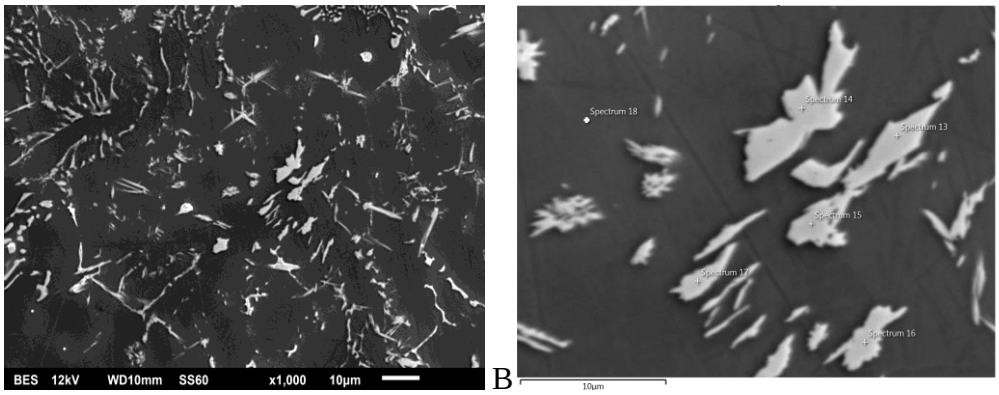

A B

Figure 6.62 (A) SEM images of TC3 of Alloy 5 (B) Magnified EDS image used for Elemental analysis

Table 6.27Elemental composition of intermetallics marked on Figure 6.62 B

Phase # as marked in the image	Al		Fe		
	wt%	at%	wt%	at%	phase
1	61	77	35	21	$FeAl_3$
2	62	77	34	21	$FeAl_3$
3	62	77	34	21	$FeAl_3$
4	62	77	34	21	$FeAl_3$
5	62	77	34	20	$FeAl_3$

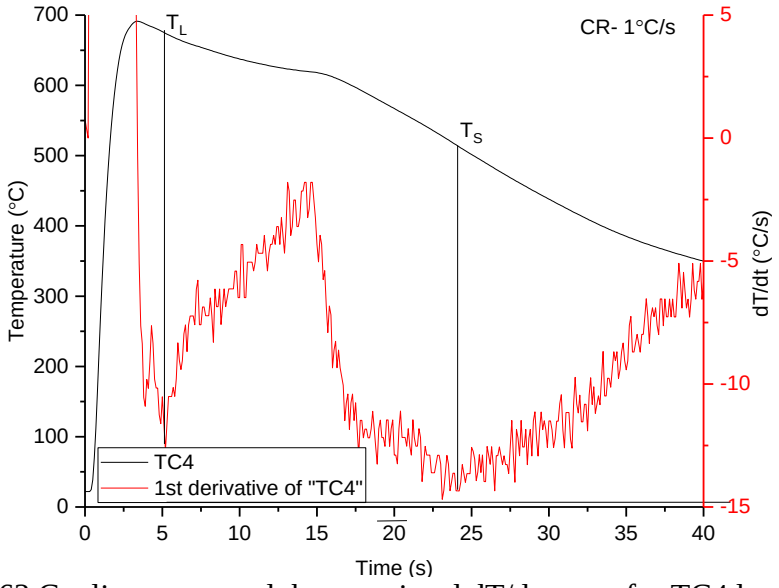

Figure 6.63 Cooling curve and the associated dT/dt curve for TC4 location

A 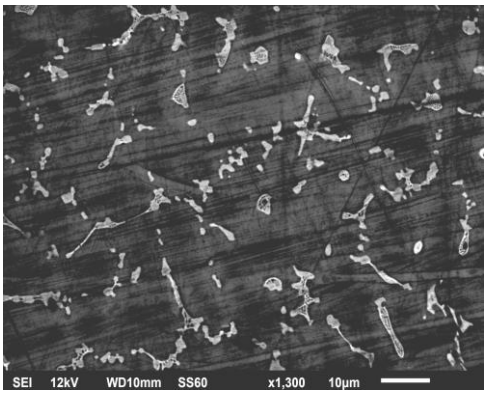

B 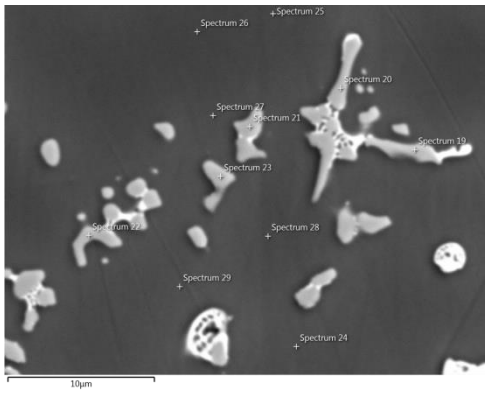

Figure 6.64 (A) SEM images of TC4 of Alloy 5 (B) Magnified EDS image used for Elemental analysis

Table 6.28 Elemental composition of intermetallics marked on Figure 6.64 B

Phase # as marked in the image	Al		Fe		
	wt%	at%	wt%	at%	phase
1	67	82	21	12	$FeAl_6$
2	67	81	21	12	$FeAl_6$
3	67	81	21	12	$FeAl_6$
4	67	81	21	12	$FeAl_6$
5	66	81	22	13	$FeAl_6$

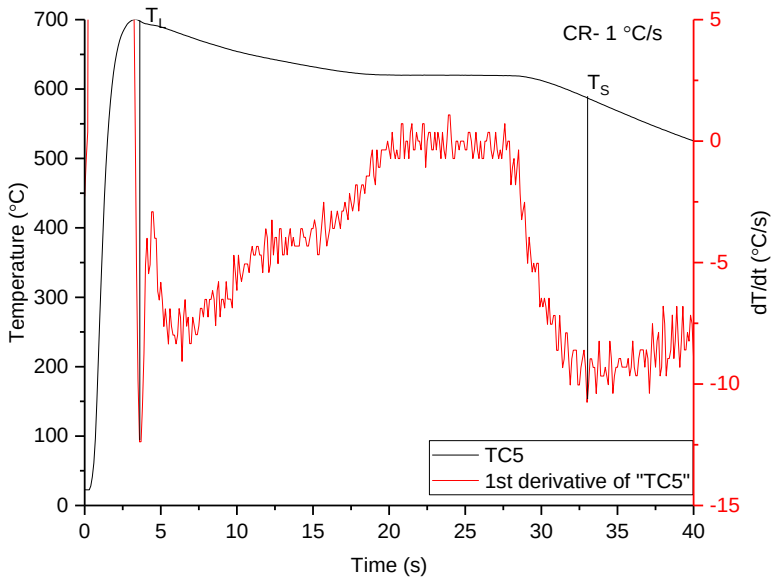

Figure 6.65 Cooling curve and the associated dT/dt curve for TC5 location

A 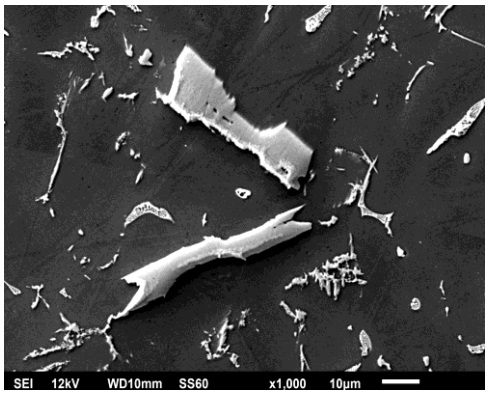

B 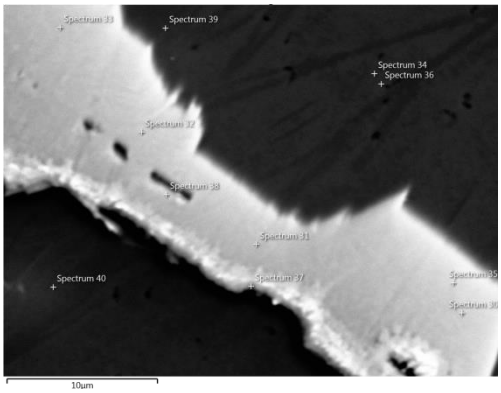

Figure 6.66 (A) SEM images of TC5 of Alloy 5 (B) Magnified EDS image used for Elemental analysis

Table 6.29 Elemental composition of intermetallics marked on Figure 6.66 B

Phase # as marked in the image	Al		Fe		
	wt%	at%	wt%	at%	phase
1	62	77	36	22	$FeAl_3$
2	61	77	36	22	$FeAl_3$
3	61	77	36	22	$FeAl_3$
4	62	77	35	21	$FeAl_3$
5	62	77	35	21	$FeAl_3$

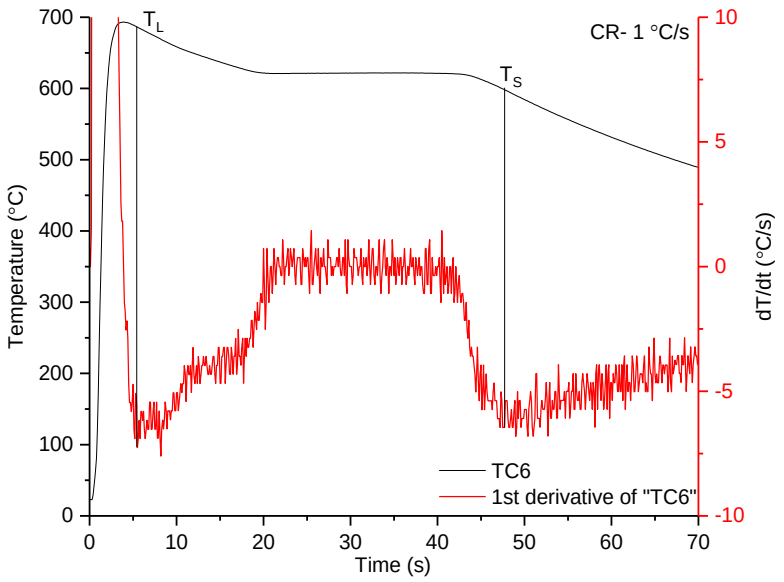

Figure 6.67 Cooling curve and the associated dT/dt curve for TC6 location

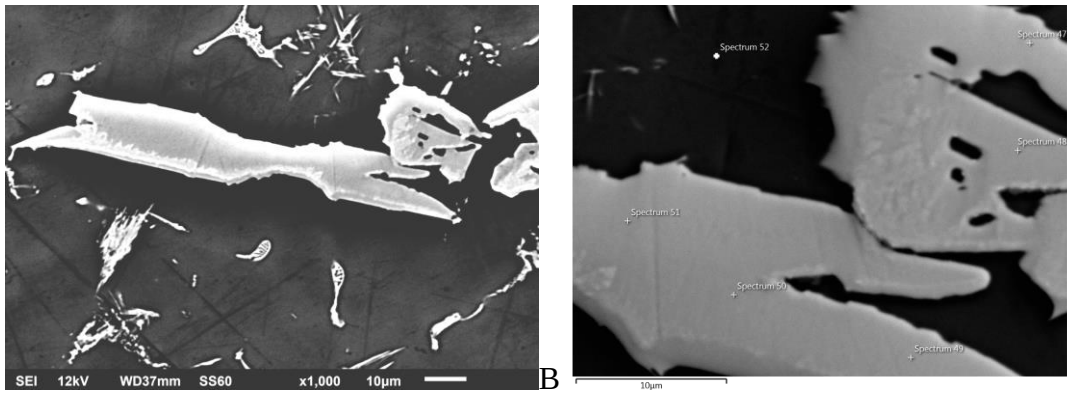

A B

Figure 6.68 (A) SEM images of TC6 of Alloy 5 (B) Magnified EDS image used for Elemental analysis

Table 6.30 Elemental composition of intermetallics marked on Figure 6.68 B

Phase # as marked in the image	Al		Fe		
	wt%	at%	wt%	at%	phase
1	60	76	37	23	$FeAl_3$
2	61	76	37	22	$FeAl_3$
3	61	76	37	22	$FeAl_3$
4	66	76	37	23	$FeAl_3$
5	60	76	37	23	$FeAl_3$

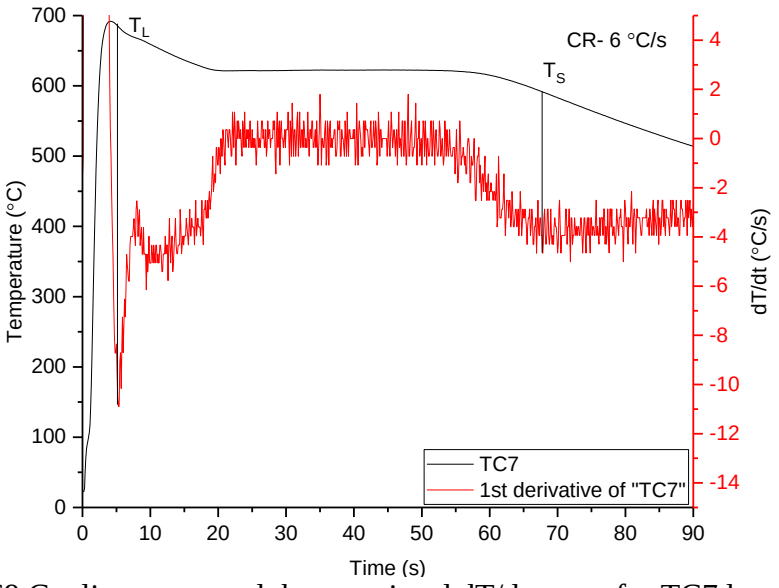

Figure 6.69 Cooling curve and the associated dT/dt curve for TC7 location

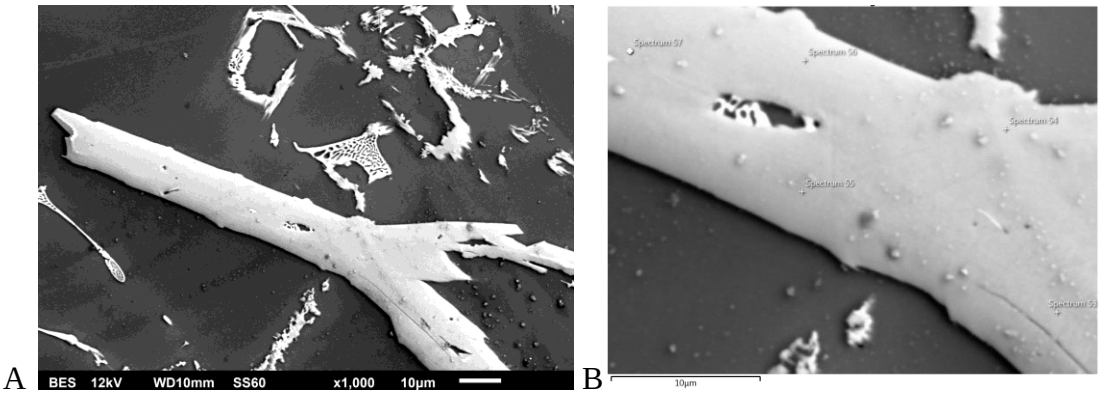

A B

Figure 6.70 (A) SEM images of TC7 of Alloy 5 (B) Magnified EDS image used for Elemental analysis

Table 6.31 Elemental composition of intermetallics marked on Figure 6.70 B

Phase # as marked in the image	Al		Fe		
	wt%	at%	wt%	at%	phase
1	61	77	37	22	$FeAl_3$
2	60	76	37	22	$FeAl_3$
3	61	77	36	22	$FeAl_3$
4	60	76	37	23	$FeAl_3$
5	60	76	38	23	$FeAl_3$

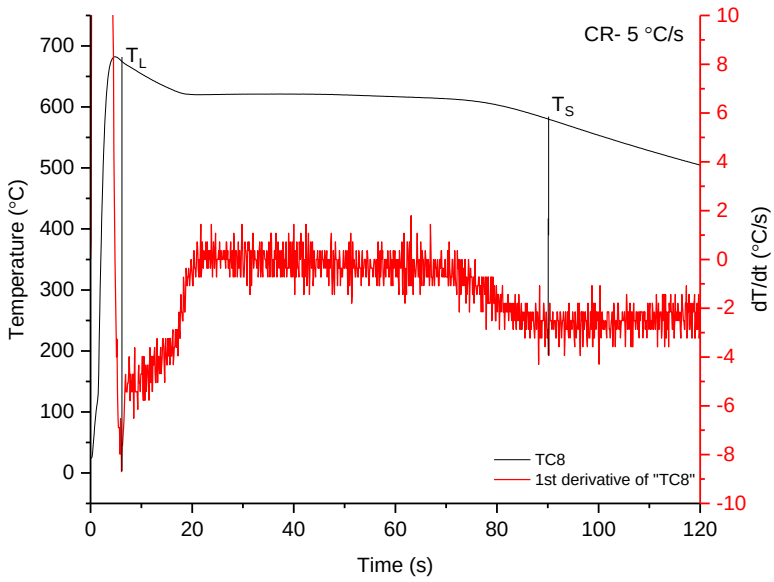

Figure 6.71 Cooling curve and the associated dT/dt curve for TC8 location

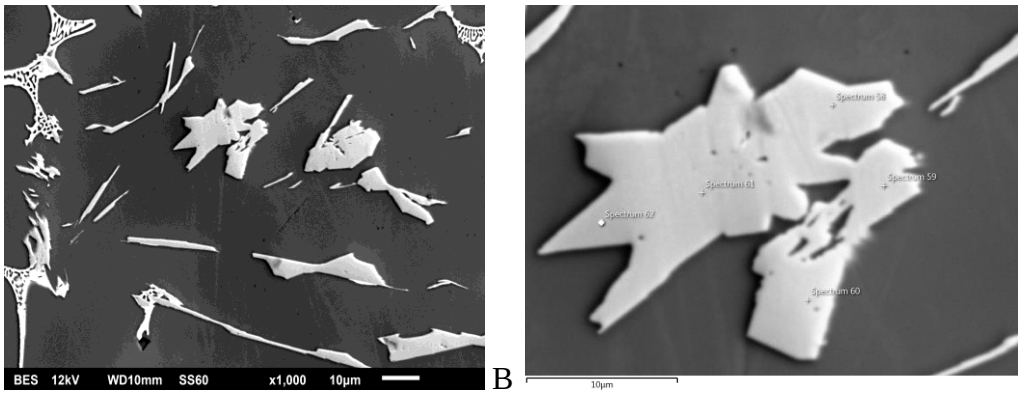

A B

Figure 6.72 (A) SEM images of TC8 of Alloy 5 (B) Magnified EDS image used for Elemental analysis

Table 6.32 Elemental composition of intermetallics marked on Figure 6.72 B

Phase # as marked in the image	Al		Fe		
	wt%	at%	wt%	at%	phase
1	60	76	37	22	$FeAl_3$
2	61	77	35	21	$FeAl_3$
3	60	77	36	22	$FeAl_3$
4	61	77	36	22	$FeAl_3$
5	61	77	35	21	$FeAl_3$

Alloy6

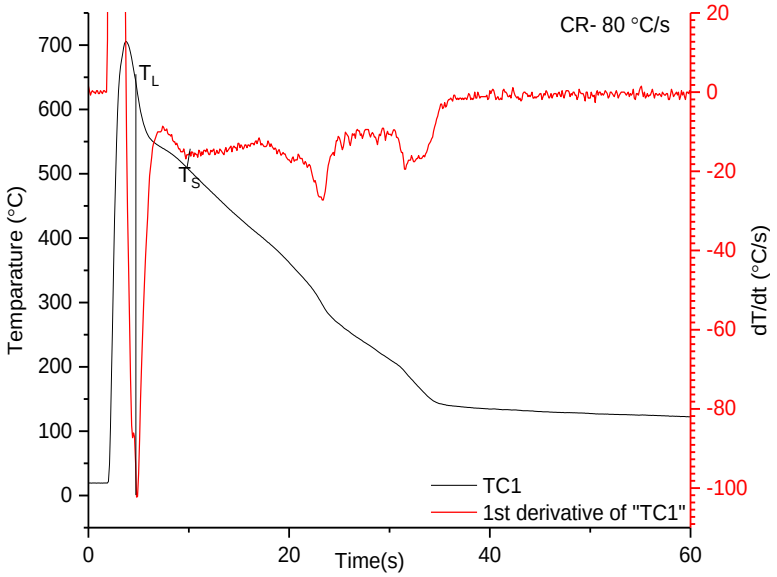

Figure 6.73 Cooling curve and the associated dT/dt curve for TC1 location

A 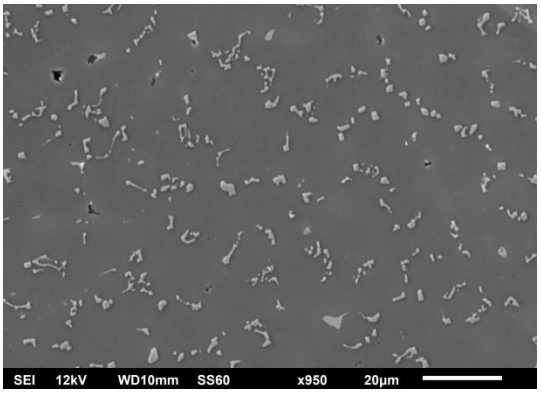

B 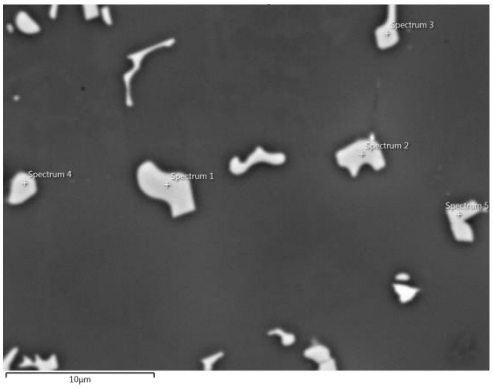

Figure 6.74 (A) SEM images of TC1 of Alloy 6 (B) Magnified EDS image used for Elemental analysis

Table 6.33 Elemental composition of intermetallics marked on Figure 6.74 B

Phase # as marked in the image	Al		Fe		
	wt%	at%	wt%	at%	phase
1	69	82	24	14	$FeAl_6$
2	68	82	24	14	$FeAl_6$
3	70	83	23	13	$FeAl_6$
4	69	84	23	13	$FeAl_6$
5	69	82	23	13	$FeAl_6$

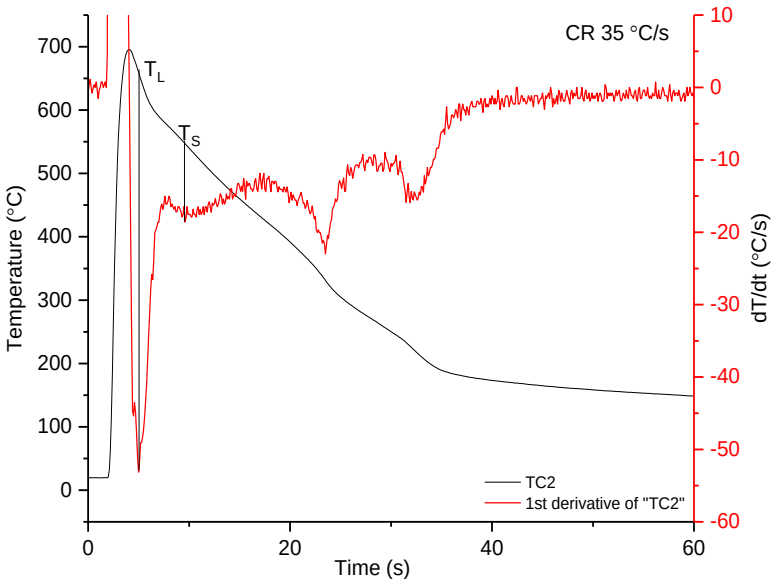

Figure 6.75 Cooling curve and the associated dT/dt curve for TC2 location

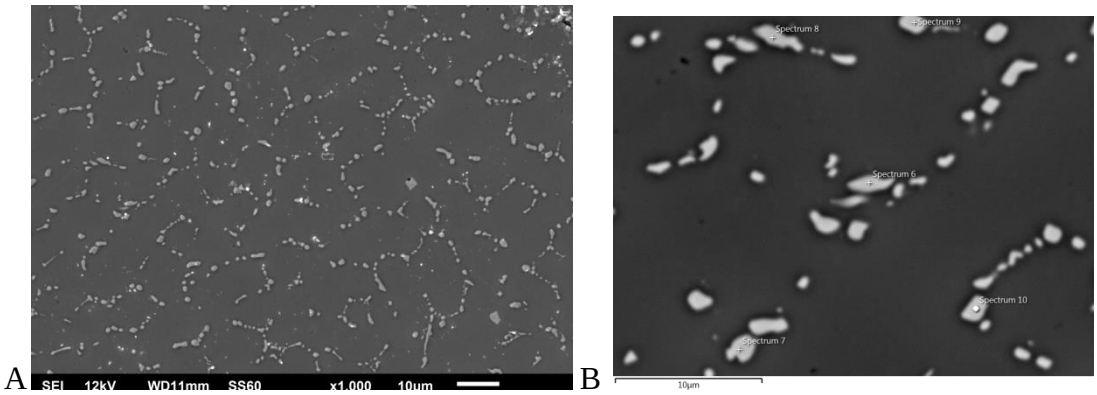

Figure 6.76 (A) SEM images of TC2 of Alloy 6 (B) Magnified EDS image used for Elemental analysis

Table 6.34 Elemental composition of intermetallics marked on Figure 6.76 B

Phase # as marked in the image	Al		Fe		
	wt%	at%	wt%	at%	phase
1	70	83	21	12	$FeAl_6$
2	70	83	21	12	$FeAl_6$
3	75	86	18	10	$FeAl_6$
4	70	83	21	12	$FeAl_6$
5	69	82	22	13	$FeAl_6$

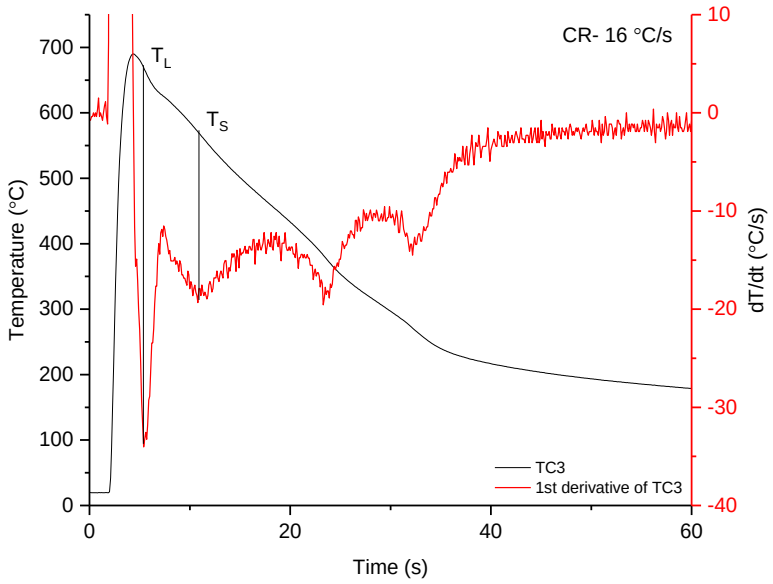

Figure 6.77 Cooling curve and the associated dT/dt curve for TC3 location

A 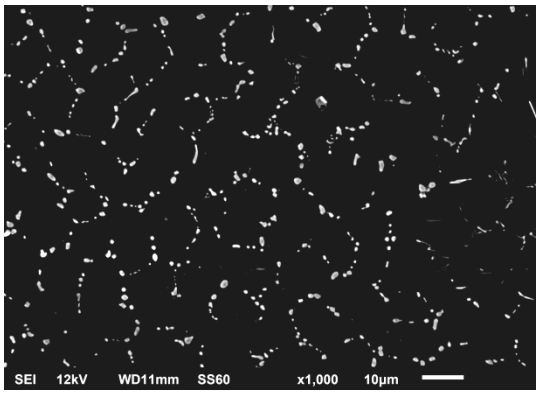

B 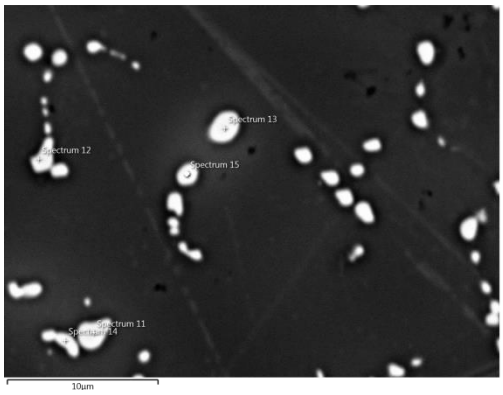

Figure 6.78 (A) SEM images of TC3 of Alloy 6 (B) Magnified EDS image used for Elemental analysis

Table 6.35 Elemental composition of intermetallics marked on Figure 6.78 B

Phase # as marked in the image	Al		Fe		
	wt%	at%	wt%	at%	phase
1	69	82	23	13	$FeAl_6$
2	73	85	19	11	$FeAl_6$
3	68	82	23	13	$FeAl_6$
4	70	83	21	12	$FeAl_6$
5	69	83	22	12	$FeAl_6$

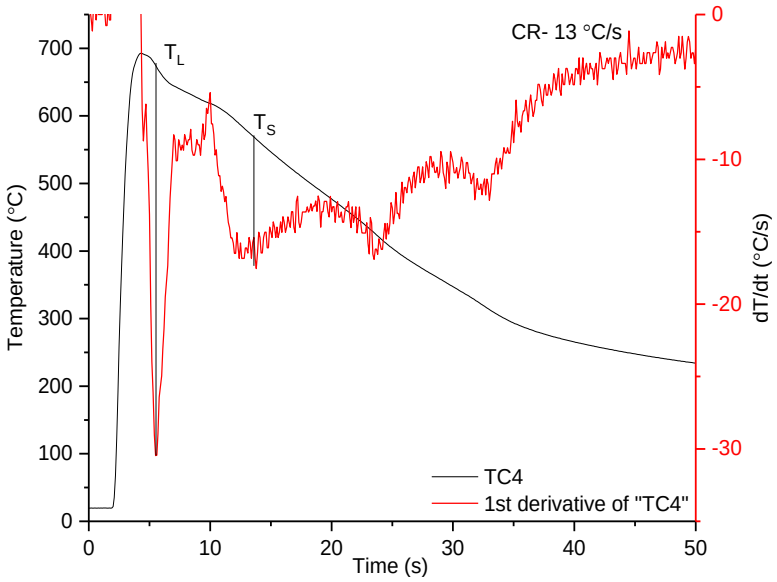

Figure 6.79 Cooling curve and the associated dT/dt curve for TC4 location

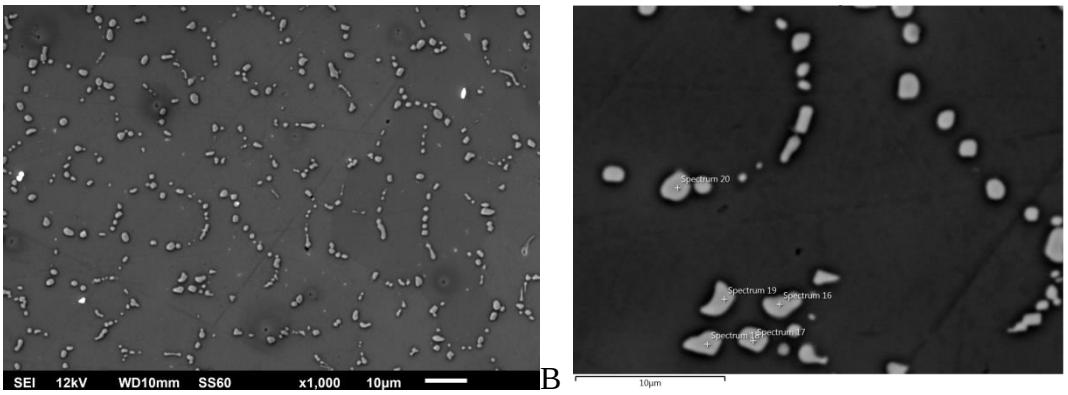

A B

Figure 6.80 (A) SEM images of TC4 of Alloy 6 (B) Magnified EDS image used for
Elemental analysis

Table 6.36 Elemental composition of intermetallics marked on Figure 6.80 B

Phase # as marked in the image	Al		Fe		
	wt%	at%	wt%	at%	phase
1	70	83	21	12	$FeAl_6$
2	68	82	23	13	$FeAl_6$
3	68	82	23	14	$FeAl_6$
4	69	82	23	13	$FeAl_6$
5	68	82	23	13	$FeAl_6$

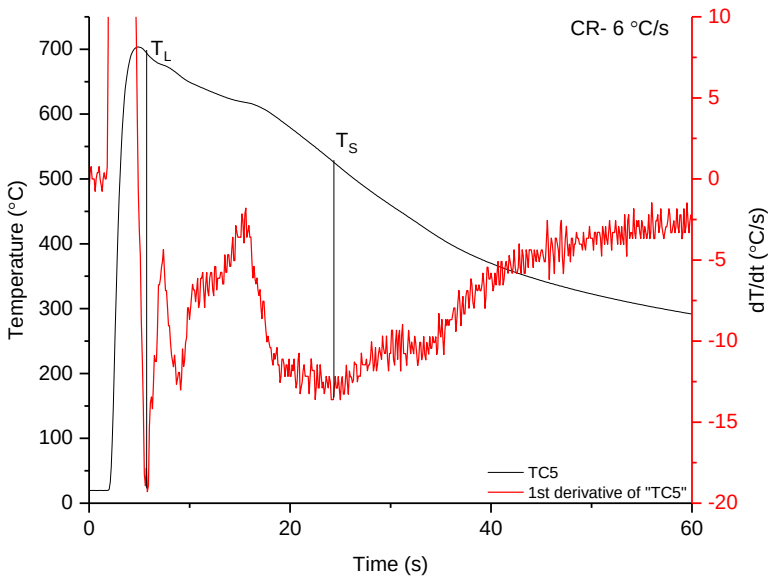

Figure 6.87 Cooling curve and the associated dT/dt curve for TC5 location

A 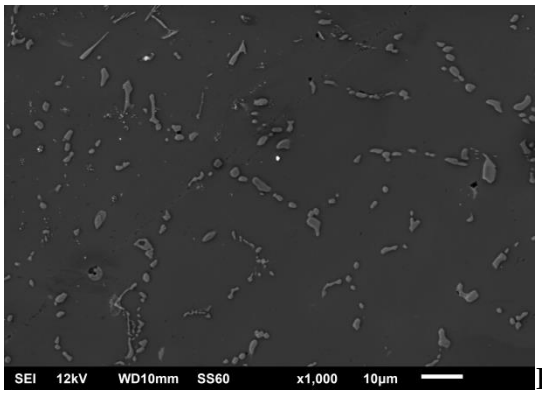

B 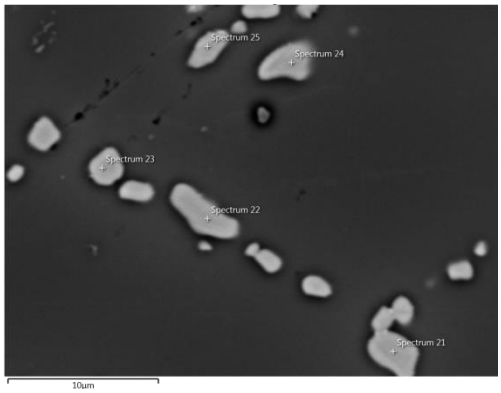

Figure 6.88 (A) SEM images of TC5 of Alloy 6 (B) Magnified EDS image used for Elemental analysis

Table 6.37 Elemental composition of intermetallics marked on Figure 6.88 B

Phase # as marked in the image	Al		Fe		
	wt%	at%	wt%	at%	phase
1	67	81	24	14	$FeAl_6$
2	68	82	24	14	$FeAl_6$
3	68	82	24	14	$FeAl_6$
4	68	82	24	14	$FeAl_6$
5	68	82	24	14	$FeAl_6$

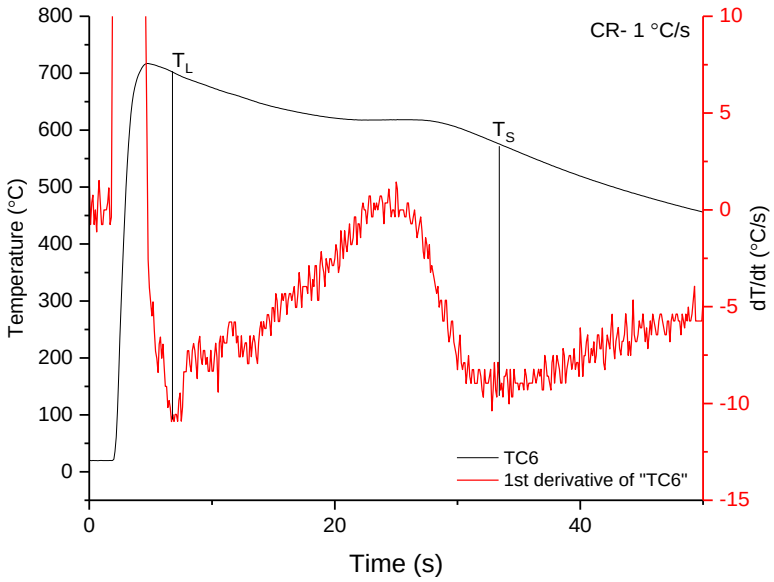

Figure 6.89 Cooling curve and the associated dT/dt curve for TC6 location

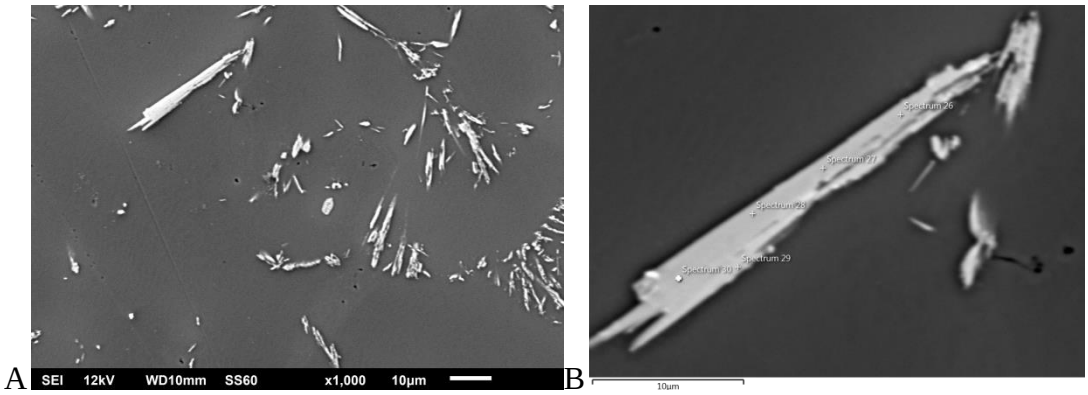

Figure 6.90 (A) SEM images of TC6 of Alloy 6 (B) Magnified EDS image used for Elemental analysis

Table 6.38 Elemental composition of intermetallics marked on Figure 6.90 B

Phase # as marked in the image	Al		Fe		
	wt%	at%	wt%	at%	phase
1	62	77	36	21	$FeAl_6$
2	63	78	32	19	$FeAl_6$
3	63	77	33	20	$FeAl_6$
4	62	76	28	17	$FeAl_6$
5	61	76	33	20	$FeAl_6$

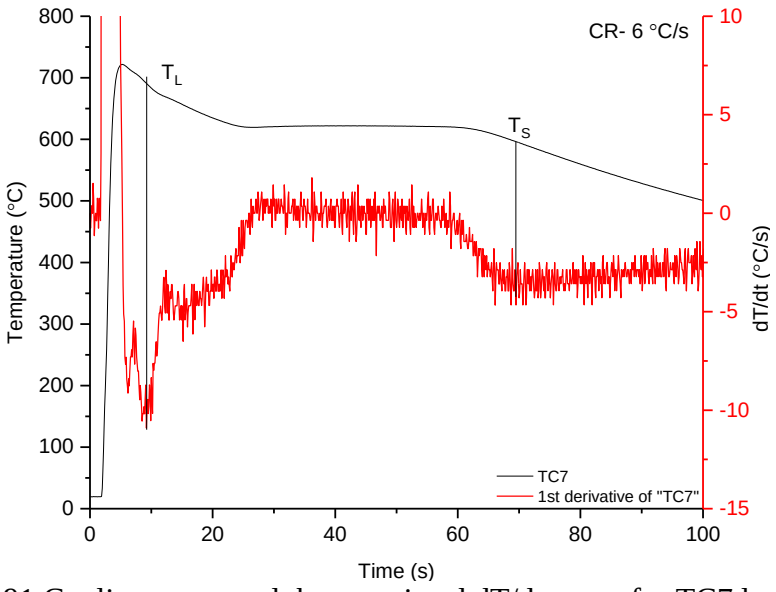

Figure 6.91 Cooling curve and the associated dT/dt curve for TC7 location

A 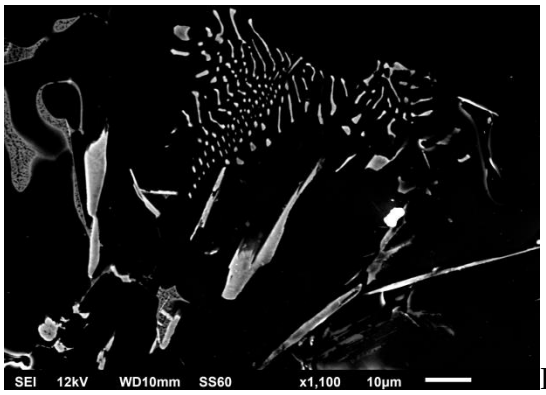

B 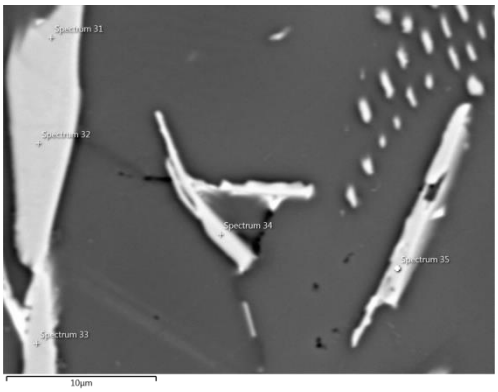

Figure 6.92 (A) SEM images of TC7 of Alloy 6 (B) Magnified EDS image used for Elemental analysis

Table 6.39 Elemental composition of intermetallics marked on Figure 6.92 B

Phase # as marked in the image	Al		Fe		
	wt%	at%	wt%	at%	phase
1	62	77	37	22	$FeAl_3$
2	62	77	36	22	$FeAl_3$
3	61	76	35	21	$FeAl_3$
4	63	77	34	20	$FeAl_3$
5	63	78	34	20	$FeAl_3$

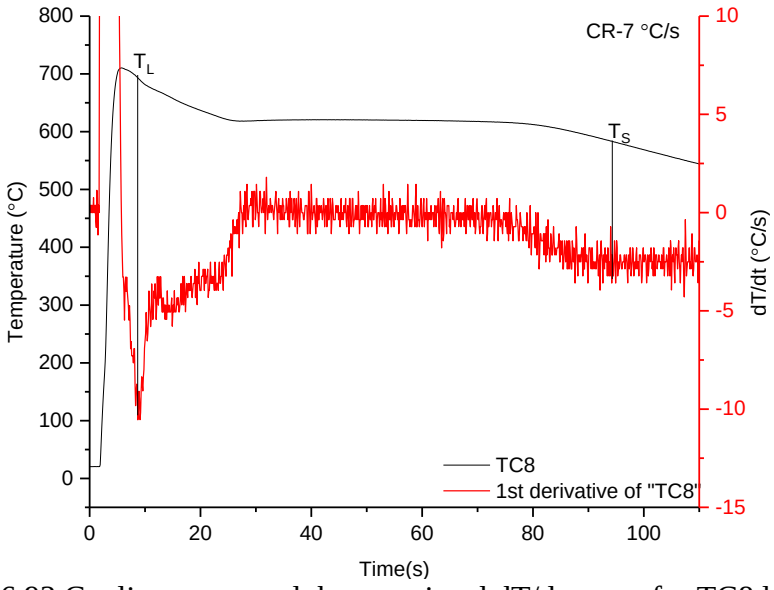

Figure 6.93 Cooling curve and the associated dT/dt curve for TC8 location

A 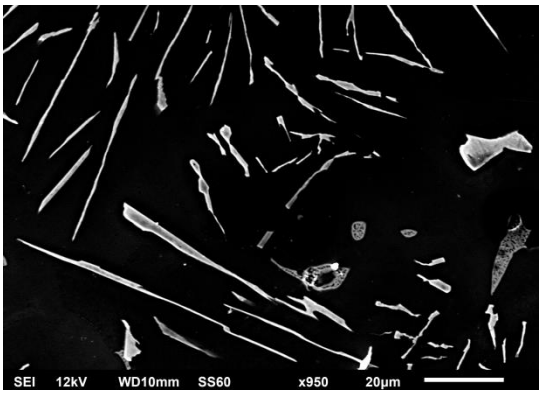

B 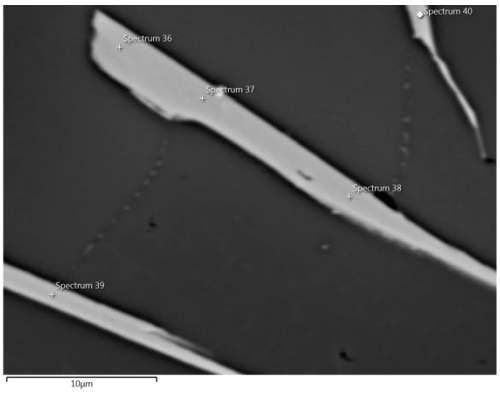

Figure 6.94 (A) SEM images of TC8 of Alloy 6 (B) Magnified EDS image used for Elemental analysis

Table 6.40 Elemental composition of intermetallics marked on Figure 6.94 B

Phase # as marked in the image	Al		Fe		
	wt%	at%	wt%	at%	phase
1	61	77	37	23	$FeAl_6$
2	60	76	39	24	$FeAl_6$
3	61	76	38	23	$FeAl_6$
4	62	73	37	22	$FeAl_6$
5	63	78	36	22	$FeAl_6$

Alloy 7

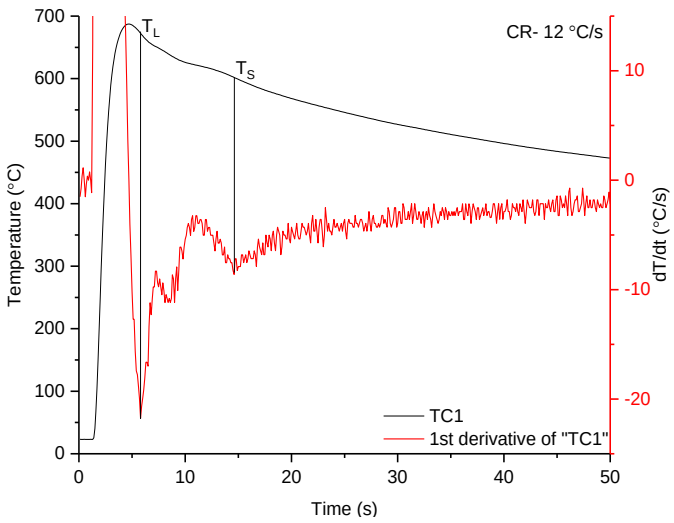

Figure 6.95 Cooling curve and the associated dT/dt curve forTC1 location

A 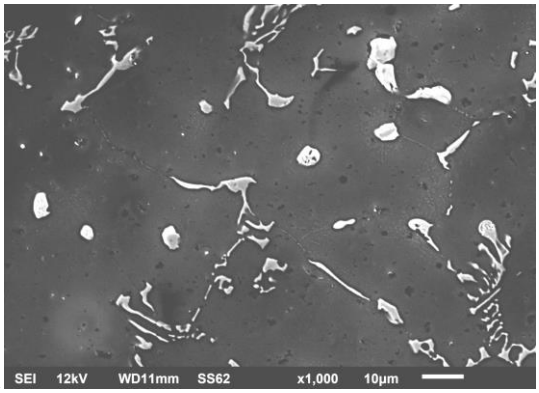

B 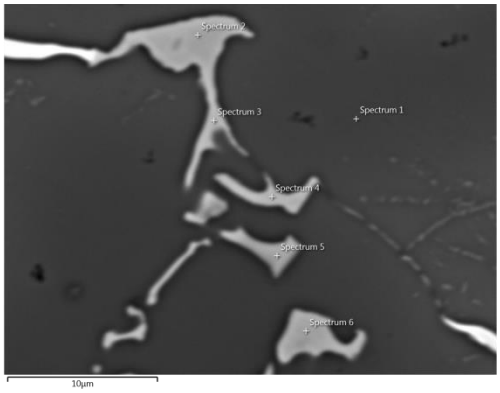

Figure 6.96 (A) SEM images of TC1 of Alloy 7 (B) Magnified EDS image used for
Elemental analysis

Table 6.41 Elemental composition of intermetallics marked on Figure 6.96 B

Phase # as marked in the image	Al		Fe		
	wt%	at%	wt%	at%	phase
1	61	77	30	18	$FeAl_6$
2	61	77	26	16	$FeAl_6$
3	61	77	27	17	$FeAl_6$
4	67	81	23	14	$FeAl_6$
5	64	79	27	16	$FeAl_6$

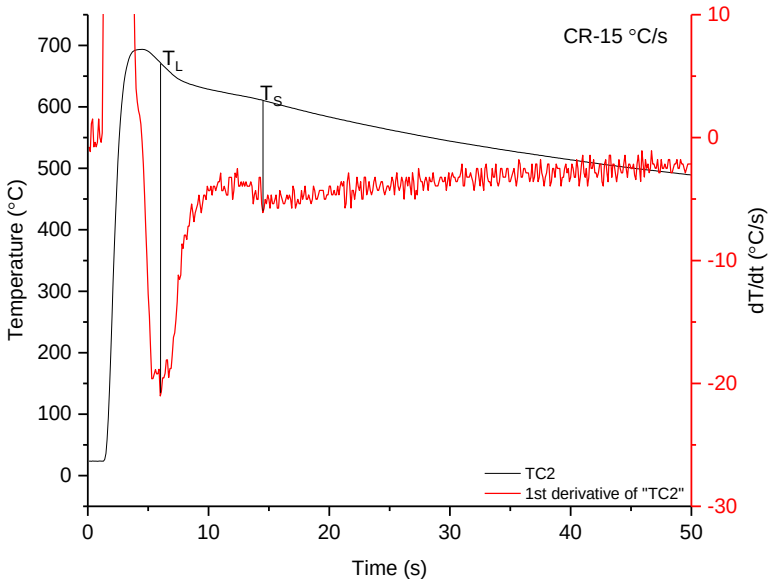

Figure 6.97 Cooling curve and the associated dT/dt curve for TC2 location

A 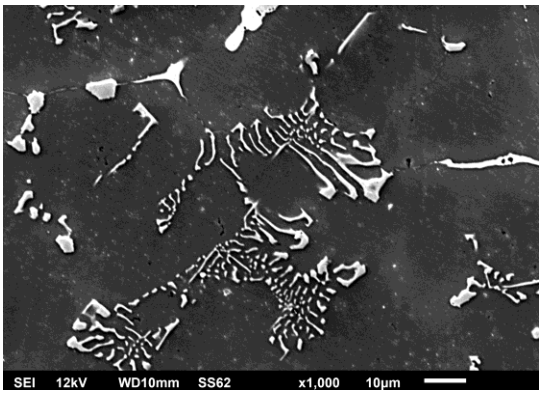

B 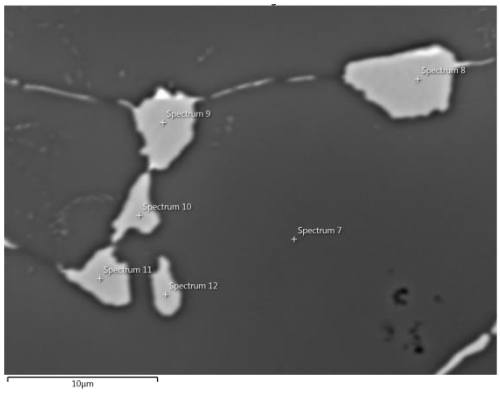

Figure 6.98 (A) SEM images of TC2 of Alloy 7 (B) Magnified EDS image used for Elemental analysis

Table 6.42 Elemental composition of intermetallics marked on Figure 6.98 B

Phase # as marked in the image	Al		Fe		
	wt%	at%	wt%	at%	phase
1	62	77	29	18	$FeAl_3$
2	62	77	29	17	$FeAl_3$
3	62	77	29	18	$FeAl_3$
4	62	77	29	18	$FeAl_3$
5	62	77	29	18	$FeAl_3$

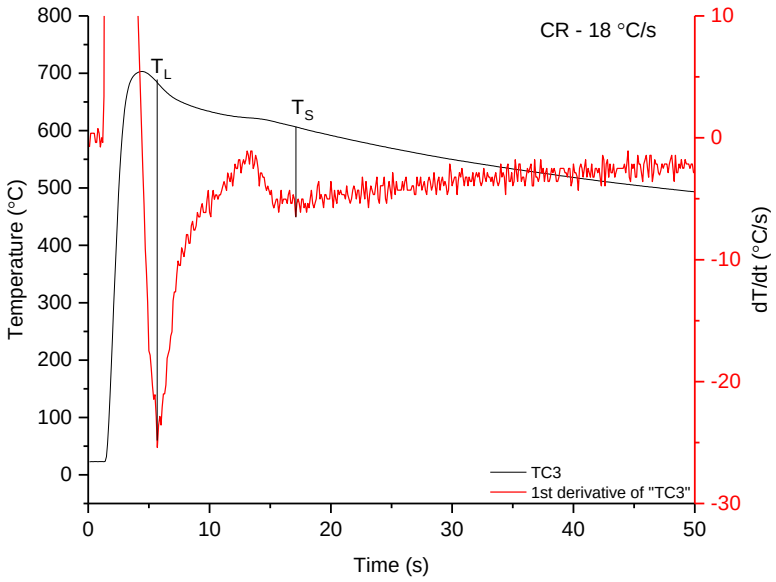

Figure 6.99 Cooling curve and the associated dT/dt curve for TC3 location

A 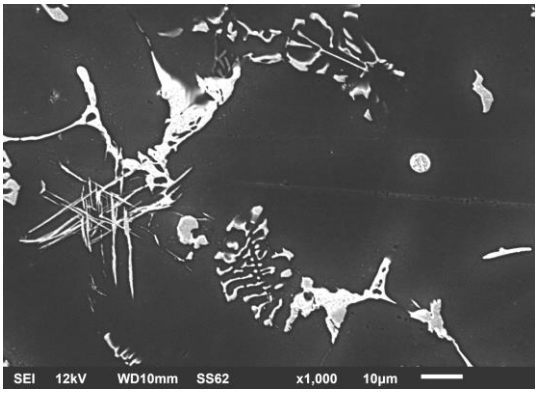

B 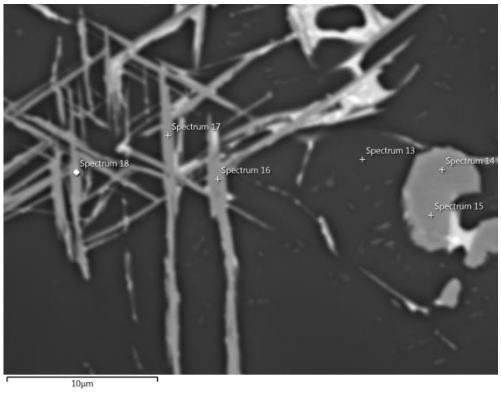

Figure 6.100 (A) SEM images of TC3 of Alloy 7 (B) Magnified EDS image used for Elemental analysis

Table 6.43 Elemental composition of intermetallics marked on Figure 6.100 B

Phase # as marked in the image	Al		Fe		
	wt%	at%	wt%	at%	phase
1	60	76	30	18	$FeAl_6$
2	60	76	29	18	$FeAl_6$
3	59	75	28	17	$FeAl_6$
4	64	79	27	16	$FeAl_6$
5	61	77	30	18	$FeAl_6$

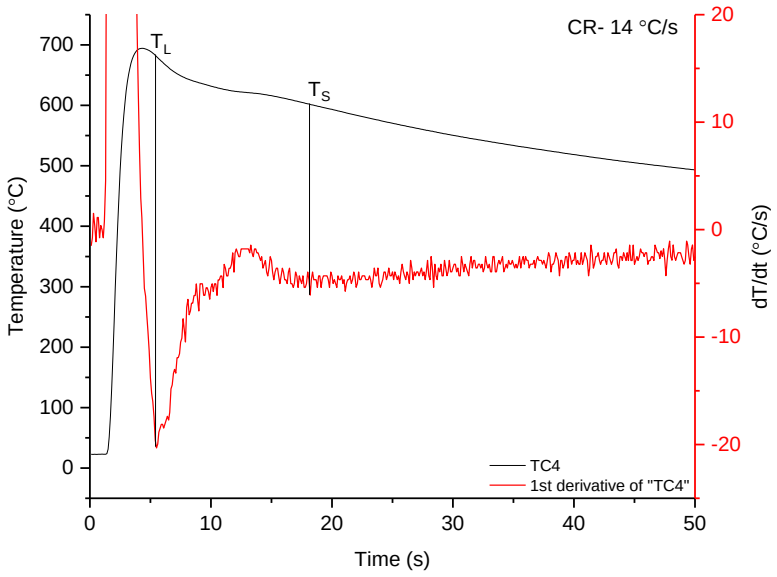

Figure 6.101 Cooling curve and the associated dT/dt curve for TC8 location

A 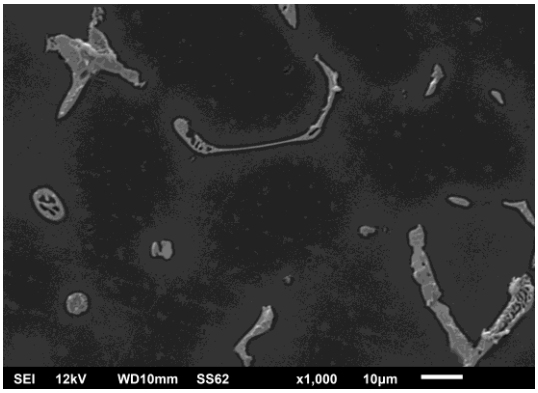

B 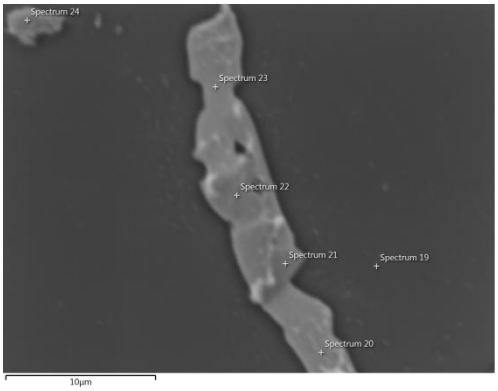

Figure 6.102 (A) SEM images of TC4 of Alloy 7 (B) Magnified EDS image used for Elemental analysis

Table 6.44 Elemental composition of intermetallics marked on Figure 6.102 B

Phase # as marked in the image	Al		Fe		
	wt%	at%	wt%	at%	phase
1	60	76	30	18	$FeAl_6$
2	62	77	29	18	$FeAl_6$
3	61	77	30	18	$FeAl_6$
4	60	76	29	18	$FeAl_6$
5	61	77	30	18	$FeAl_6$

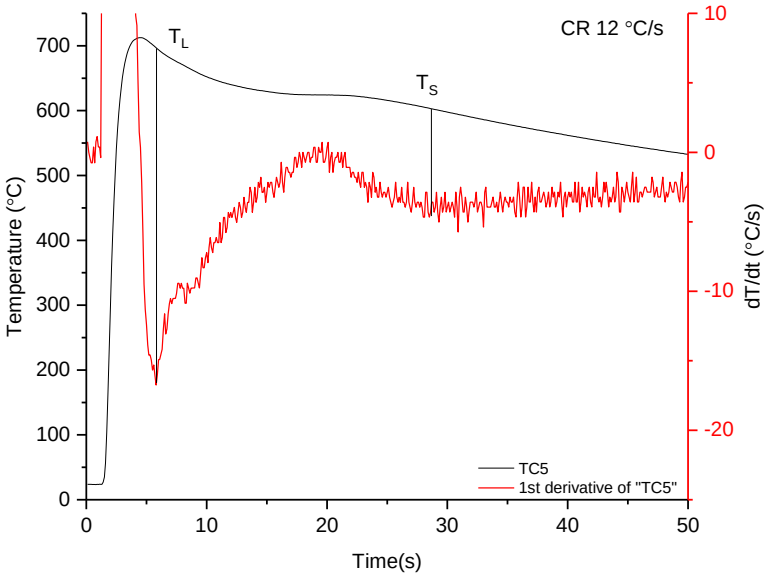

Figure 6.103 Cooling curve and the associated dT/dt curve for TC5 location

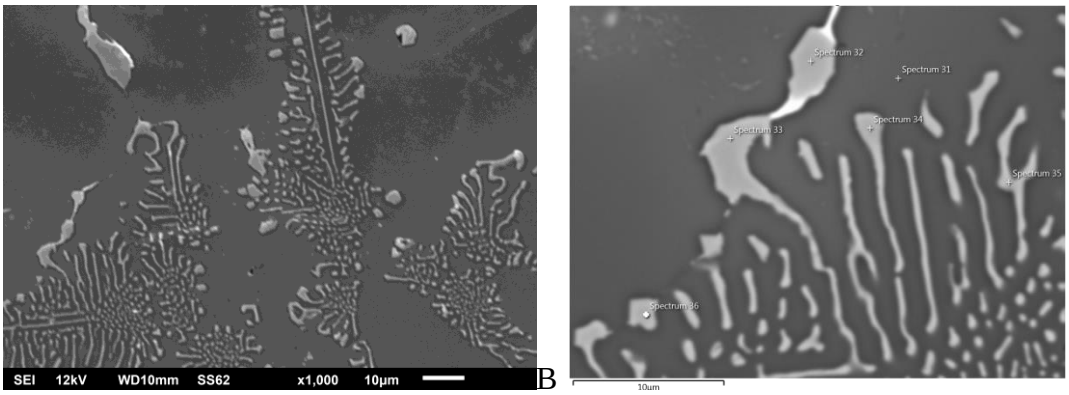

A B

Figure 6.104 (A) SEM images of TC5 of Alloy 7 (B) Magnified EDS image used for Elemental analysis

Table 6.45 Elemental composition of intermetallics marked on Figure 6.104 B

Phase # as marked in the image	Al		Fe		
	wt%	at%	wt%	at%	phase
1	60	76	28	17	$FeAl_6$
2	61	77	28	18	$FeAl_6$
3	66	81	24	14	$FeAl_6$
4	69	83	21	12	$FeAl_6$
5	62	78	28	17	$FeAl_6$

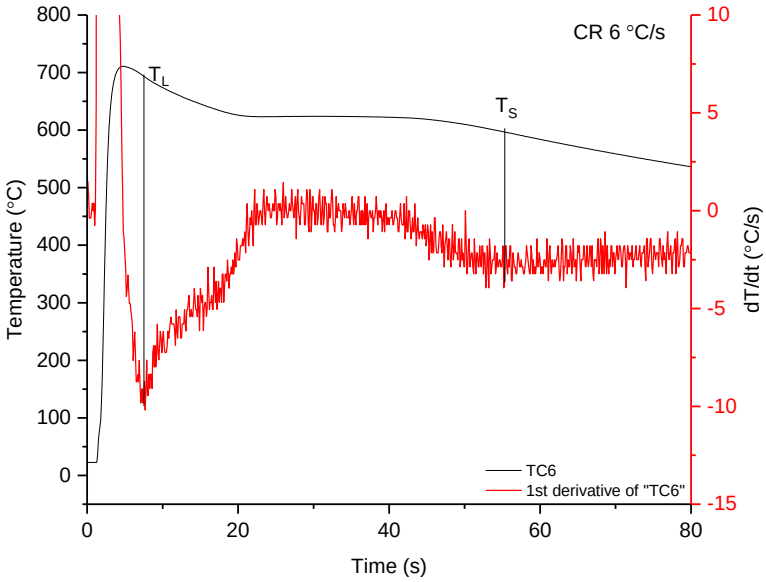

Figure 6.105 Cooling curve and the associated dT/dt curve for TC6 location

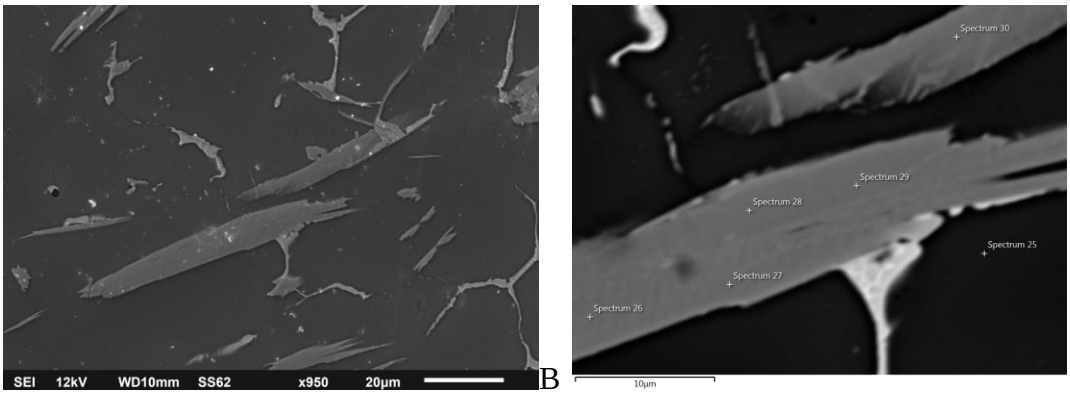

A B

Figure 6.106 (A) SEM images of TC6 of Alloy 7 (B) Magnified EDS image used for Elemental analysis

Table 6.46 Elemental composition of intermetallics marked on Figure 6.106 B

Phase # as marked in the image	Al		Fe		
	wt%	at%	wt%	at%	phase
1	62	77	34	21	$FeAl_3$
2	61	76	34	21	$FeAl_3$
3	61	76	35	21	$FeAl_3$
4	61	77	35	21	$FeAl_3$
5	66	80	27	16	$FeAl_6$

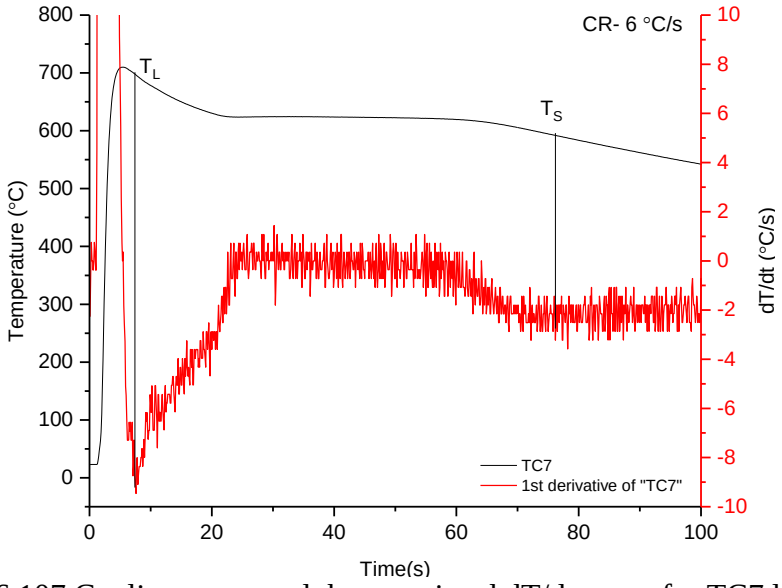

Figure 6.107 Cooling curve and the associated dT/dt curve for TC7 location

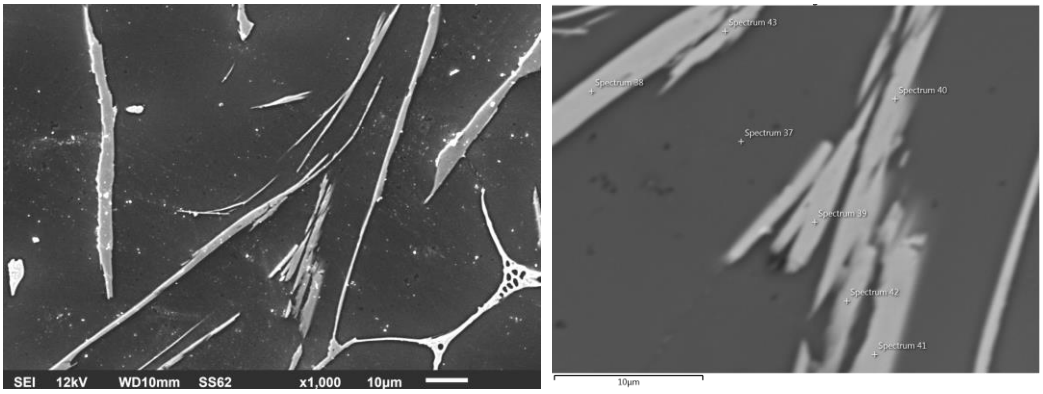

Figure 6.108 (A) SEM images of TC7 of Alloy 7 (B) Magnified EDS image used for Elemental analysis

Table 6.47 Elemental composition of intermetallics marked on Figure 6.108 B

Phase # as marked in the image	Al		Fe		
	wt%	at%	wt%	at%	phase
1	62	77	34	21	$FeAl_3$
2	61	76	36	22	$FeAl_3$
3	61	77	33	21	$FeAl_3$
4	63	78	32	20	$FeAl_3$
5	67	81	27	16	$FeAl_6$

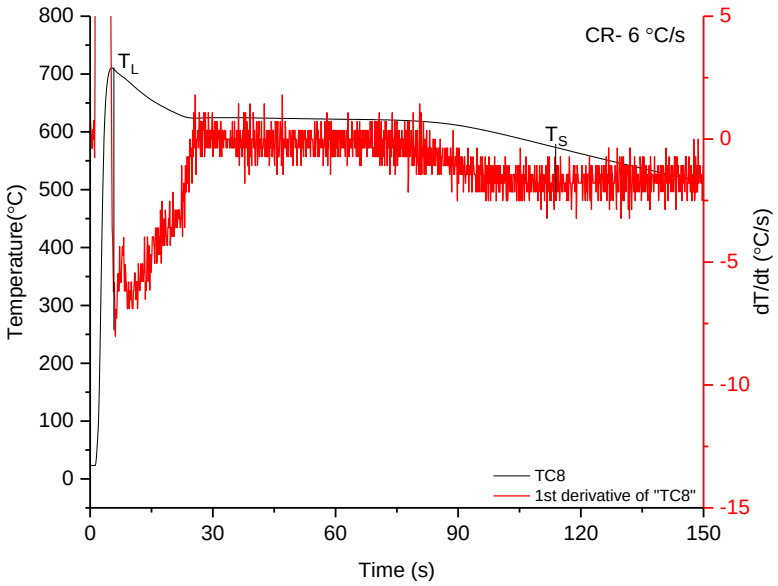

Figure 6.109 Cooling curve and the associated dT/dt curve for TC8 location

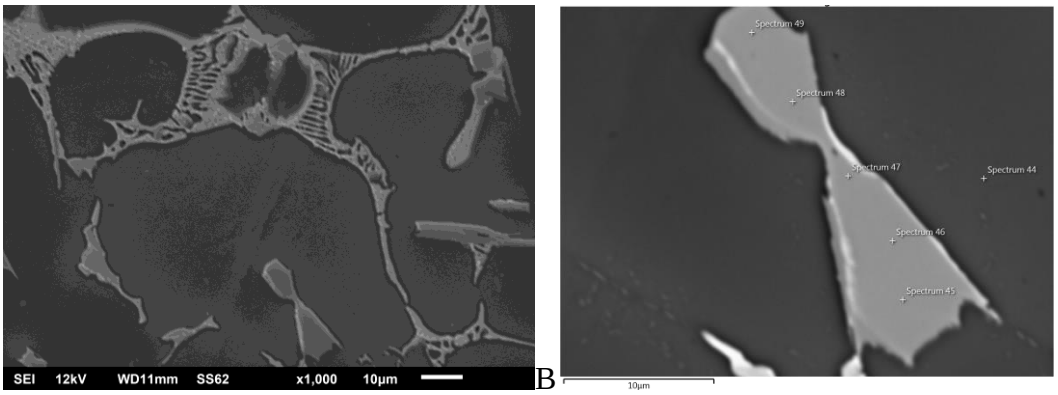

A B

Figure 6.110 (A) SEM images of TC8 of Alloy 7 (B) Magnified EDS image used for Elemental analysis

Table 6.48 Elemental composition of intermetallics marked on Figure 6.110 B

Phase # as marked in the image	Al		Fe		
	wt%	at%	wt%	at%	phase
1	60	76	35	22	$FeAl_3$
2	61	77	36	22	$FeAl_3$
3	61	77	35	21	$FeAl_3$
4	60	76	36	22	$FeAl_3$
5	60	77	36	22	$FeAl_3$

Alloy 8

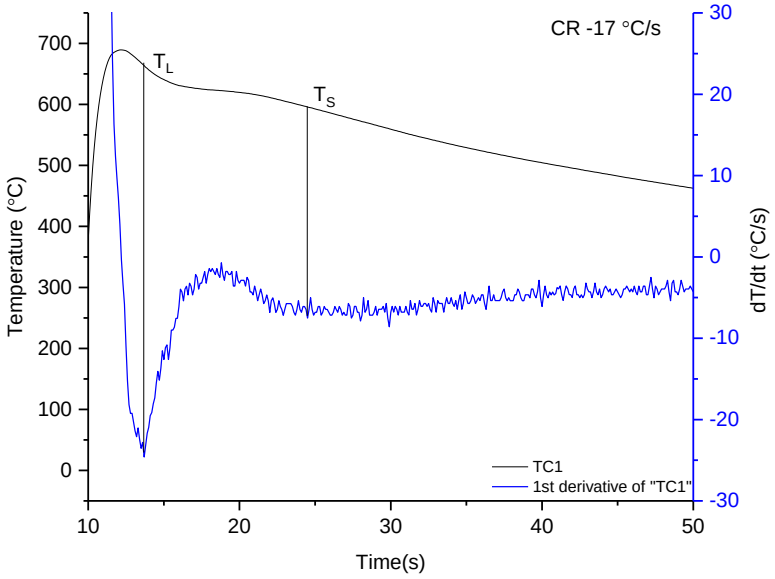

Figure 6.111 Cooling curve and the associated dT/dt curve for TC1 location

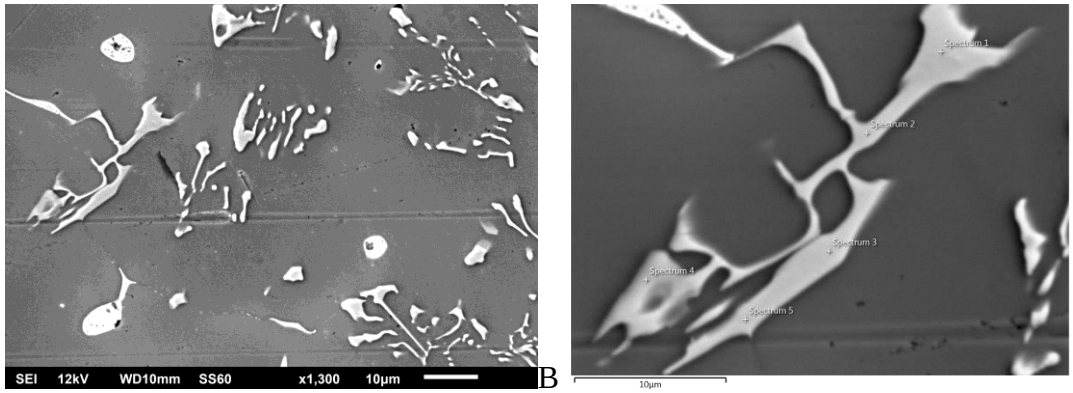

A B

Figure 6.112 (A) SEM images of TC1 of Alloy 8 (B) Magnified EDS image used for
Elemental analysis

Table 6.49 Elemental composition of intermetallics marked on Figure 6.112 B

Phase # as marked in the image	Al		Fe		
	wt%	at%	wt%	at%	phase
1	68	82	24	14	$FeAl_6$
2	70	83	22	13	$FeAl_6$
3	67	82	24	14	$FeAl_6$
4	75	86	17	10	$FeAl_6$
5	70	82	22	13	$FeAl_6$

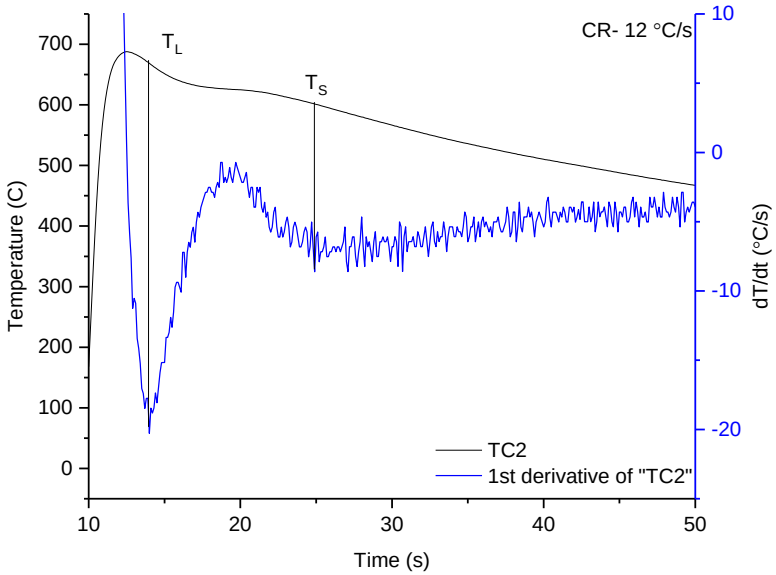

Figure 6.113 Cooling curve and the associated dT/dt curve for TC2 location

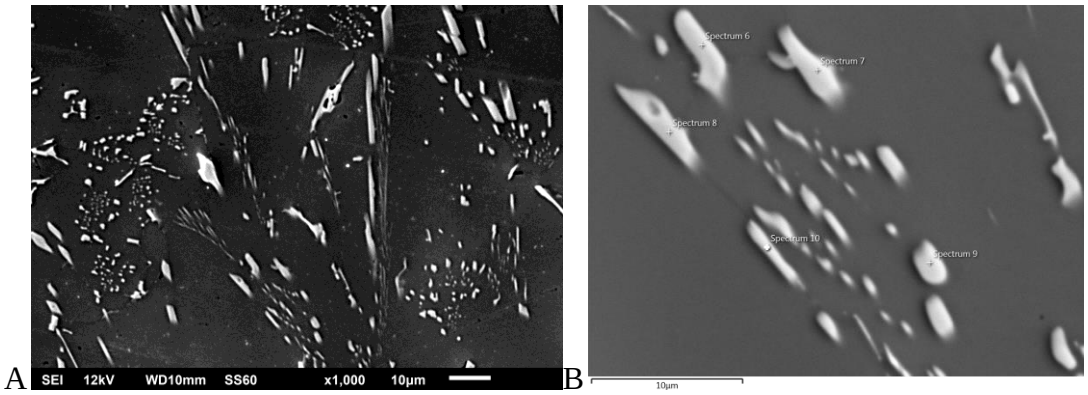

A B

Figure 6.114 (A) SEM images of TC2 of Alloy 8 (B) Magnified EDS image used for Elemental analysis

Table 6.50 Elemental composition of intermetallics marked on Figure 6.114 B

Phase # as marked in the image	Al		Fe		
	wt%	at%	wt%	at%	phase
1	67	82	24	14	$FeAl_6$
2	68	82	22	13	$FeAl_6$
3	71	83	21	12	$FeAl_6$
4	70	83	20	12	$FeAl_6$
5	68	82	23	13	$FeAl_6$

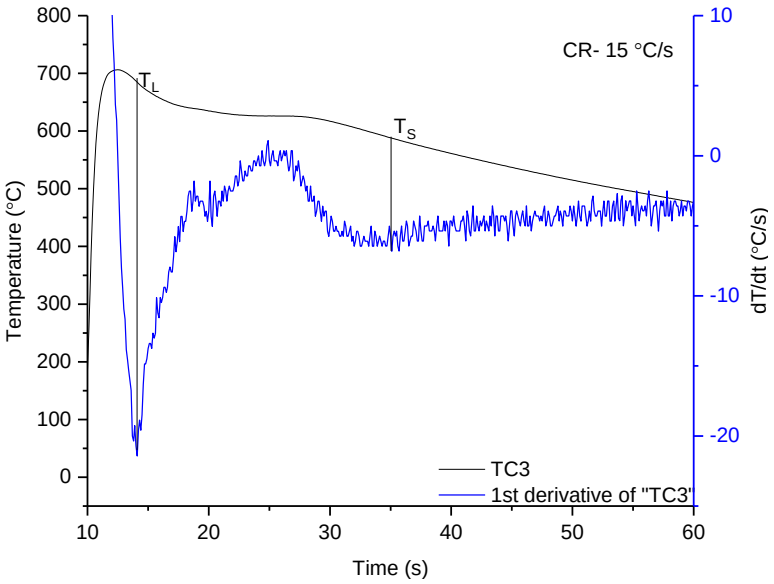

Figure 6.115 Cooling curve and the associated dT/dt curve for TC3 location

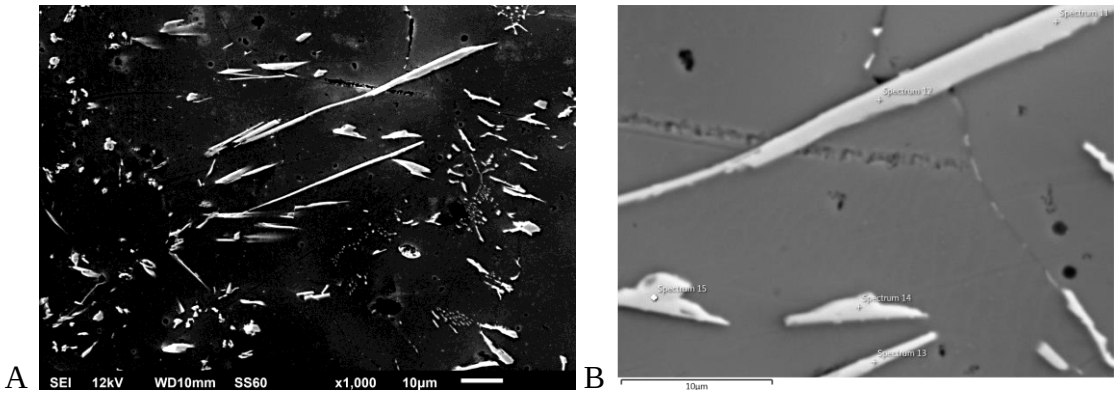

Figure 6.116 (A) SEM images of TC3 of Alloy 8 (B) Magnified EDS image used for Elemental analysis

Table 6.51 Elemental composition of intermetallics marked on Figure 6.116 B

Phase # as marked in the image	Al		Fe		
	wt%	at%	wt%	at%	phase
1	61	76	37	23	$FeAl_3$
2	61	76	37	22	$FeAl_3$
3	63	78	34	20	$FeAl_3$
4	62	77	36	22	$FeAl_3$
5	61	76	37	22	$FeAl_3$

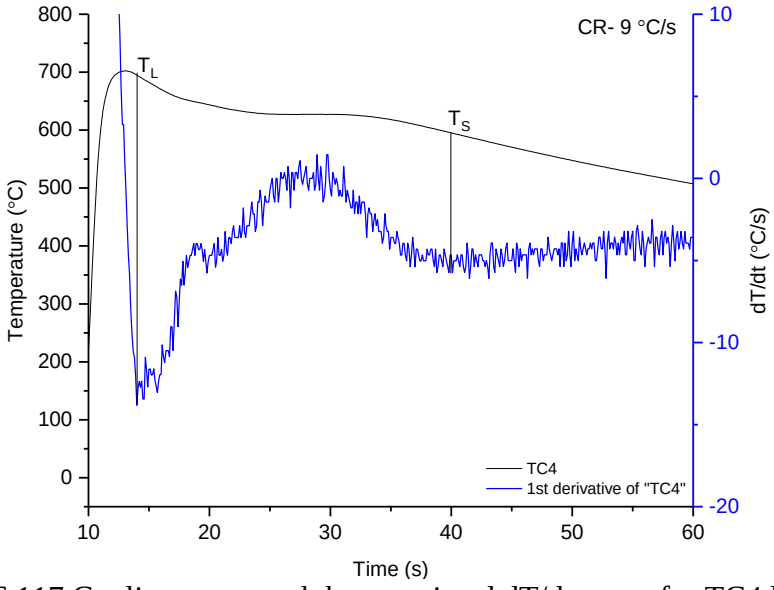

Figure 6.117 Cooling curve and the associated dT/dt curve for TC4 location

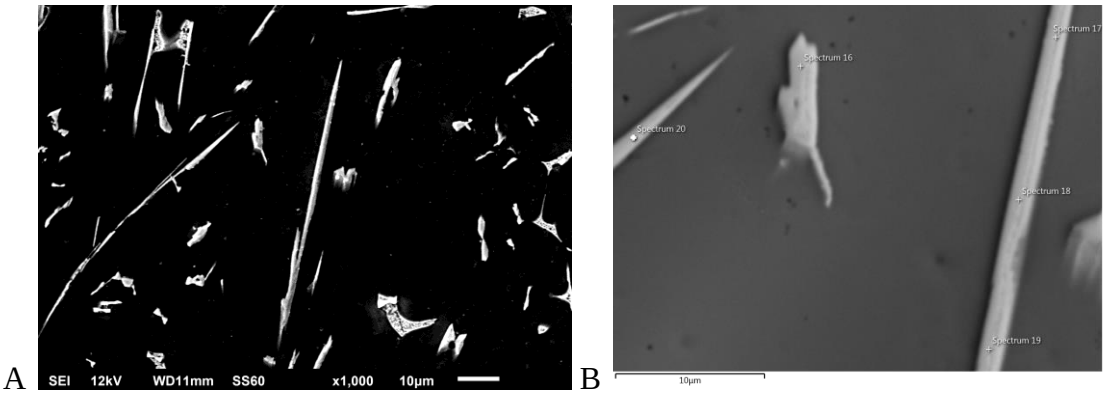

Figure 6.118 (A) SEM images of TC4 of Alloy 8 (B) Magnified EDS image used for Elemental analysis

Table 6.52 Elemental composition of intermetallics marked on Figure 6.118 B

Phase # as marked in the image	Al		Fe		
	wt%	at%	wt%	at%	phase
1	62	77	37	22	$FeAl_3$
2	62	77	35	21	$FeAl_3$
3	63	78	34	20	$FeAl_3$
4	64	79	33	20	$FeAl_3$
5	66	80	30	18	$FeAl_6$

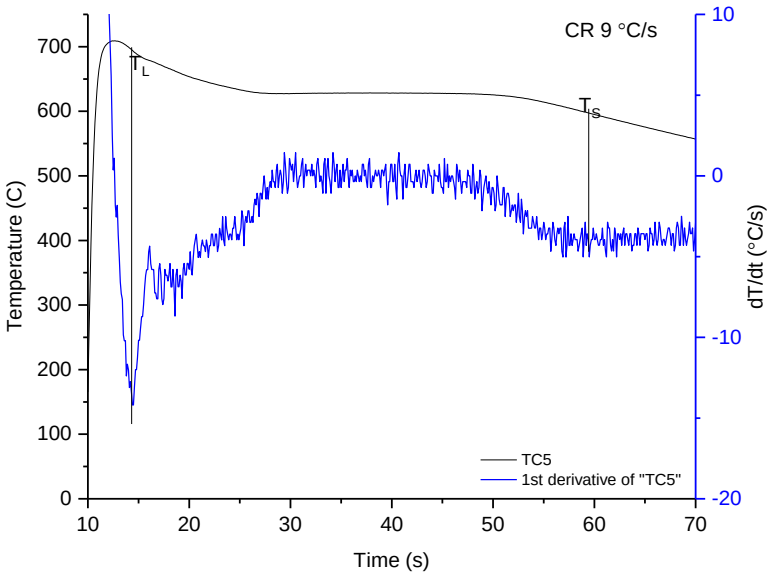

Figure 6.119 Cooling curve and the associated dT/dt curve for TC5 location

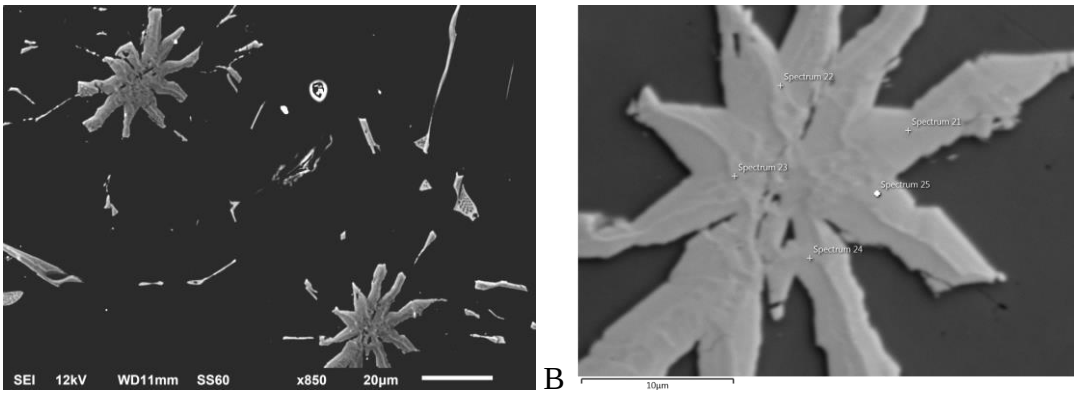

Figure 6.120 (A) SEM images of TC5 of Alloy 8 (B) Magnified EDS image used for Elemental analysis

Table 6.53 Elemental composition of intermetallics marked on Figure 6.120 B

Phase # as marked in the image	Al		Fe		
	wt%	at%	wt%	at%	phase
1	61	77	36	22	$FeAl_3$
2	61	76	37	23	$FeAl_3$
3	61	77	36	22	$FeAl_3$
4	62	77	37	22	$FeAl_3$
5	60	76	37	23	$FeAl_3$

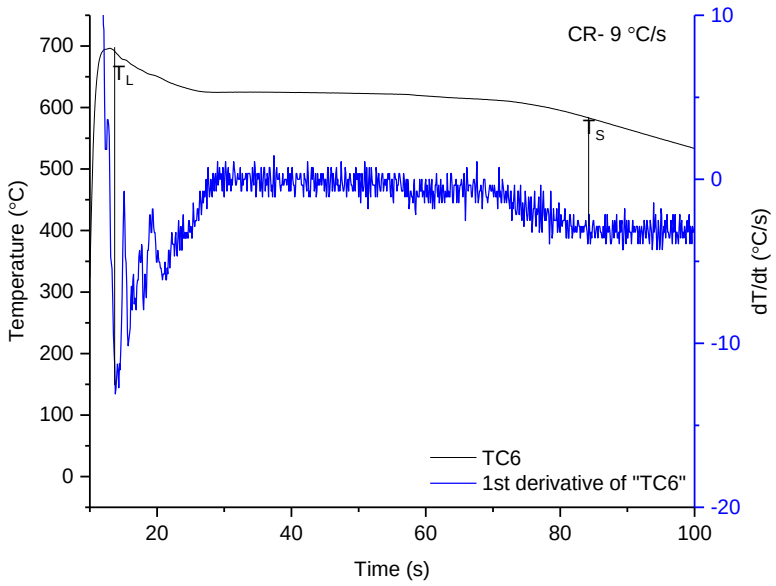

Figure 6.121 Cooling curve and the associated dT/dt curve for TC6 location

A 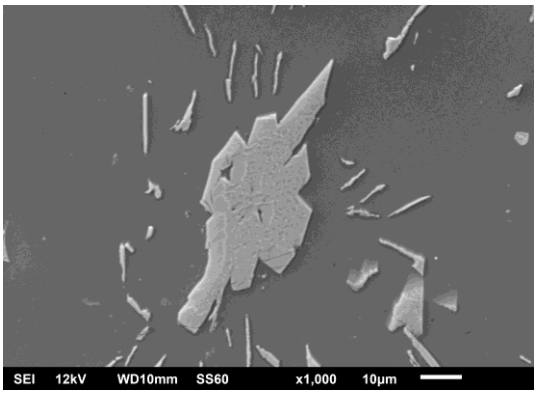

B 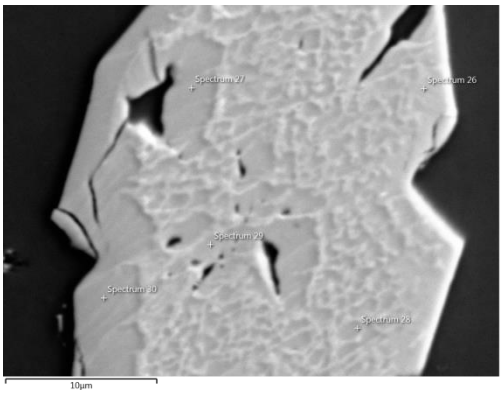

Figure 6.122 (A) SEM images of TC6 of Alloy 8 (B) Magnified EDS image used for Elemental analysis

Table 6.54 Elemental composition of intermetallics marked on Figure 6.122 B

Phase # as marked in the image	Al		Fe		
	wt%	at%	wt%	at%	phase
1	61	77	38	23	$FeAl_3$
2	62	77	37	22	$FeAl_3$
3	62	77	37	23	$FeAl_3$
4	61	77	38	23	$FeAl_3$
5	62	78	37	22	$FeAl_3$

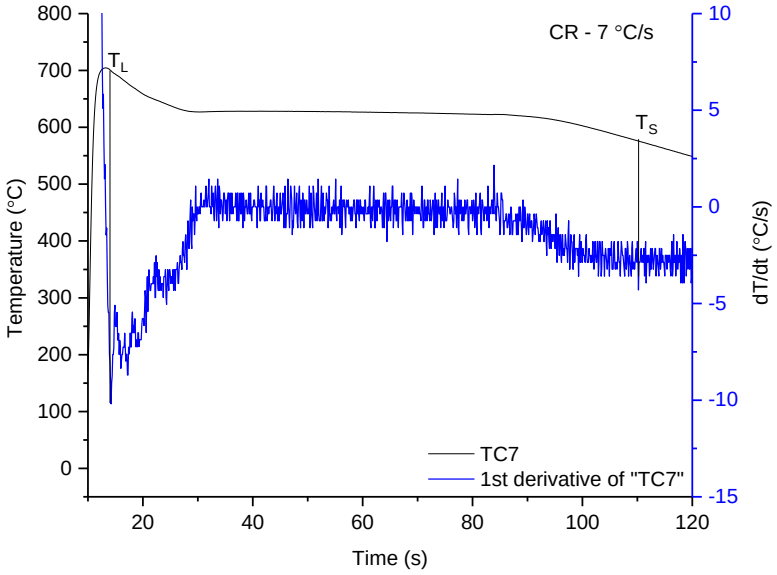

Figure 6.123 Cooling curve and the associated dT/dt curve for TC7 location

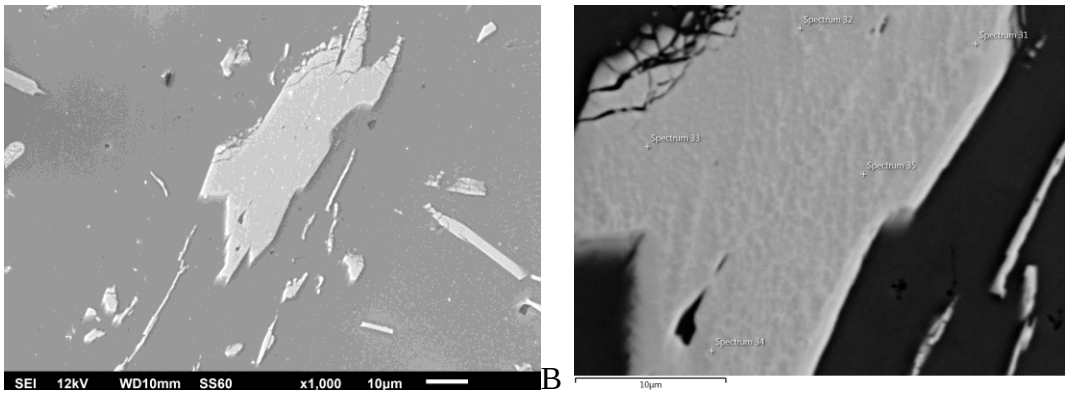

A B

Figure 6.124 (A) SEM images of TC7 of Alloy 8 (B) Magnified EDS image used for Elemental analysis

Table 6.55 Elemental composition of intermetallics marked on Figure 6.124 B

Phase # as marked in the image	Al		Fe		
	wt%	at%	wt%	at%	phase
1	61	77	38	23	$FeAl_3$
2	62	77	37	23	$FeAl_3$
3	62	77	38	23	$FeAl_3$
4	62	77	37	22	$FeAl_3$
5	61	76	38	23	$FeAl_3$

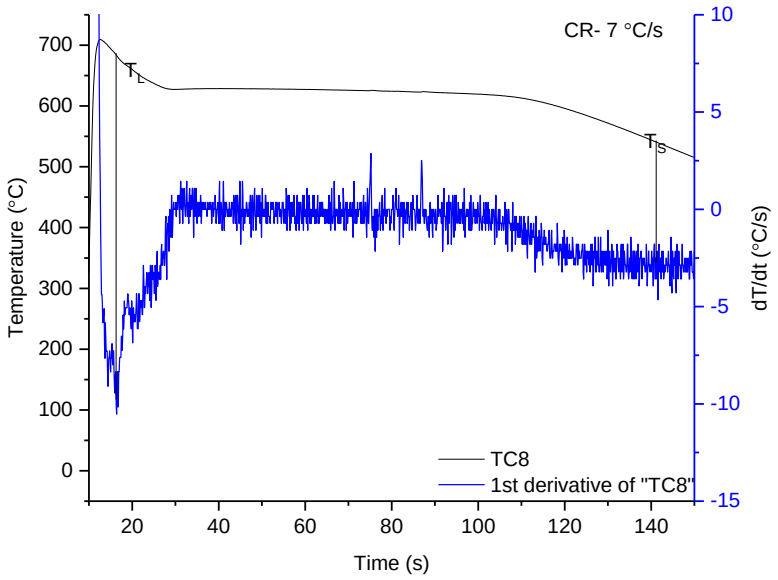

Figure 6.129 Cooling curve and the associated dT/dt curve for TC8 location

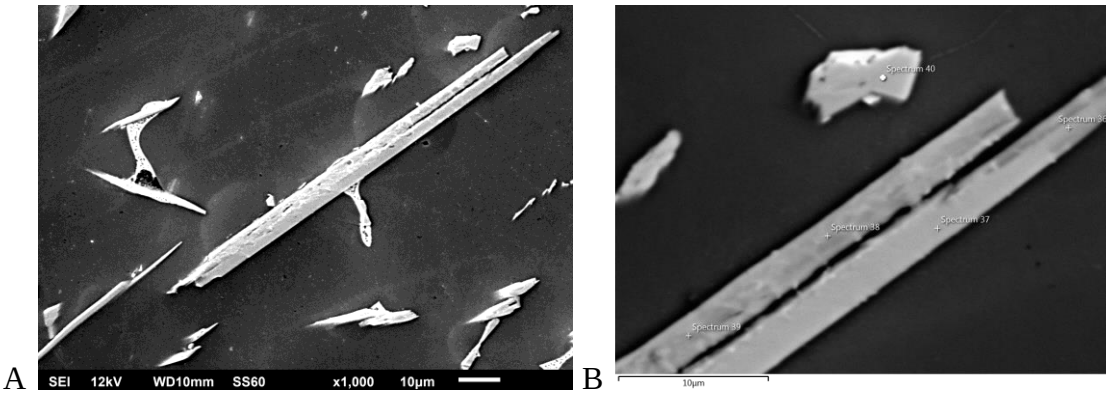

A B

Figure 6.130 (A) SEM images of TC8 of Alloy 8 (B) Magnified EDS image used forElemental analysis

Table 6.56 Elemental composition of intermetallics marked on Figure 6.130 B

Phase # as marked in the image	Al		Fe		
	wt%	at%	wt%	at%	phase
1	70	82	26	15	$FeAl_6$
2	65	79	33	20	$FeAl_3$
3	70	82	26	15	$FeAl_6$
4	68	81	27	16	$FeAl_6$
5	61	77	38	23	$FeAl_3$

Alloy 9

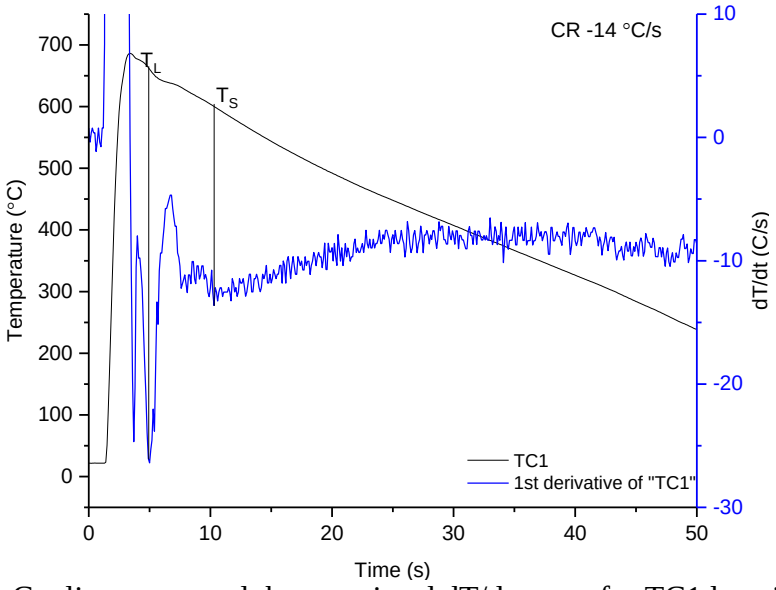

Figure 6.131 Cooling curve and the associated dT/dt curve for TC1 location

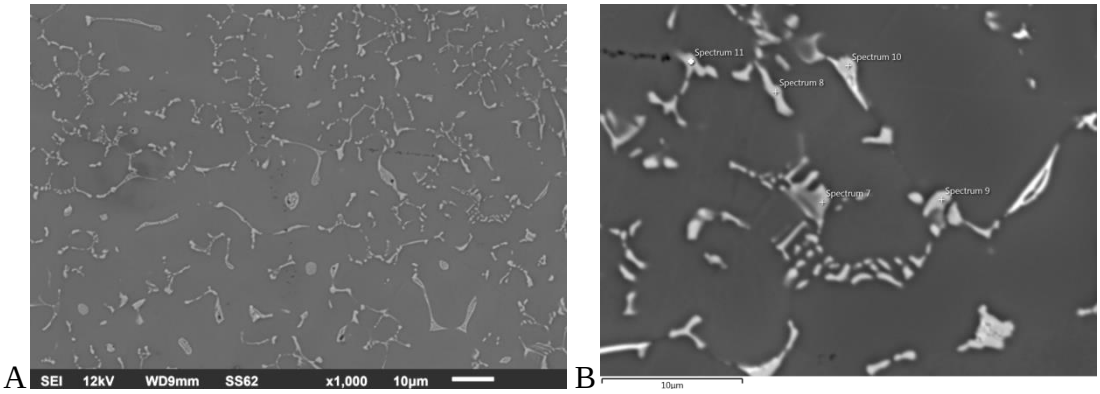

Figure 6.132 (A) SEM images of TC1 of Alloy 9 (B) Magnified EDS image used for Elemental analysis

Table 6.57 Elemental composition of intermetallics marked on Figure 6.132 B

Phase # as marked in the image	Al		Fe		
	wt%	at%	wt%	at%	phase
1	73	85	19	11	$FeAl_6$
2	67	81	24	14	$FeAl_6$
3	65	79	27	16	$FeAl_6$
4	61	77	28	17	$FeAl_6$
5	68	81	25	15	$FeAl_6$

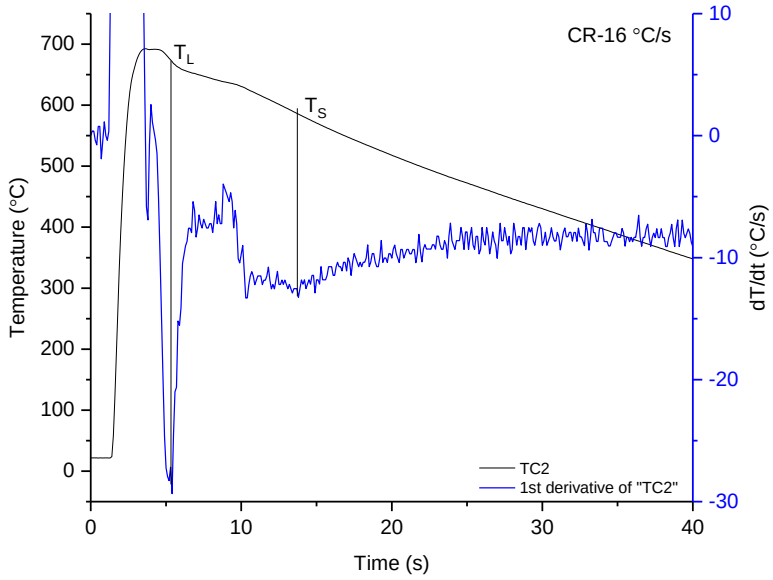

Figure 6.133 Cooling curve and the associated dT/dt curve for TC2 location

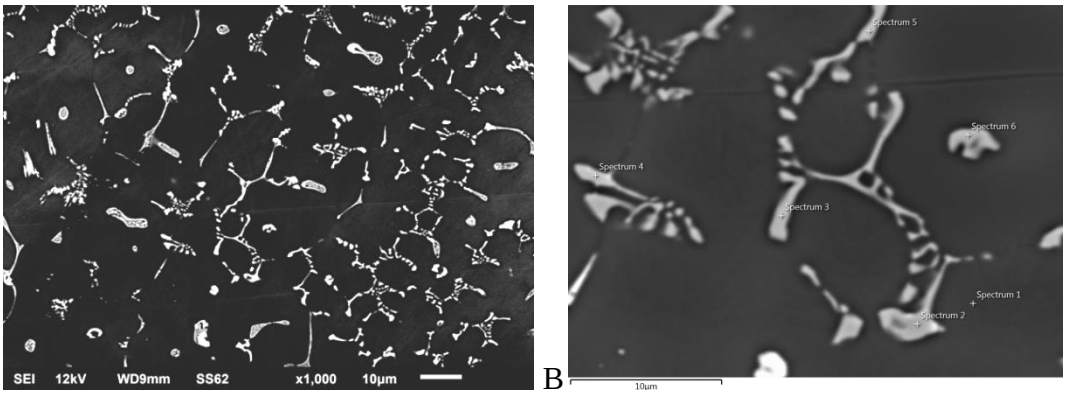

A B

Figure 6.134 (A) SEM images of TC2 of Alloy 9 (B) Magnified EDS image used for
Elemental analysis

Table 6.58 Elemental composition of intermetallics marked on Figure 6.134 B

Phase # as marked in the image	Al		Fe		
	wt%	at%	wt%	at%	phase
1	61	76	29	18	$FeAl_6$
2	65	79	27	16	$FeAl_6$
3	59	74	22	13	$FeAl_6$
4	67	81	25	14	$FeAl_6$
5	65	80	27	16	$FeAl_6$

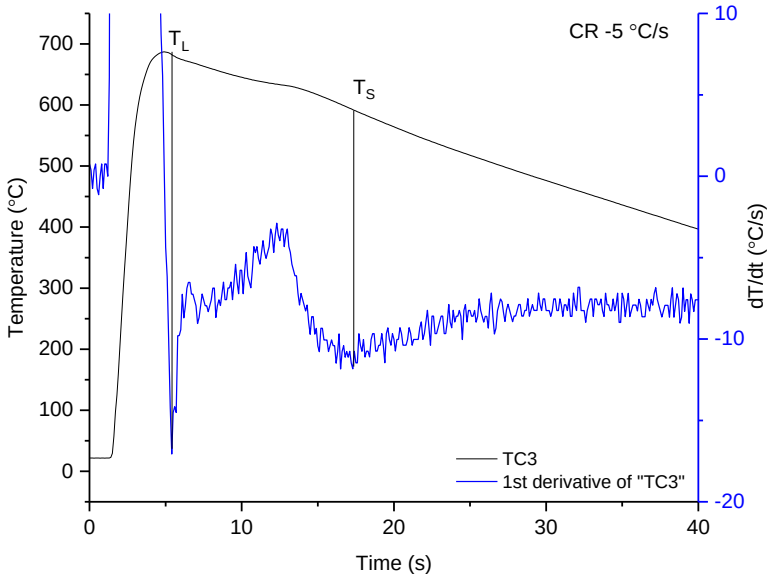

Figure 6.135 Cooling curve and the associated dT/dt curve for TC3 location

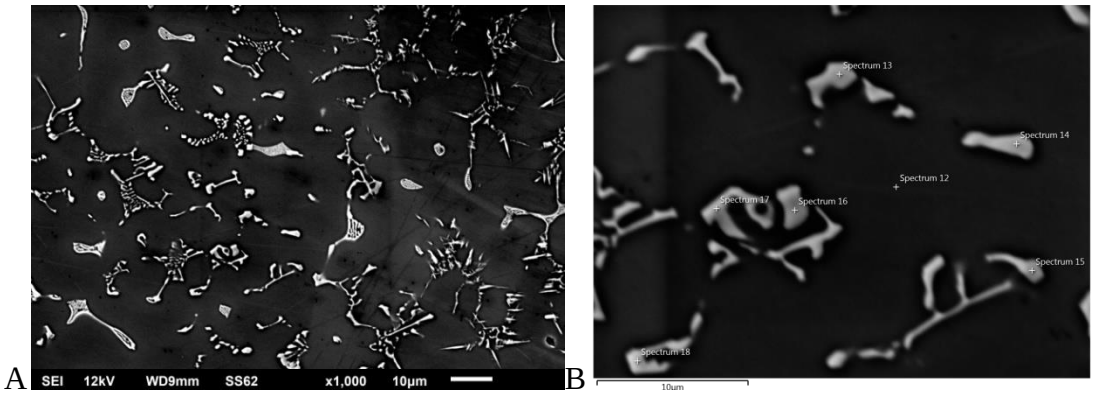

A B

Figure 6.136 (A) SEM images of TC3 of Alloy 9 (B) Magnified EDS image used for
Elemental analysis

Table 6.59 Elemental composition of intermetallics marked on Figure 6.136 B

Phase # as marked in the image	Al		Fe		
	wt%	at%	wt%	at%	phase
1	66	80	27	16	$FeAl_6$
2	62	78	31	19	$FeAl_3$
3	76	86	17	9	$FeAl_6$
4	73	85	19	11	$FeAl_6$
5	73	85	19	11	$FeAl_6$

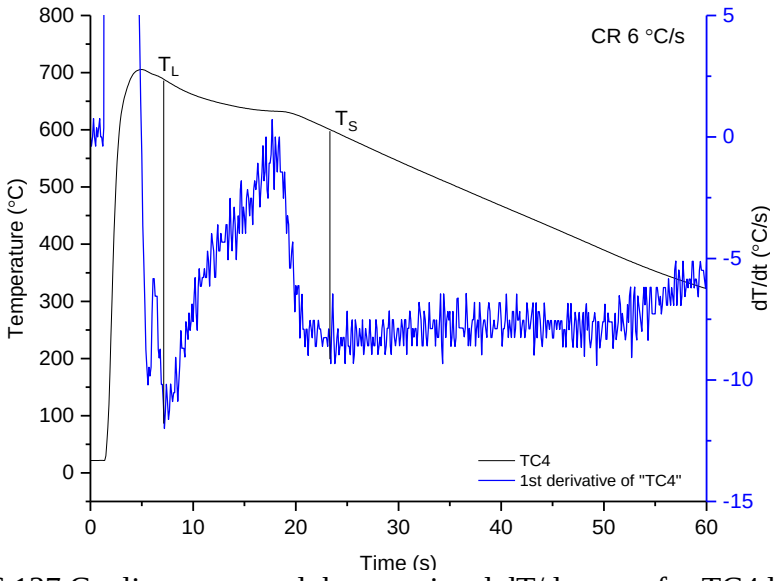

Figure 6.137 Cooling curve and the associated dT/dt curve for TC4 location

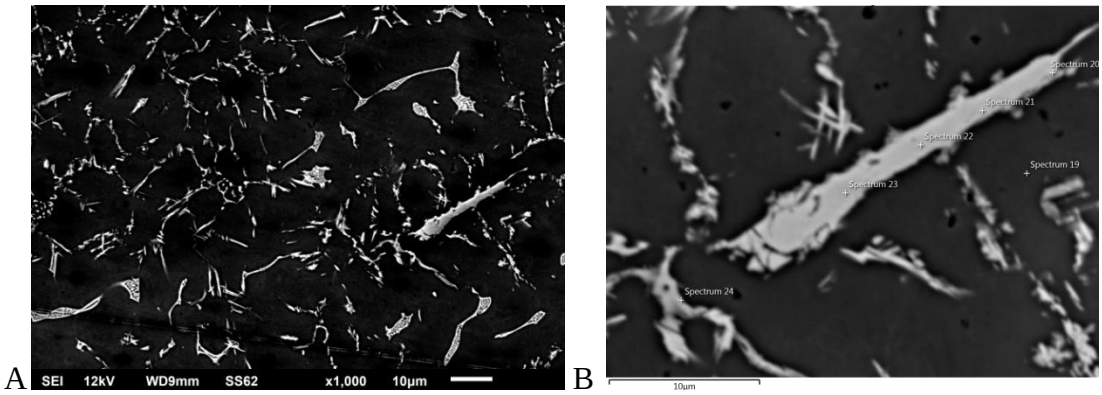

A B

Figure 6.138 (A) SEM images of TC4 of Alloy 9 (B) Magnified EDS image used for
Elemental analysis

Table 6.60 Elemental composition of intermetallics marked on Figure 6.138 B

Phase # as marked in the image	Al		Fe		
	wt%	at%	wt%	at%	phase
1	61	77	37	22	$FeAl_3$
2	61	77	37	23	$FeAl_3$
3	61	77	37	23	$FeAl_3$
4	61	76	37	23	$FeAl_3$
5	69	82	25	14	$FeAl_6$

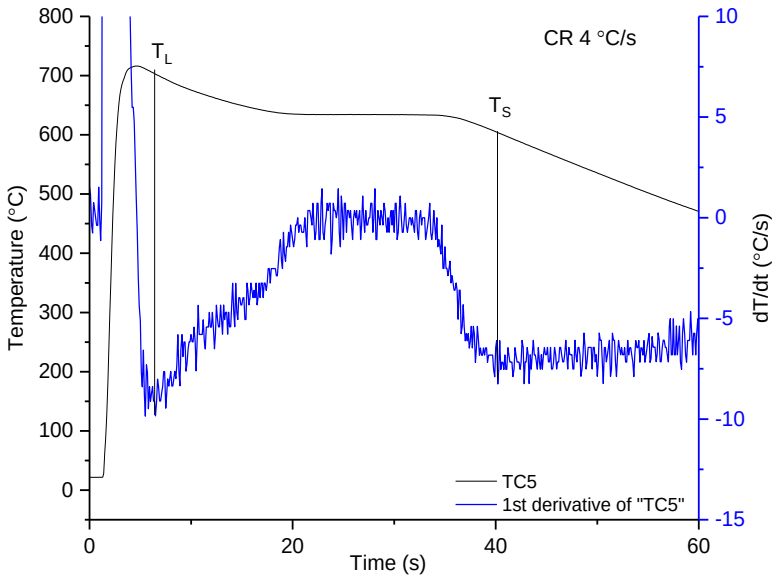

Figure 6.139 Cooling curve and the associated dT/dt curve for TC5 location

A 

B 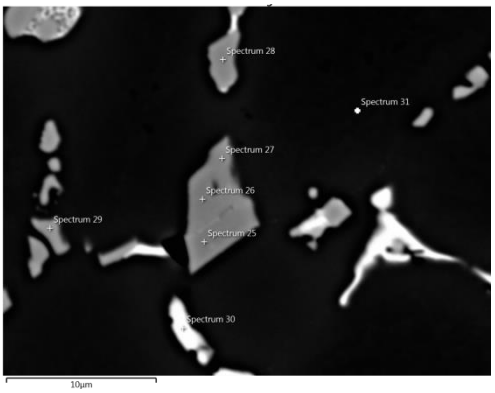

Figure 6.140 (A) SEM images of TC5 of Alloy 9 (B) Magnified EDS image used for
Elemental analysis

Table 6.61 Elemental composition of intermetallics marked on Figure 6.140 B

Phase # as marked in the image	Al		Fe		
	wt%	at%	wt%	at%	phase
1	66	81	23	14	$FeAl_6$
2	66	82	22	13	$FeAl_6$
3	67	82	22	13	$FeAl_6$
4	66	81	23	14	$FeAl_6$
5	67	81	22	13	$FeAl_6$

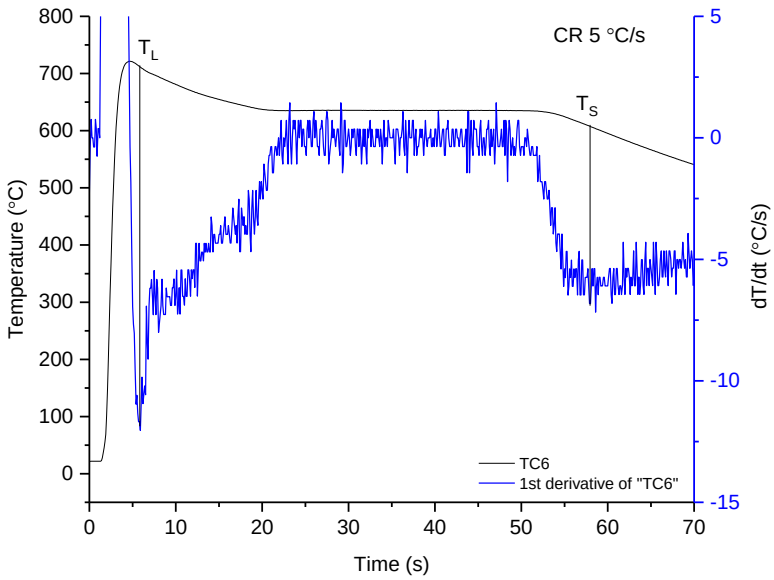

Figure 6.141 Cooling curve and the associated dT/dt curve for TC6 location

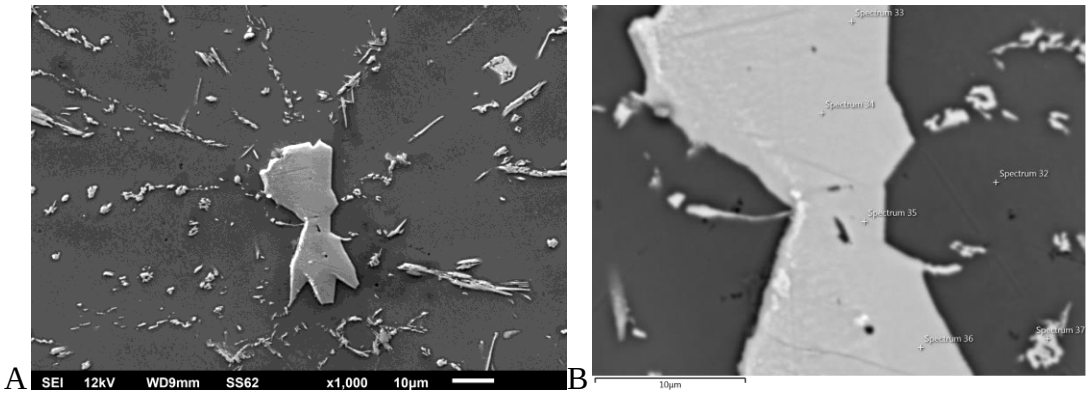

A B

Figure 6.142 (A) SEM images of TC6 of Alloy 9 (B) Magnified EDS image used for Elemental analysis

Table 6.62 Elemental composition of intermetallics marked on Figure 6.142 B

Phase # as marked in the image	Al		Fe		
	wt%	at%	wt%	at%	phase
1	61	76	37	23	$FeAl_3$
2	61	76	36	22	$FeAl_3$
3	61	77	39	23	$FeAl_3$
4	62	77	38	23	$FeAl_3$
5	65	80	33	20	$FeAl_3$

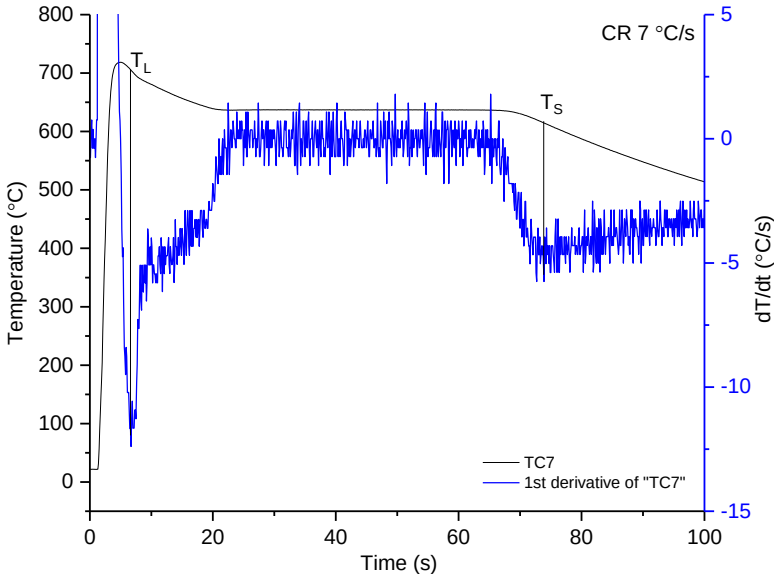

Figure 6.143 Cooling curve and the associated dT/dt curve for TC7 location

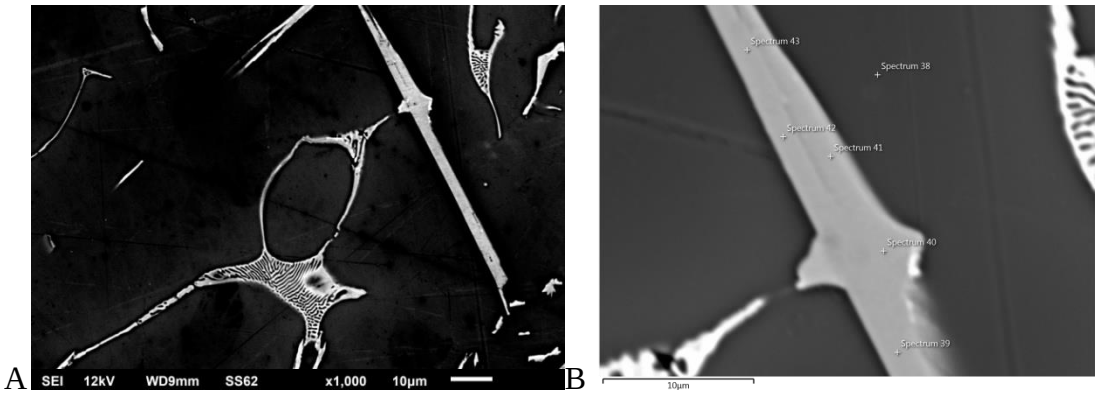

Figure 6.148 (A) SEM images of TC7 of Alloy 9 (B) Magnified EDS image used for
Elemental analysis

Table 6.63 Elemental composition of intermetallics marked on Figure 6.148 B

Phase # as marked in the image	Al		Fe		
	wt%	at%	wt%	at%	phase
1	62	77	36	22	$FeAl_3$
2	60	76	36	22	$FeAl_3$
3	61	76	36	22	$FeAl_3$
4	62	78	36	22	$FeAl_3$
5	61	72	37	22	$FeAl_3$

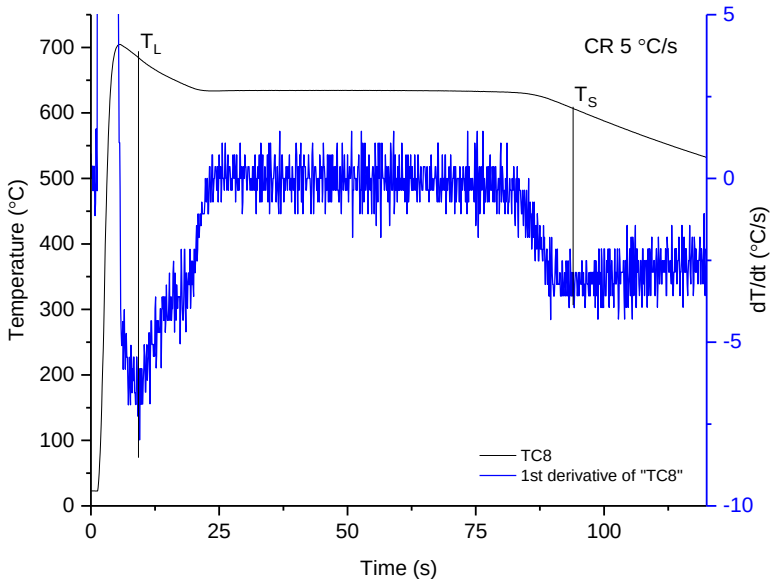

Figure 6.149 Cooling curve and the associated dT/dt curve for TC8 location

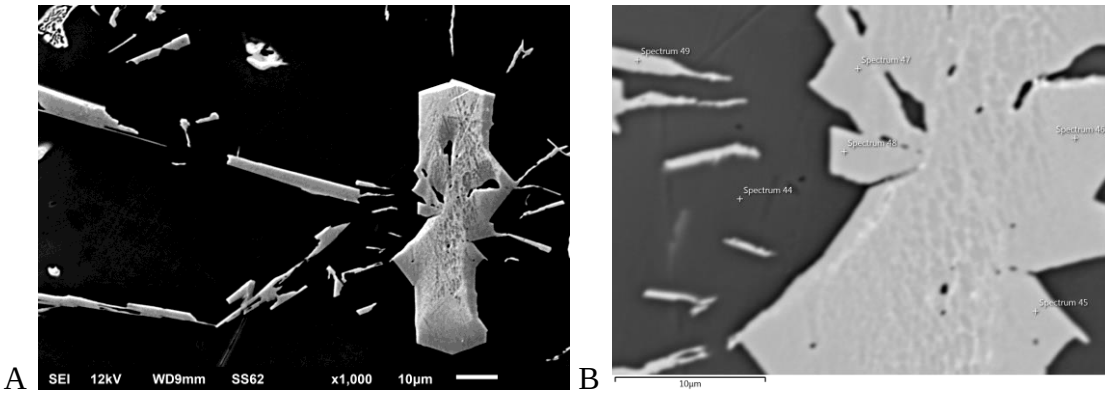

A B

Figure 6.150 (A) SEM images of TC8 of Alloy 9 (B) Magnified EDS image used for
Elemental analysis

Table 6.64 Elemental composition of intermetallics marked on Figure 6.150 B

Phase # as marked in the image	Al		Fe		
	wt%	at%	wt%	at%	phase
1	60	76	39	24	$FeAl_3$
2	60	76	38	23	$FeAl_3$
3	62	77	38	23	$FeAl_3$
4	61	77	37	22	$FeAl_3$
5	61	77	37	22	$FeAl_3$

References

[1] L. Cheah et al, "Factor of Two: Having the Fuel Consumption of New U.S Automobiles by 2035", Report by Laboratory of Energy and Environment, Massachusetts Institute of Technology, Cambridge, USA, Publication No. LFEE 2007-04 RP, Oct. (2007) 49-70

[2] S. Chayong, H.V. Atkinson and P. Kapranos, Materials Science and Engineering A 390 (2005) 3–12

[3] S. Shankar and D. Apelian, Metallurgical and Materials Transactions, 33B (2002) 465-476

[4] N.A. Belov, A.A. Aksenov, Dmitry G. Eskin "Iron in Aluminium Alloys: Impurity and Alloying Element". Taylor & Francis Inc, New York, (2002)

[5] J. A. Taylor, Procedia Materials Science 01 (2012) 19-33

[6] L. Wang, M. Makhlouf and D. Apelian, International Materials Reviews, 40:6 (2013) 221-238

[7] T. Akopyan and N.A.Belov, Non-Ferrous Metals. 01 (2016) 20-27

[8] M. Makhlouf and D. Apelian, "Casting Characteristics of Aluminum Alloys", Report by Advanced Casting Research Center, Worcester Polytechnic Institute-USA, Publication No. DOE/ID—13716, Feb. (2002)1-44

[9] Q. Han and S. Viswanathan, Metallurgical and Materials Transactions, 34A (2003) 139-146

[10] S. Shankar and D. Apelian, Journal of the Minerals, Metals & Materials Society 54:8 (2002) 47-54

[11] S. Shankar and D. Apelian, International Journal of Cast Metals Research, 15 (2002) 103-116

[12] H. W. L. Phillips, Annotated equilibrium diagrams of some aluminum alloy systems. London, Institute of Metals (1959)

[13] X. Li, A. Scherf, M. Heilmaier, and F. Stein, Journal of Phase Equilibria and Diffusion 37 (2016) 162-173

[14] C.M. Allen, K.A.Q. O'Reilly, B. Cantor, and P.V. Evans, Progress in Materials Science 43 (1998) 89-170

[15] D. Liang and H. Jones, Scripta Materialia, 55 (1991) 25-28

[16] E. H. Hollingsworth, G. R. Frank, Jr., and R. E. Willett, Transactions, TMS-AIME, 224 (1962) 188

[17] H. Kosuge and Keikinzoku 34 (1984) 4

[18] L. BaÈckerud, Jernkont, 152 (1968) 109

[19] C.McL. Adam and L.M.Hogan, Acta Materialia, 23 (1975) 345

[20] I. Hughes and H. J Jones, Journal of Material Science, 11 (1976) 1781-96

[21] R.M.K. Young and T.W. Clyne, Scripta Materialia, 15 (1981) 1211
.
[22] T. O. Mbuya, B. O. Odera and S. P. Ng'ang'a, International Journal of Cast Metals Research- 16:5 (2016) 451-465

[23] S. G. Shabestari, and J. E. Gruzleski, Cast Metals, 6:4 (1994) 217-224

[24] S. Li, Hot tearing in cast aluminum alloys, PhD dissertation, (2010), Worcester polytechnic institute.

[25] L. F. Mondolfo, "Aluminum alloys: structure and properties", London, Butterworths , (1976)

[26] S. Murali, K. S. Raman, and K.S.S. Murthy: Materials. Science and Engineering, A151 (1992)1-10

[27] S. Ji, W. Yang, F. Gao, D. Watson, Z. Fan, Materials Science and Engineering, 564A (2013) 130-139

[28] S .Gowri and F.H.Samuel, Metallurgical and Materials Transactions, 25A (1994) 437-448

[29] L. Sweet, M. A. Easton, J. A. Taylor, J. F. Grandfield, C. J. Davidson , Liming Lu, M. J. Couper, D. H. St John, Metallurgical and Materials Transactions A,44:12 (2013) 5396-5407

[30] S. Shankar and D. Apelian, Transactions of the North American Die Casting Association (NADCA), Nov. (1997) 245-281

[31] J. Lee and K. Subramanian, Journal of Materials Science 27 (1992) 5453.